Contribution to the study of directive or wide-band miniature antennas with non-Foster circuits

Abdullah Haskou

ANNÉE 2016

UNIVERSITÉ DE RENNES 1

UNIVERSITE BRETAGNE LOIRE

THÈSE / UNIVERSITÉ DE RENNES 1

sous le sceau de l'Université Bretagne Loire

pour le grade de

DOCTEUR DE L'UNIVERSITÉ DE RENNES 1

Mention : Traitement de Signal et Télécommunications

Ecole doctorale MATISSE

présentée par

Abdullah Haskou

préparée à l'unité de recherche IETR (UMR 6164)

Institut d'Electronique et de Télécommunications de Rennes

UFR Informatique et Electronique

Contribution à l'Etude des Antennes Miniatures Directives ou Large-Bande avec des Circuits Non-Foster

Thèse soutenue à Rennes le 7 Septembre 2016

devant le jury composé de :

Robert STARAJ

Professeur à Polytech'Nice Sophia / examinateur et président

Anja SKRIVERVIK

Professeur à l'Ecole Polytechnique Fédérale de Lausanne / rapporteur

Eric RIUS

Professeur à l'Université de Bretagne Occidentale / rapporteur

Christophe DELAVEAUD

Docteur (HDR) au CEA-LETI Grenoble / examinateur

Sylvain COLLARDEY

Maitre de conférences à l'Université de Rennes 1 / examinateur

Ala SHARAIHA

Professeur à l'Université de Rennes 1 / directeur de thèse

To my parents

Ji bo dê û bavê min

Acknowledgments

This thesis started October 1, 2013 and finished September 7, 2016 after three years of hard work, patience, anxiety, and sometimes despair. During these years I had the chance to meet and work with some wonderful people to whom I shall be forever indebted.

First of all I am profoundly grateful for my PhD. advisers Prof. Ala Sharaiha, Dr. Sylvain Collardey and Dr. Dominique Lemur for giving me the opportunity to do this PhD. I am particularly thankful for their guidance, supervision, valuable advise and constant encouragement that helped achieving this work. I am also thankful for our discussions that improved my knowledge.

I would like to thank all the technical staff in Institut d'Electronique et de Télécommunications de Rennes (IETR) for all the prototypes they realized and the measurements they helped me perform.

I am also thankful for all the administrative team in IETR for facilitating my administrative procedures and my professional traveling.

I would also like to give a special thank to all my colleagues for all the interesting time we spent together and the discussions we had.

I would like to express my gratitude to the jury members for the time they devoted for reading this thesis and their valuable comments and questions that helped enhancing the quality and readability of this manuscript.

Finally, I would like to thank my family for their constant encouragement, support and belief in me. Their presence on my side means the world to me and I shall be forever grateful.

List of Abbreviations

ESA . . . . . Electrically Small Antenna
Q . . . . . Quality Factor
PCB . . . . . Printed Circuit Board
HPBW . . . . . Half-Power Beamwidth
FBR . . . . . Front to Back Ratio
CP . . . . . Circularly-Polarized
LHCP . . . . . Left-Hand Circular Polarization
RHCP . . . . . Right-Hand Circular Polarization
NIC . . . . . Negative Impedance Converter
OIP . . . . . Output Intercept Point
AMC . . . . . Artificial Magnetic Conductor
NF . . . . . Noise Figure
SNR . . . . . Signal to Noise Ratio
TCM . . . . . Theory of Characteristic Modes
HIS . . . . . High Impedance Surface
NII . . . . . Negative Impedance Inverter
OpAmp. . . . . Operational Amplifier
BJT . . . . . Bipolar Junction Transistor
FET . . . . . Field Effect Transistor
ILA . . . . . Inverted-L Antenna
IIP . . . . . Input Intercept Point
VNA . . . . . Vector Network Analyzer
PSD . . . . . Power Spectral Density
UWB . . . . . Ultra Wide-Band
PCB . . . . . Printed Circuit Board
AUT . . . . . Antenna Under-Test
SLL . . . . . Side Lobe Level
AR . . . . . Axial Ratio

Contents

List of Figures

List of Tables

Résumé des Travaux

Contexte de L'Etude

Avec l'évolution des technologies sans fil, un smartphone doit supporter de plus en plus de standards de communication (GSM, UMTS, LTE, Bluetooth, WiFi, GPS, ...) afin d'offrir aux usagers les meilleures performances possibles. De plus, de nouvelles applications comme les systèmes de pointage (télécommande radio) peuvent nécessiter l'intégration de systèmes compacts à rayonnement directifs nécessaires pour contrôler séparément plusieurs périphériques en fonction de l'orientation de la télécommande. Ces besoins nécessitent un effort de plus en plus important d'intégration des systèmes et donc des antennes dont la miniaturisation doit permettre conserver des performances acceptables en termes de bande passante, de directivité et d'efficacité. Cependant, les performances des antennes ont des limites fondamentales liées à leurs dimensions physiques. Plusieurs études ont précisé les limites fondamentales pour des Antennes Électriquement Petites (AEP). En 1947, A.H. Wheeler a été le premier à étudier ces limites. Il a défini une AEP comme une antenne avec $ka < 1$, où $k = \frac{2\pi}{\lambda}$ est le nombre d'onde, λ est la longueur d'onde en espace libre et a est le rayon de la plus petite sphère entourant l'antenne. Chu a montré que le facteur de qualité (Q) d'une antenne est inversement proportionnel à $(ka)^3$ ce qui signifie que la miniaturisation augmente de manière significative le facteur Q. De plus, Bode-Fano et Yaghjian-Best ont montré que la bande passante d'une antenne est inversement proportionnelle à son facteur de qualité. Par conséquent, il est difficile de concevoir des AEP à large bande de fréquence. Harrington a démontré que la directivité d'une antenne est aussi directement reliée à ses dimensions et qu'en raison de cette contrainte, il est difficile de concevoir des AEP directives.

Les Contributions de la Thèse

Bien que les limites définies par Bode-Fano et Yaghjian-Best, concernant la bande passante des antennes, ne sont applicables qu'aux antennes adaptées par des circuits de type Foster, des circuits dits non-Foster semblent en mesure de surpasser ces limites. De plus, la théorie sur les réseaux superdirectifs montre que la limite de Harrington sur la directivité des antennes peut être dépassée dans certaines conditions. Par conséquent, ce travail se concentre sur l'étude et la conception d'antennes adaptées par des circuits à comportement non-Foster et de réseaux d'antennes superdirectifs comme solutions possibles pour l'amélioration des performances des AEP.

Les Antennes Adaptées par des Circuits Non-Foster

La première partie de cette thèse a été menée dans le cadre du projet ANR "Systèmes d'antenne capteur miniature (SENSAS)". Ce projet a pour but d'étudier, de réaliser et de caractériser de nouvelles antennes ultra-miniatures et intelligentes, capables de s'adapter à leur environnement et, pour certaines d'entre elles, intégrant des capteurs de température ou de pression. Le projet associe les compétences de trois laboratoires de recherche CEA-Leti, l'IETR et LEAT, et de deux entreprises, Technicolor et SENSeOR [1]. Dans ce cadre, un convertisseur d'impédance négative (NIC) de type Linvill flottant à comportement non-Foster a été réalisé pour obtenir un condensateur de faible valeur (quelques pF) mais négative, donc de valeur de réactance très élevée. Dans la bande UHF, les capacités parasites des transistors sont exploitées afin d'atteindre ces faibles valeurs de capacité. Un prototype du circuit à deux ports est réalisé pour étudier les pertes du circuit ainsi que sa stabilité. Les résultats obtenus montrent que le circuit présente un gain satisfaisant en basse fréquence ($7dB$ autour de $250MHz$). Avec la fréquence, le gain du circuit diminue dans la bande utile (autour de $910MHz$) pour atteindre $1dB$. A partir de $1.3GHz$, le circuit commence à générer des pertes qui augmentent alors avec la fréquence ($8dB$ à $3GHz$). Ce prototype est aussi utilisé pour analyser la stabilité du circuit selon différents critères. Les résultats obtenus montrent que le circuit est inconditionnellement stable à partir de $1.61GHz$. Les cercles de stabilité du circuit sont tracées dans la bande d'instabilité et montrent qu'une charge capacitive (ce qui est le cas avec une antenne de type dipôle) stabilisera le circuit. Les produits d'intermodulation du circuit sont également mesurés et mettent en évidence des points d'interceptions en sortie (OIP) du deuxième et troisième ordre assez élevés. Le point de compression du gain du circuit est aussi étudié et montre que le circuit présentent des points de compression et de saturation très élevés ($12.5dBm$ et $27.5dBm$ respectivement). Une fois le circuit caractérisé, celui-ci est utilisé pour adapter une antenne miniature de type ILA (Inverted L-Antenna) dans la bande de fréquence ($0.76-2.17GHz$). La stabilité de l'antenne associée au circuit est mise en évidence à l'aide d'un analyseur de spectre. De plus, une comparaison entre le niveau de bruit de l'analyseur de spectre, connecté à l'antenne ou à une charge adaptée (50Ω), montre que le circuit n'ajoute pratiquement aucun bruit. Les résultats de mesures montrent aussi que l'antenne présente une bonne linéarité avec un rendement total acceptable (environ 20%). Les caractéristiques de rayonnement sont mesurées suivant deux modes de fonctionnement, en émission et en réception, montrant ainsi que l'antenne fonctionne de façon réciproque. Le rendement est semblable dans les deux modes. En prolongement de ces travaux, le circuit NIC est également utilisé pour adapter une antenne ILA de mêmes dimensions que la précédente mais intégrée sur un PCB plus petit (équivalent à une clef USB). Cette antenne présente une oscillation en basse fréquence (autour de $100MHz$) mais aucune harmonique secondaire n'est mise en évidence en haute fréquence. En termes de bande-passante et rayonnement, cette antenne est aussi performante que la première sur le plus grand PCB.

Réseaux d'Antennes Superdirectifs

La deuxième partie de cette thèse s'inscrit dans le cadre du projet "Super-directivité pour le contrôle du rayonnement des objets communicants (SOCRATE)" financé

également par l'Agence Nationale de la Recherche (ANR). Ce projet regroupe des équipes de recherche du CEA-Leti et de l'IETR, ainsi que deux partenaires industriels (Movea et Tagsys) portant des applications demandeuses en antennes compactes et directives. Le but du projet et d'améliorer la directivité des antennes électriquement petites [2]. Dans ce contexte, les limites théoriques des réseaux d'antennes superdirectifs ont tout d'abord été mises en évidence à partir d'un état de l'art exhaustif. Suite à cette première phase, une approche simple et pratique a été développée afin de faciliter la conception des réseaux d'antennes superdirectifs à base d'éléments parasites (ou chargées). La méthode consiste à intégrer les diagrammes de rayonnement des éléments du réseau dans les équations de Yaghjian pour calculer les pondérations en courant qui maximise la directivité du réseau dans la direction end-fire. Les pondérations obtenues et la matrice Z du réseau sont ensuite utilisées pour calculer les impédances actives de chaque élément. Finalement, un élément du réseau est choisi pour être alimenté tandis que les autres sont connectés à des charges équivalentes à leurs impédances actives. Les différentes étapes de la méthode sont décrites sur la Figure 1.

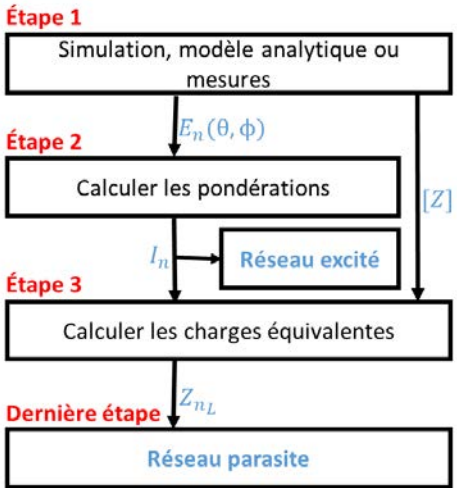

Figure 1: Un organigramme de la méthodologie de conception des réseaux superdirectifs à base d'éléments parasites.

Les limites pratiques de l'approche proposée sont démontrées par une étude paramétrique sur des réseaux à base de dipôles. Cette analyse montre que la méthode utilisant des charges n'est pas limitée par le nombre des éléments, ni par la distance inter-élément. Cette analyse montre également qu'en raison des limites et des difficultés pratiques, la conception de réseaux superdirectifs est effectuée suivant un compromis entre directivité, efficacité de rayonnement et dimension (nombre d'éléments et espacement inter-éléments). L'approche proposée est également utilisée pour la conception de réseaux superdirectifs à deux, trois et quatre éléments à base d'AEP. Dans tous les cas, la distribution des courants à la surface des antennes, notamment des éléments parasites, est très proche de celle du réseau qui aurait tous ses éléments alimentés. La même comparaison entre réseau alimenté et réseau parasite peut être faite concernant l'allure des diagrammes de rayonnement ainsi que de la valeur de directivité totale. En outre, la directivité end-fire du réseau parasite est maximale à la fréquence de conception pour laquelle les charges sont calculées.

Les résultats mesurés pour tous les prototypes fabriqués valident complètement les résultats de simulation. Ces travaux sur la superdirectivité d'antennes planaires ont aussi permis de répondre aux problématiques d'intégration sur PCB ainsi que de caractérisation expérimentale. Il a été montré que le phénomène de superdirectivité est très sensible à l'environnement. Cette problématique a nécessité de mener une étude afin d'optimiser l'intégration des antennes superdirectives sur des circuits imprimés (PCB) afin de conserver leurs directivités. Pour quelques exemples d'antennes, les résultats obtenus à partir de cette étude montrent que la configuration du PCB, cest-à-dire la position du réseau, a un impact significatif sur la directivité et l'efficacité de rayonnement. Ajouter une fente sur le PCB permet de contrôler la distribution du courant afin de maintenir une contribution constructive et ainsi de conserver, non seulement, la superdirectivité de l'antenne mais aussi d'accroître son efficacité. Confronté à des difficultés de mesure des AEP superdirectives intégrées sur PCB, différents scénarios pour connecter le système d'alimentation à l'antenne ont été évalués. Les résultats obtenus montrent qu'une connexion correcte du système d'excitation peut réduire ces effets négatifs, et par conséquent, permettre la caractérisation de l'antenne. La dernière partie de ces travaux a permis de développer une nouvelle stratégie pour concevoir des réseaux compacts utilisant des éléments superdirectifs dans la bande UHF RFID ($866MHz$). Un premier design de réseau 3D dont les dimensions totales sont de $20 \times 20 \times 7cm^3 (0.58\lambda \times 0.58\lambda \times 0.2\lambda)$ a permis d'atteindre une directivité totale de $11.4dBi$ avec une efficacité de rayonnement de 73%. Les ouvertures angulaires à mi-puissance (HPBW) dans les plans horizontal et vertical atteignent respectivement 56^o et 48^o pour un rapport avant-arrière (Front to Back Ratio, FBR) de $13.2dB$. Les résultats simulés et mesurés sont en très bon accord. À directivité égale, ce réseau est nettement plus compact que d'autres antennes plus classiques (Yagi par exemple). Ce travail basé sur un réseau à deux éléments peut être généralisé pour des réseaux à N-éléments superdirectifs tout en gardant à l'esprit les compromis à faire entre dimensions, directivité et efficacité de rayonnement du réseau. Un second réseau planaire a été développé à partir d'une antenne superdirective à deux éléments superposés. Cet élément superdirectif, de dimensions $8 \times 8 \times 2.5cm^3 (0.23\lambda \times 0.23\lambda \times 0.07\lambda)$ dans la bande UHF RFID, atteint une directivité totale de $7dBi$ et une efficacité de rayonnement de 43.4%. Ce élément compact et superdirectif est ensuite intégré dans le réseau planaire de 2×2. Pour une distance inter-élément de $26cm(0.75\lambda)$ et pour des dimensions totales de $34 \times 34 \times 2.5cm^3 (0.98\lambda \times 0.98\lambda \times 0.07\lambda)$, une directivité totale de $12.6dBi$ et une efficacité de rayonnement de 41% sont obtenues. Cette antenne est significativement plus petite que des réseaux classiques ayant la même directivité. Enfin, ce réseau planaire est aussi développé pour fonctionner en polarisation circulaire (CP). Les dimensions totales du réseau sont de $22 \times 22 \times 2.5cm^3 (0.63\lambda \times 0.63\lambda \times 0.07\lambda)$. Ce dernier présente une directivité main gauche (LH) de $10.3dBic$ et un rendement de rayonnement de 38.5%.

La Valorisation des Résultats

Les travaux menés dans le cadre de cette thèse ont été valorisés par 5 revues, 14 communications dans des conférences internationales, 2 communications dans une conférence nationale et 3 communications dans des journées thématiques nationales.

General Introduction

Background

Many emerging radio technologies require supporting multiple communications standards. For example a smart phone requires supporting GSM, UMTS, LTE, Bluetooth, WiFi, GPS,...etc. standards. In other applications, as a universal remote control, a small and directive antenna is required to separately control multiple devices depending on the remote orientation. This requires a significant effort on the antenna miniaturization while keeping an acceptable performance (in terms of bandwidth, directivity and efficiency). However, the antenna performance is limited with some fundamental limits related to its physical dimensions. Multiple researchers addressed the fundamental limits of Electrically Small Antennas (ESAs) [3]-[18]. A. H. Wheeler was the first to address these limits [3, 4]. He defined an ESA as an antenna with $ka < 1$ as shown in Figure 2, where $k = \frac{2\pi}{\lambda}$ is the wave number, λ is the free space wavelength and a is the radius of the smallest sphere enclosing the antenna.

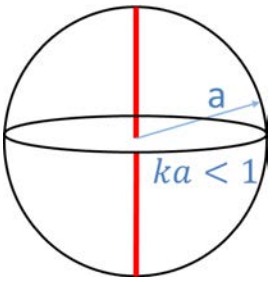

Figure 2: An illustration of an ESA definition.

The first relationship between the antenna size and its Quality Factor (Q) was presented by Chu [5] in 1948. Based on the approximations indicated by Chu this limit is given by [6]:

$$Q_{min} = \frac{1 + 2(ka)^2}{(ka)^3\big(1 + (ka)^2\big)} \tag{1}$$

However, this limit was later refined by McLean in 1996 [6]. He expressed the minimum Q of a linear ESA in free space as:

$$Q_{min} = \frac{1}{(ka)^3} + \frac{1}{(ka)} \tag{2}$$

For very small antennas, this limit can be approximated as follows:

$$Q_{min} \approx \frac{1}{(ka)^3} \tag{3}$$

As it can be noticed, the antenna Q is inversely proportional to the third power of its size factor meaning that miniaturizing the antenna will significantly increase its Q. The minimum Q of a Circularly-Polarized (CP) ESA is given by:

$$Q_{min} = \frac{1}{2}\Big(\frac{1}{(ka)^3} + \frac{2}{(ka)}\Big) \tag{4}$$

Figure 3(a) shows both Chu and McLean bound on an antenna Q as function of ka. As it can be noticed, both limits are in a very good agreement for small dimensions. However, as the antenna dimensions increases the divergence between the two limits also increases. Bode and Fano derived a bound on the antenna fractional matching bandwidth based on its Q [7]. The limit was derived for a shunt (parallel) RC load. Bode showed that the fundamental limitation on the matching network is:

$$\int_0^\infty ln(\frac{1}{|\Gamma|})dw \leqslant \frac{\pi}{RC} \tag{5}$$

where $|\Gamma|$ is the reflection coefficient magnitude. If $|\Gamma|$ is kept to $|\Gamma_m|$ inside the radial frequency band w and to unity outside this band, this limit can be written as:

$$w\ ln(\frac{1}{|\Gamma_m|}) \leqslant \frac{\pi}{RC} \tag{6}$$

Or equivalently, the fractional bandwidth $Bw = \frac{w}{w_0}$ can be given in terms of the load quality factor $Q = w_0RC$ as:

$$Bw \leqslant \frac{\pi}{Q\ ln(\frac{1}{|\Gamma_m|})} \tag{7}$$

Yaghjian and Best derived a similar bound for general single-feed (one-port) lossy or lossless linear antenna tuned to resonance or unti-resonance given by:

$$Bw = \frac{S-1}{Q\sqrt{S}} \tag{8}$$

where S is the standing wave ratio and it is related to Γ_m as:

$$S = \frac{1+|\Gamma_m|}{1-|\Gamma_m|} \tag{9}$$

Figure 3(b) shows Bode-Fano and Yaghjian-Best limits on antenna $S_{11} < -10dB$ bandwidth as a function of ka. It can be noticed that the two limits are in a good agreement for small ka (< 0.5) and as ka increases the difference between them increases. In general, due to the assumptions under-which Fano limit was derived, this limit is more optimistic than Yaghjian's one. Due to this fundamental limit, it is hard to design wide-band small antennas.

As for the antenna directivity, Harrington derived an upper bound depending on the spherical wave order N associated to the antenna radiation given by:

$$D_{max} = N^2 + 2N \tag{10}$$

Harrington also provided a relationship between the antenna size and the spherical wave order given by:

$$N = ka \tag{11}$$

However, Harrington limit was derived considering lossless antennas, hence in the case of ESAs with $ka < 0.5$ it yields negative directivity in dBi. Furthermore, it does not converge to the directivity of Huygens source. Consequently, in [19], the authors proposed a renormalization of the second part of this limit (the spherical wave order) to fulfill the directivity definition and the physical behavior of ESAs. The renormalized spherical wave order is given by:

$$N = k\big(a + \frac{\lambda}{2\pi}\big) \tag{12}$$

Figure 3(c) shows Harrington limit on the antenna directivity and the renormalized limit as a function of ka. Due to this fundamental limit, it is hard to design directive small antennas.

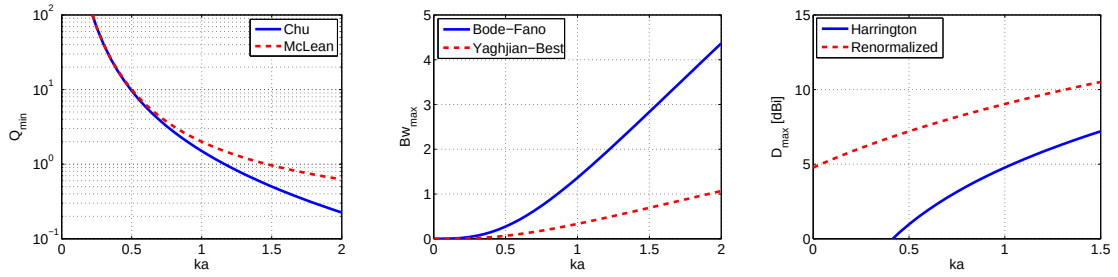

(a) (b) (c)

Figure 3: The bounds on the antenna parameters as a function of ka. (a) Minimum quality factor, (b) maximum bandwidth and (c) maximum directivity.

Now assuming a lossy antenna with a radiation efficiency of η_{rad}, MacLean minimum quality factor can be modified as follows:

$$Q_{min} = \eta_{rad}\Big(\frac{1}{(ka)^3} + \frac{1}{(ka)}\Big) \tag{13}$$

Replacing the value of Q in the bound on the antenna bandwidth given by Bode-Fano, the following bound on the antenna efficiency can be derived:

$$\eta_{rad} = \frac{\pi(ka)^3}{Bw\ ln(\frac{1}{|\Gamma_m|})\big((ka)^2+1\big)} \tag{14}$$

and by changing the value of Q in the bound on the antenna bandwidth given by Yaghjian-Best, the following bound on the antenna efficiency can be derived:

$$\eta_{rad} = \frac{(S-1)(ka)^3}{\sqrt{S}\ Bw\ \big((ka)^2+1\big)} \tag{15}$$

As it can be noticed, the antenna bandwidth is inversely proportional to the antenna relative bandwidth while it is proportional to the third power of its size factor. This means that, for a fixed dimension, there is a trade-off between the antenna bandwidth and its efficiency. Figure 4 shows the limit on antenna efficiency for different relative bandwidths. Since Fano's limit is more optimistic concerning the obtainable bandwidth, it is also more optimistic concerning the attainable efficiency.

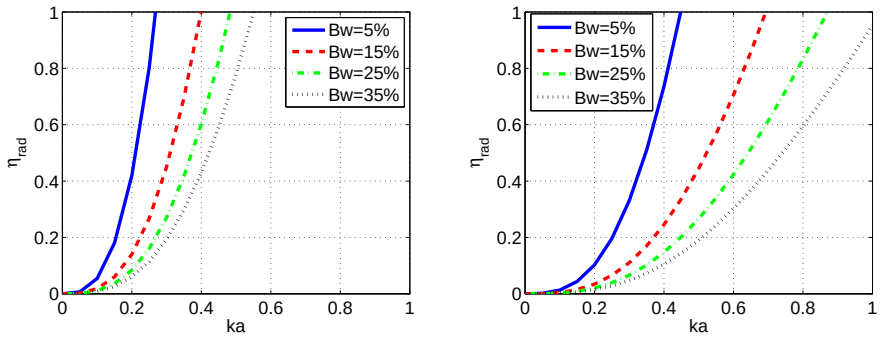

Figure 4: The bound on the antenna efficiency. (a) Considering Bode-Fano limit on Q and (b) considering Yaghjian-best limit on Q.

Objectives

In the previous section it was shown that the antenna performance (in terms of bandwidth, directivity and efficiency) is limited by the fundamental limits related to its dimensions. This work is done in the framework of two French National Research Agency (ANR) Projects. The first project, systèmes d'antenne capteur miniature "SENSAS", aims to study, implement and characterize new ultra-miniature and smart antennas, that are able to adapt to their changing environment, and for some of them, including detection capabilities. The project combines the expertise of three research laboratories CEA-Leti, IETR and LEAT, and two companies, Technicolor and SENSeOR [1]. The second project, super-directivité pOur le Contrôle du Rayonnement des objets communicants, aimes to improve the directivity of ESAs. It brings together research teams from CEA-Leti and IETR and two industrial partners (Movea and TAGSYS) [2]. In this context, the main objective of this thesis is the design of ESAs approaching, or exceeding, the well known fundamental limits on antenna bandwidth and directivity.

Layout

This thesis is organized in four chapters.
In the first chapter, a the definition of non-Foster circuits is presented. A literature review on the different aspect and applications of non-Foster circuits is given showing that using this kind of circuits can help designing ESAs overcoming the theoretical limits on Q and bandwidth.
In the second chapter, a non-Foster circuit is designed and characterized in terms of losses, stability, linearity and inter-modulation. Then, the circuit is ued to match to ILAs showing a significantly wide-band, stable, low-noise performance.
In the third chapter, superdirective arrays are defined and their different optimization methods are presented. The state of the art on this kind of arrays is summarized showing that in some parasitic arrays a frequency optimization is required while in others resistive loads are applied which highly reduces the antenna efficiency.
In the fourth chapter, a design approach for parasitic superdirective antenna arrays is presented. A parametric analysis on dipole-based arrays is performed to investigate

the practical limitations. The method is later used to design multiple superdirective ESA-based arrays surpassing Harrington's limit on antenna directivity. Then, the integration of superdirective ESAs in PCBs is investigated via different scenarios. Next, measuring superdirective ESAs integrated in PCBs is also investigated via different feeding configurations. Later, a new strategy is presented to obtain a 3D small-size broadside array using compact end-fire unit-elements for UHF band. Afterward, a two-element parasitic superdirective antenna array is designed and integrated in a compact 2×2 planar antenna array. Finally, a compact CP planar array for $866MHz$ band based on superdirective arrays is presented.

Chapter 1

Non-Foster Matched Antennas, Literature Review

1.1 Introduction

We previously mentioned Bode-Fano fundamental limit on the antenna bandwidth when a passive matching circuit is used. One solution to surpass this limit is using a non-Foster matching circuit. Let us consider the example of a small monopole that can be modeled as a resistor in series with a capacitance (for example $1pF$). To eliminate this antenna's reactance, it can be connected in series with an inductor (passive matching) or a negative capacitor (non-Foster matching). While the first solution eliminates the antenna's reactance at a single frequency, the second does that for the whole band and therefore has a much wider bandwidth (see Figure 1.1).

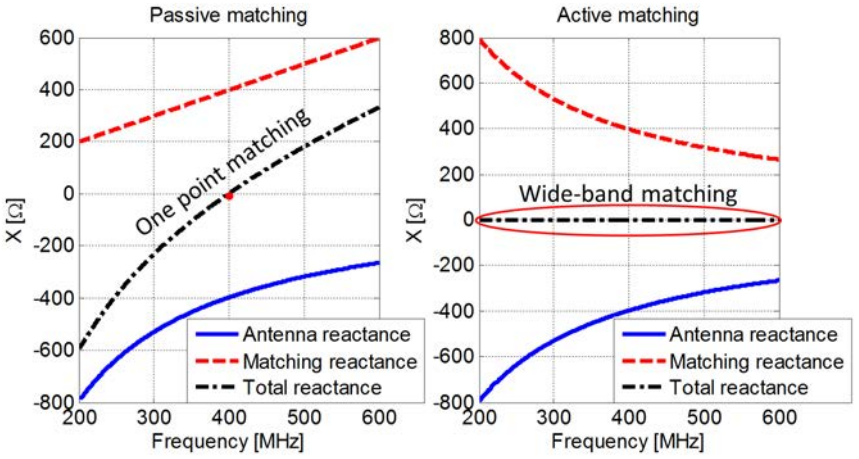

Figure 1.1: Passive matching vs. non-Foster matching of a short monopole.

Hirvonen et al. presented the bandwidth limitations for dipoles matched with negative impedances [20]. It was shown that even though in reality infinite bandwidths cannot be achieved, the bandwidth achieved with one negative capacitor demonstrates a larger than the ones obtained when tuning with infinite passive components. Figure 1.2 shows that, for example, for an antenna with $ka = 0.4$, the achieved bandwidth for $VSWR = 1.5$ is 15% using infinite passive tuning while it is 24% using a negative capacitor. The "non-Foster" notation comes from Foster

theorem.

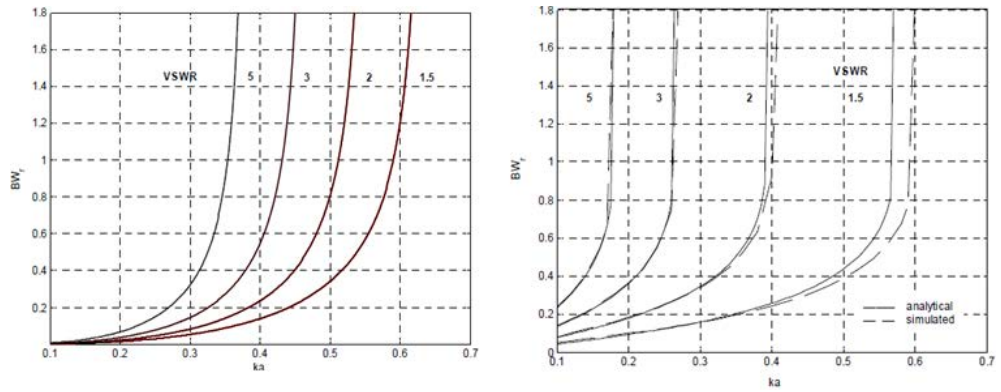

Figure 1.2: Dipoles bandwidth limits as presented in [20]. (Left) Matching with infinite number of LC and (right) matching with a negative capacitor.

The rest of the chapter is organized as follows: First Foster theorem is presented. Then, Negative Impedance Converters (NICs) are defined and their applications are given. Later, NIC stability is addressed. Finally, some conclusions are drawn.

1.2 Foster Theorem

This theory developed by Roland M. Foster in 1924 states that "the reactance of a passive, lossless two-terminal (one-port) network always strictly monotonically increases with frequency" [21]. In Figure 1.3 we show different examples of Foster nature circuits as an inductor a capacitor or any combination of parallel or series connection of them. As it can be noticed, in all cases, the reactance monotonically increases with the frequency.

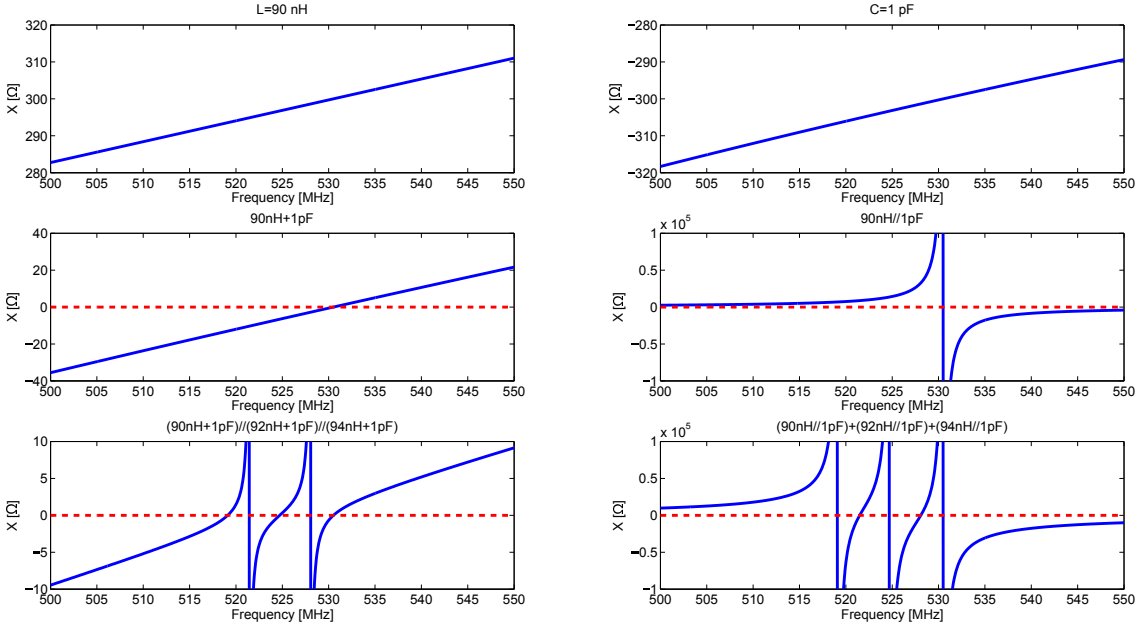

Figure 1.3: An illustration of different Foster nature components.

The active circuits that do not follow the Foster theory are called non-Foster circuits. Non-Foster circuits can be realized using Negative Impedance Converters (NICs).

1.3 NIC Definition

They are active circuits which introduce a 180^o phase difference between their input current and voltage, and therefore, operate as negative impedances. Figure 1.4 shows the function of these circuits. If a load of Z_L is connected to the output port, an impedance of $Z_{in} = -kZ_L$, where $k > 0$, can be observed at the input port. The idea of negative impedances goes back to 1920 (Marius Latour) [22].

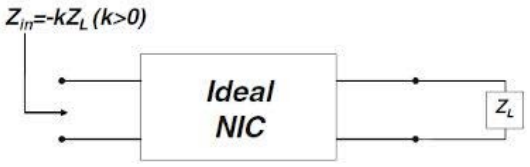

Figure 1.4: An illustration of a NIC function.

The first NIC (E1) was built using vacuum tubes as shown in Figure 1.5 in 1950 [23]. It was used as a signal repeater for telephone lines and it achieved a transmission gains of about $10dB$. When a resistance of $Z_N = 1800$ and a network is connected to terminals 3 and 4, an impedance of $-0.1Z_N$ is seen at terminals 1 and 2.

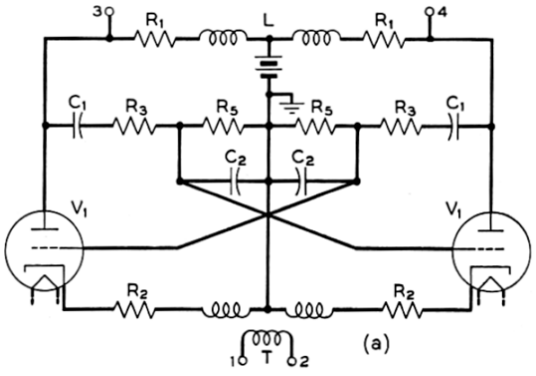

Figure 1.5: A schematic of the first realized NIC (E1).

The first transistor-based NICs were proposed by J.G. Linvill in 1953 [24]. Two types of NICs were built balanced (the output is not taken reference to the ground) and unbalanced (the output is taken reference to the ground). Figure 1.6 shows the balanced NICs, while Figure 1.7 shows the unbalanced NICs. The input impedance of the four circuits is proportional to the negative of the load, i.e. $(Z_{in} = -kZ_L)$.

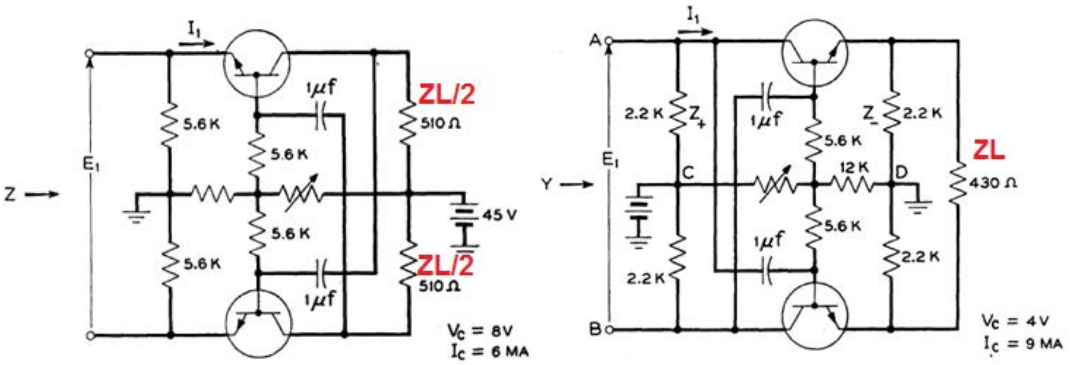

(a) (b)

Figure 1.6: Linvill balanced NICs. (a) Open circuit stable and (b) short circuit stable.

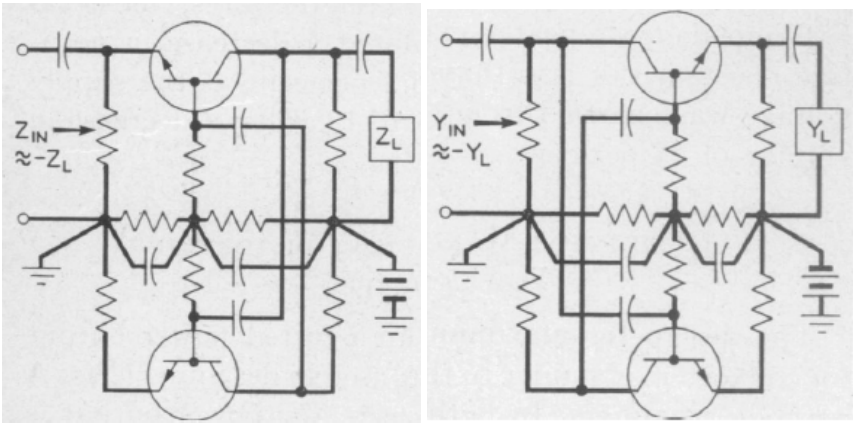

(a) (b)

Figure 1.7: Linvill unbalanced NICs. (a) Open circuit stable and (b) short circuit stable.

A catalog for all previously known NICs was presented by Sussman-Fort in 1998 as shown in Figure 1.8 [25]. The author show that the value of k in the circuits IVa, IVb, VI and VII is independent from g_m while the other circuits requires g_m to be finite to achieve their respective k.

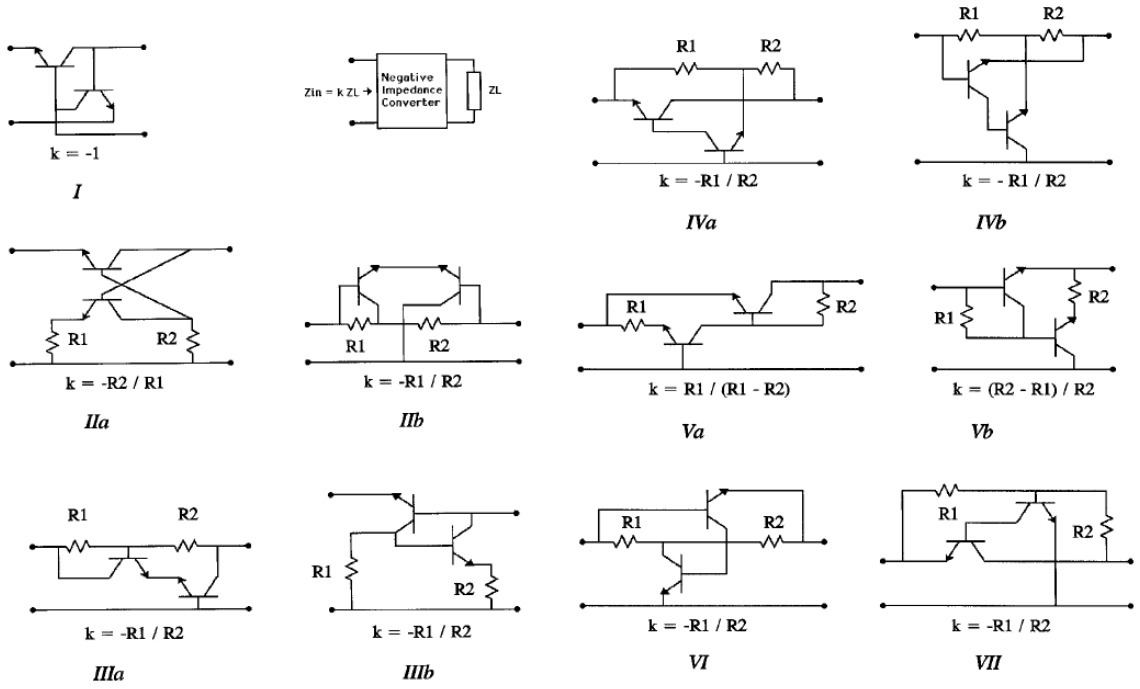

Figure 1.8: The catalog of NICs circuits given by Sussman-Fort in [25].

1.4 NIC Applications

Although the theory of NICs has been around for quite a long time, their use with antennas is relatively recent. NICs can be used for antenna impedance matching or controlling its radiation pattern. They can also be used for expanding the bandwidth of metamatirials or Artificial Magnetic Conductors (AMCs). NICs can also be used to achieve small and wide-band antenna arrays.

1.4.1 Antenna Matching

One of the most important applications of the NICs is in the antenna matching networks to overcome the theoratical bounds on antenna bandwidth. A.J. Bahr studied the effect of an active coupling network on the Noise Figure (NF) of a receiving antenna [26]. As an example a short monopole for the $(30 - 60)MHz$ and an operational amplifier-based NIC was considered. Simulation results showed that NF can be improved up to $25dB$, while experimental results showed an NF improvement of $6dB$ as in Figure 1.9. It can be noticed that in the measurement NF improvement is only up to $45MHz$.

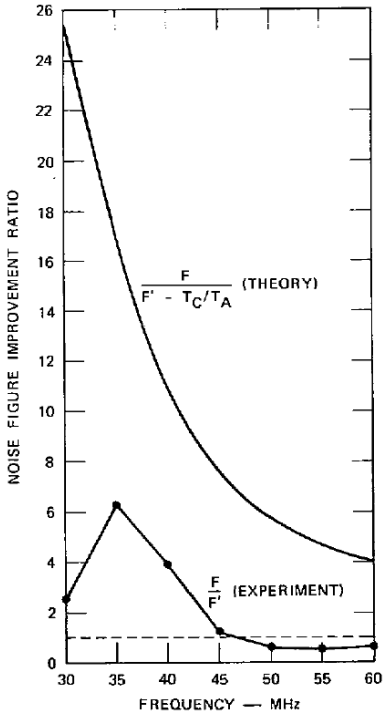

Figure 1.9: Noise figure improvement as presented by Bahr in [26].

Sussman-Fort presented the first experimental confirmation of the non-Foster impedance matching for signal reception [27]. A negative capacitor based on Linvill circuit was used to match a 6 inch monopole antenna. A Signal to Noise Ratio (SNR) improvement up to $6dB$ was reported for the $(20-110)MHz$ band compared to the same antenna without matching as shown in Figure 1.10.

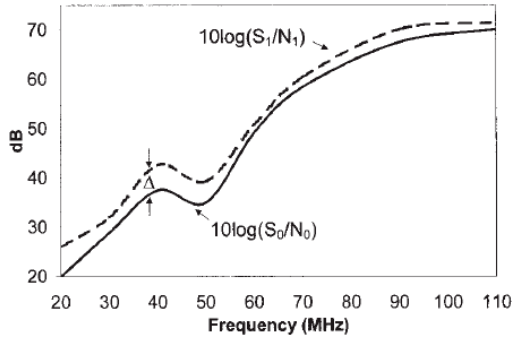

Figure 1.10: SNR improvement as presented by Sussman-Fort in [27].

Sussman-Fort and Rudish designed a negative LC circuit to match an antenna for transmission [28]. Figure 1.11 shows a schematic of the circuit with the antenna model and the experimental S_{21} improvement. It was shown that non-Foster matching bypass the gain-bandwidth constraints of passive matching.

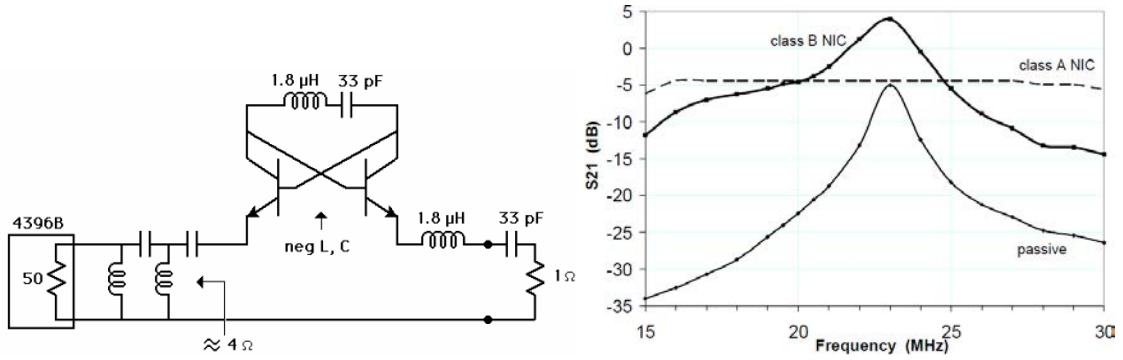

(a) (b)

Figure 1.11: The circuit designed by Sussman-Fort Rudisha [28]. (a) Schematic of the circuit and (b) its performance.

Koulouridis and Volakis were able to optimize a non-Foster circuit to match a 6 inch loop antenna [29]. The antenna's original $50MHz$ bandwidth is augmented to $320MHz$ and the central frequency is decreased from $680MHz$ to $400MHz$ as shown in Figure 1.12. The authors assumed ideal non-Foster elements in the matching network.

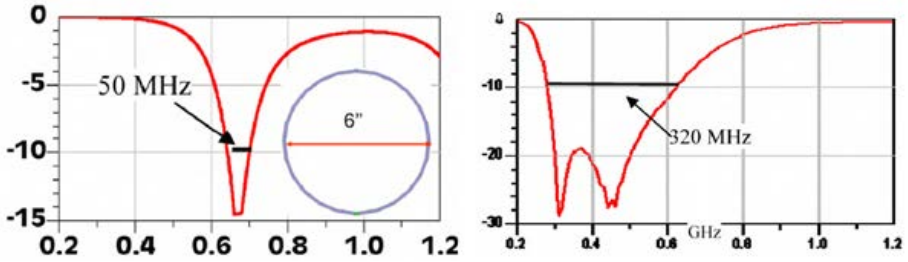

Figure 1.12: Antenna input reflection coefficient as presented in [29]. (Left) Antenna only and (right) antenna with non-Foster matching circuit.

Yifeng et al. designed a negative L//C circuit to match a printed half-loop antenna [30]. A non-Foster circuit was designed using four transistors. However, the antenna was only simulated in HFSS with ideal non-Foster elements and the simulation results are given in Figure 1.13. As it can be noticed, the use of the non-Foster circuit matches the antenna in the $(0-800)MHz$ band. Furthermore, at $200MHz$ the non-Foster matched antenna reveals a gain improvement of around $3dB$ compared to the same antenna without matching.

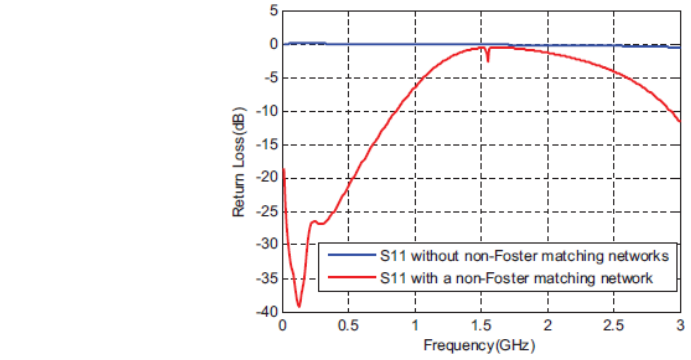

(a)

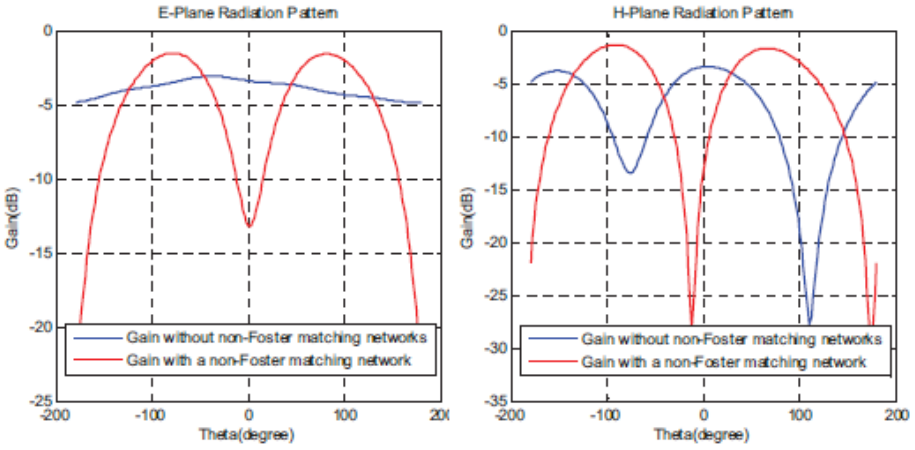

(b)

Figure 1.13: The obtained results by Yifeng et al. in [30]. (a) Input reflection coefficient magnitude and (b) radiation pattern at $200MHz$ in E and H plane.

Li et al. presented an operational amplifier-based NIC for ESA matching in the receive mode [31] as shown in Figure 1.14. The antenna is modeled as a $15pF$ capacitor. Experimental results show that the antenna achieves a good voltage gain A_v and SNR up to $50MHz$. The analytic results also show that the antenna is stable.

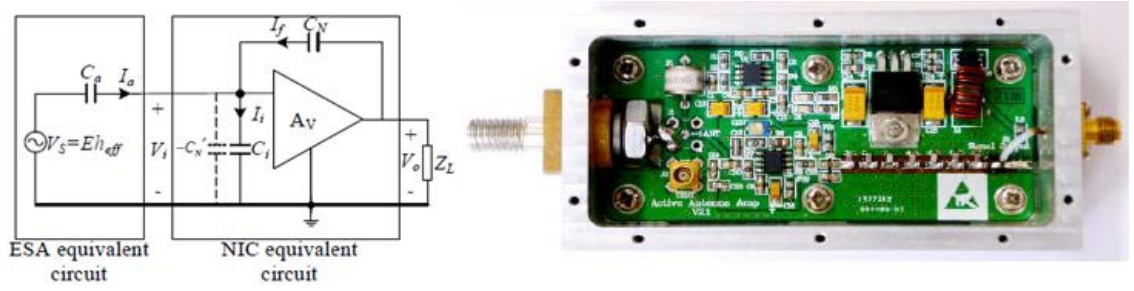

Figure 1.14: The designed NIC in [31]. (Left) A schematic representation and (right) the fabricated prototype.

White et al. designed, simulated and measured a variable negative capacitor based on Linvills balanced circuit, for matching a 15-cm monopole antenna as shown in Figure 1.15 [32]. The active antenna was used for FM radio reception and the

received signal is boosted by about $15dB$. As it can be seen from the figure by controlling the varactor voltage, the value of the obtained negative capacitance changes and the so does the received power level.

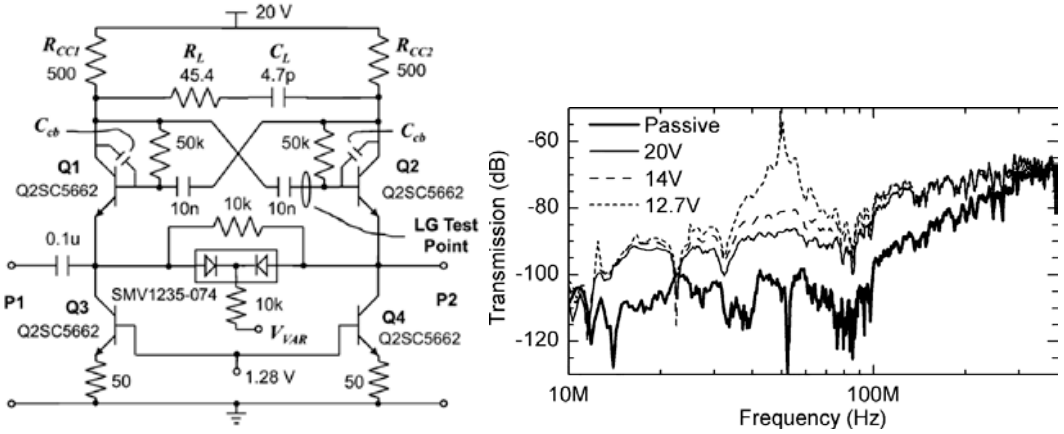

Figure 1.15: The performance of the antenna presented by White et al. [32]. (a) Schematic and (b) received signal level.

Mirzaei and Eleftheriades fabricated a metamaterial inspired antenna matched with a negative L//C circuit with the possibility of negative capacitance tuning (Figure 1.16) [33]. It can be seen from the obtained results that in all cases $S_{11} > 0dB$ at low frequencies implying that the circuit is unstable.

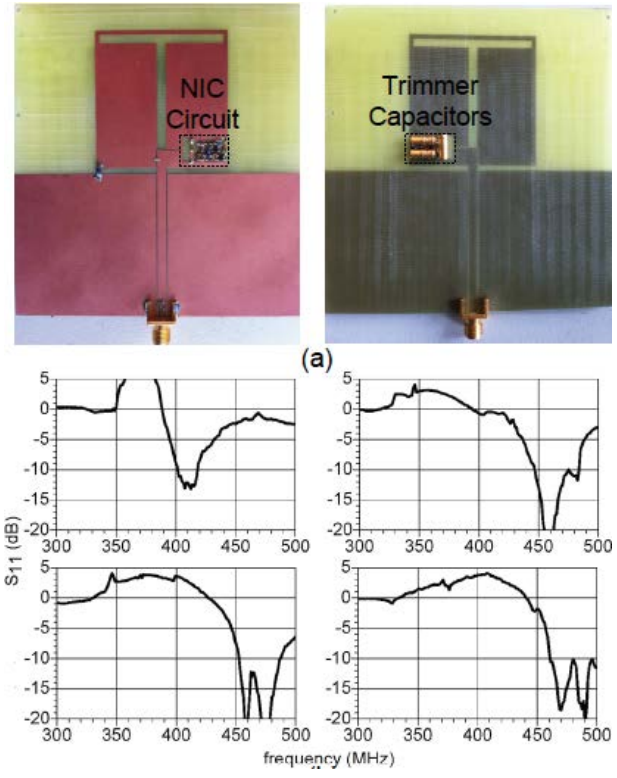

Figure 1.16: The antenna presented by Mirzaei and Eleftheriades in [33].

G. Mishra et al. presented a Bowtie antenna covering $(0.6 - 1.1)GHz$ frequency band for which it satisfies the definition of ESA using a non-Foster circuit [34]. The antenna is stable for the entire matched band. The measured realized gain of the NIC matched antenna is better than the passive antenna's one starting from $0.82GHz$ and the average gain improvement is about $4dB$ as shown in Figure 1.17.

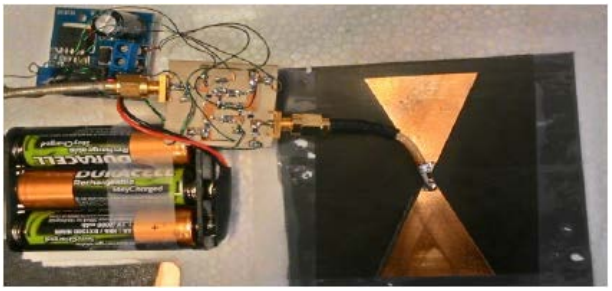

(a)

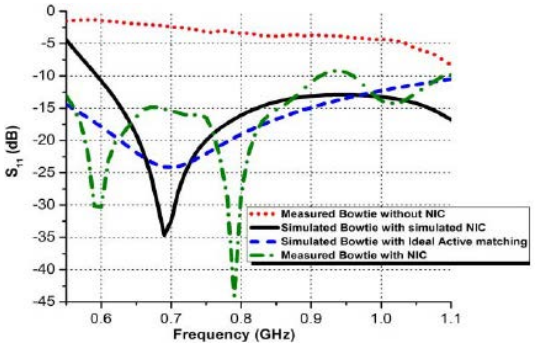

(b)

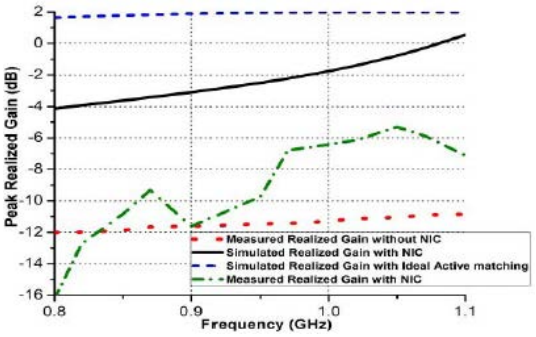

(c)

Figure 1.17: The proposed antenna in [34]. (a) The antenna geometry, (b) input reflection coefficient magnitude and (c) the realized gain.

M. M. Jacob et al. studied the non-linear effect of non-Foster matching networks [35]. Both simulation and measurement results showed that increasing the input power (RF) degrades the performance of the non-Foster matched antenna in terms of the matching and the gain as shown in Figure 1.18.

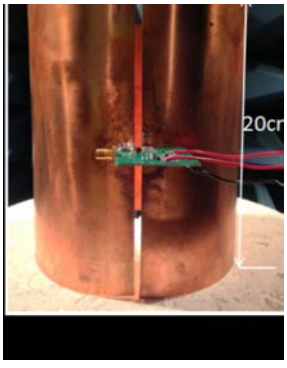

(a)

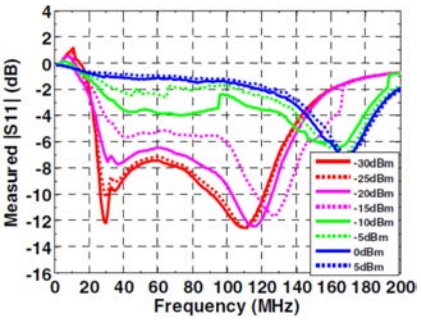

(b)

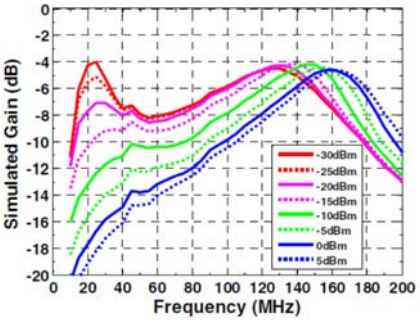

(c)

Figure 1.18: The proposed antenna in [35]. (a) The antenna geometry, (b) input reflection coefficient magnitude and (c) the realized gain.

Finally, Nagarkoti et al. discussed the effect of a non-Foster matching network on the antenna Q [36]. The non-Foster circuit is realized based on tunnel diode operating in the negative resistance region and the antenna is modeled by its equivalent lumped circuit (1.19). It was shown that the non-Foster matched antenna impedance bandwidth exceeds Bode-Fano limit.

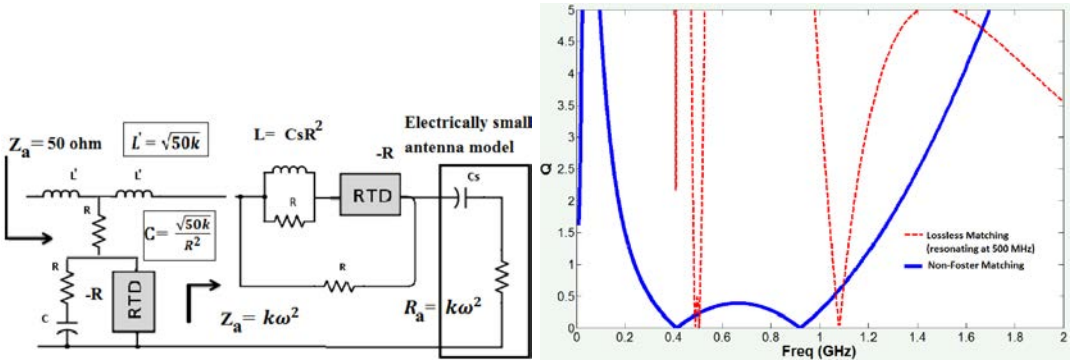

(a) (b)

Figure 1.19: The proposed active antenna in [36]. (a) The antenna and non-Foster circuit, (b) the measured Q.

O. O. Tade et al. presented a Livill-based NIC functional up to $1.5GHz$ [37]. The NIC was used to achieve a negative capacitance of $3.9pF$. The designed circuit S parameters are given in Figure 1.20.

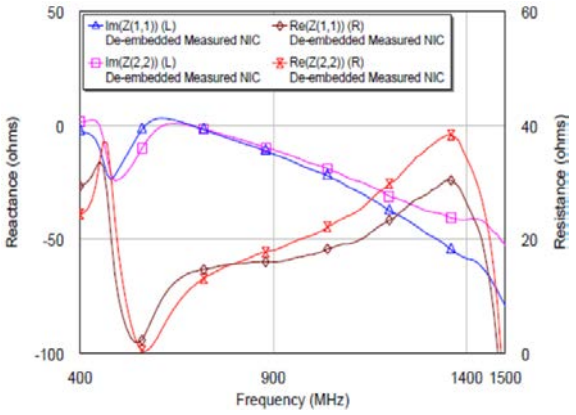

Figure 1.20: The circuit designed in [37] S parameters.

Instead of using the non-Foster circuits at the input of the antennas, they can be directly embedded in the antenna structure, some examples will be presented in the next section.

1.4.2 Antenna Loading

Koulouridis and Stephanopoulos have implemented both loading and matching a patch antenna with non-Foster circuits [38]. The antenna resonance frequency is reduced from $1.6GHz$ to $0.5GHz$ with a much wider bandwidth (Figure 1.21).

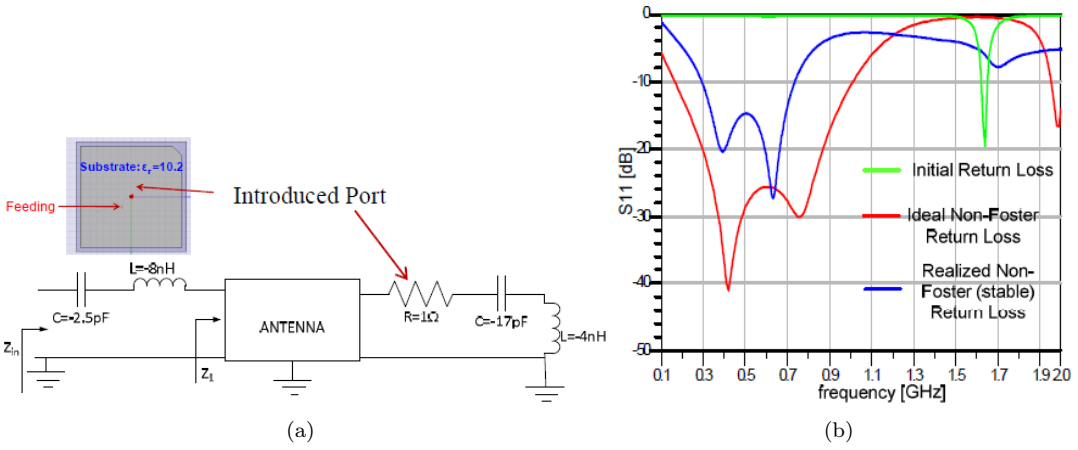

(a) (b)

Figure 1.21: The performance of the antenna presented by Koulouridis and Stephanopoulos [38]. (a) Schematic and (b) S11.

Ugarte-Munoz et al. studied the sensitivity of the reflection coefficient of a NIC-loaded antenna to the changes of the parameters of the NIC [39]. As an example the authors have taken an ordinary patch, a shorted patch, and a multi-band patch as shown in Figure 1.22. As it can be seen, depending on the antenna geometry, some optimal places exist for loading it. It should be noticed that the blue color indicates that the antenna is least sensitive while it is most sensitive in the case of a red color. For example, in the case of an ordinary patch, the antenna is least sensitive when it is loaded the furthest from the port. On the other hand, the shorted-patch is less sensitive when loaded next to the feeding port.

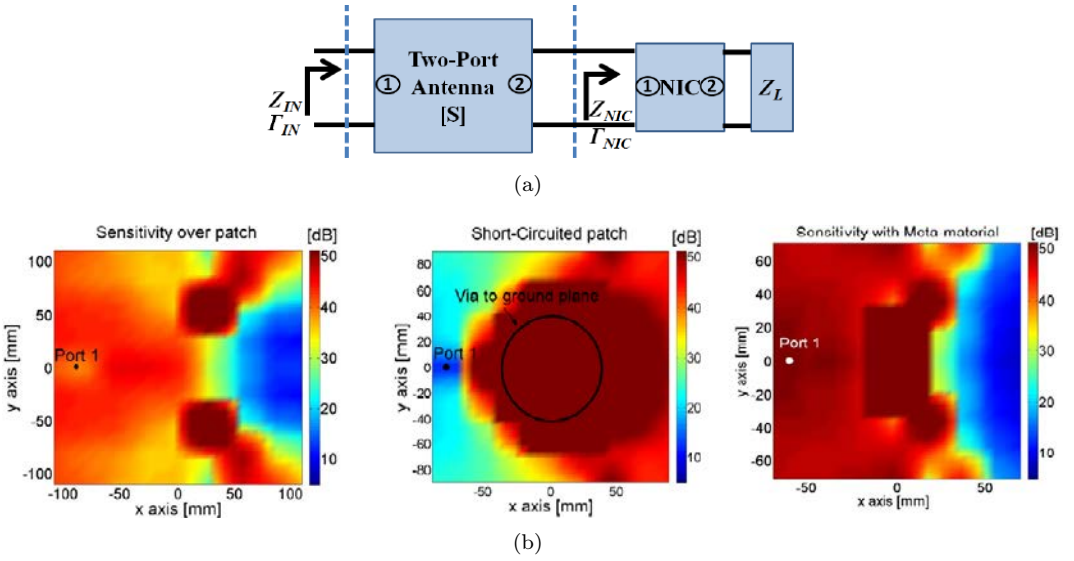

(a) (b)

Figure 1.22: The study presented by Ugarte-Munoz et al. [39]. (a) The methodology and (b) the obtained results in terms of the antenna sensitivity to the changes in the NIC parameters.

H. Mirzaei and G. V. Eleftheriades experimentally tested a printed monopole loaded with a non-Foster circuit [40]. The antenna has been used for receiving a signal around 375MHz. The obtained results are shown in Figure 1.23.

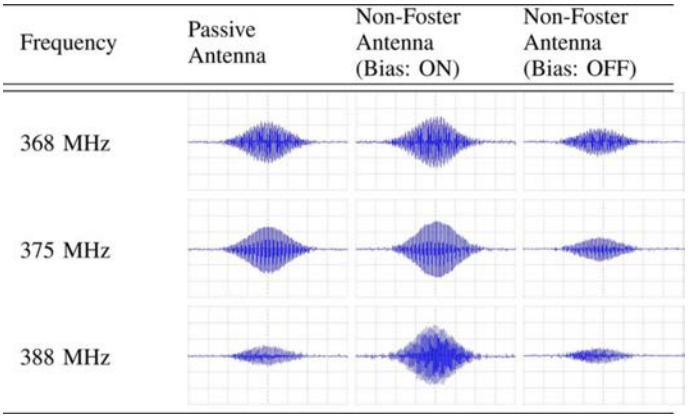

Figure 1.23: The obtained results in [40].

K. A. Obeidat et al. have proposed applying the Theory of Characteristic Modes (TCM) and non-Foster loading on multi-port antennas for broadband performance in terms of impedance and radiation pattern [41]. The studied scenario and the obtained results are shown in Figure 1.24.

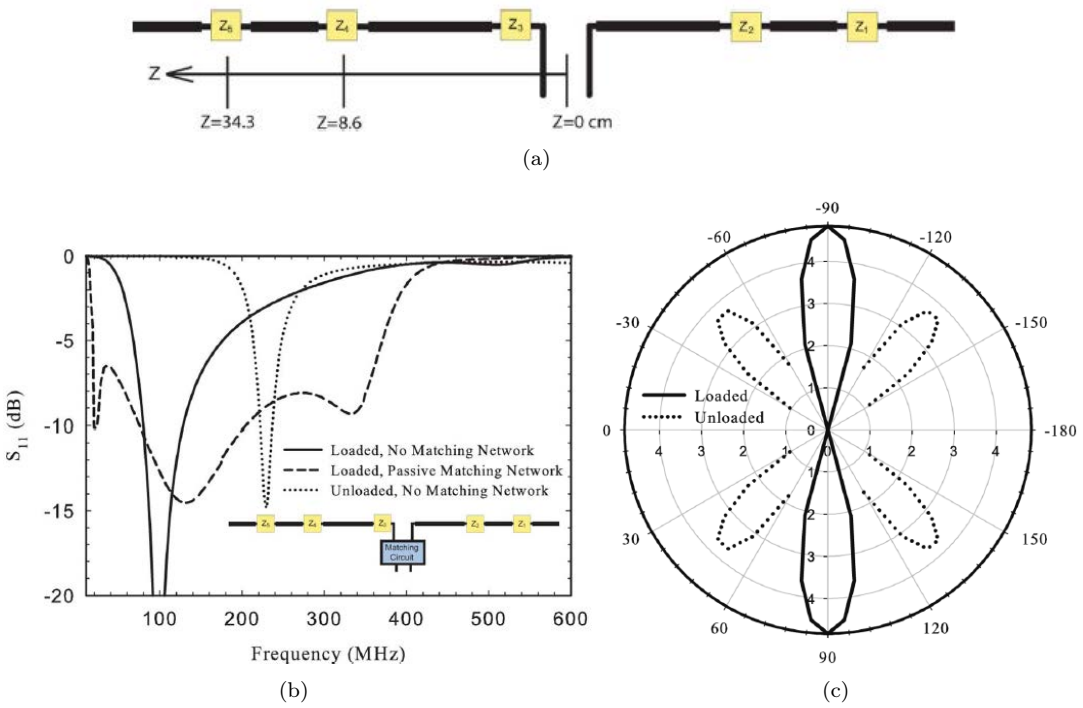

Figure 1.24: The studied scenario in [41]. (a) The antenna geometry, (b) input reflection coefficient magnitude and (c) the radiation pattern.

1.4.3 Other Applications

Gregoire et al. examined the expansion of AMCs bandwidth using negative inductors [42]. An AMC prototype for the VHF-UHF band has been realized and tested revealing a bandwidth greater than 80% as shown in Figure 1.25.

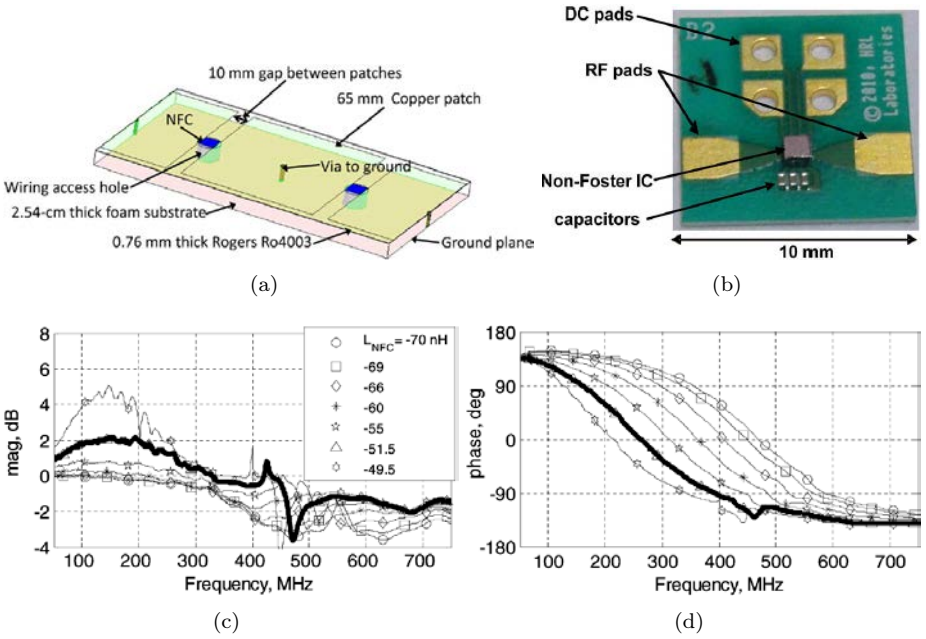

Figure 1.25: Performance of non-Foster loaded AMC structure presented by Gregoire et al. in [42]. (a) AMC unit-cell structure, (b) the non-Foster circuit, (c) the reflection magnitude in dB and (d) the reflection phase.

J. Long and D. Sievenpiper proposed using non-Foster circuits to reduce the dispersion of High Impedance Surfaces (HISs) [43]. Different ideal non-Foster L//C were used for obtaining different propagation indexes. Loaded HISs are divergence free in the band (180-450)MHz as shown in Figure 1.26.

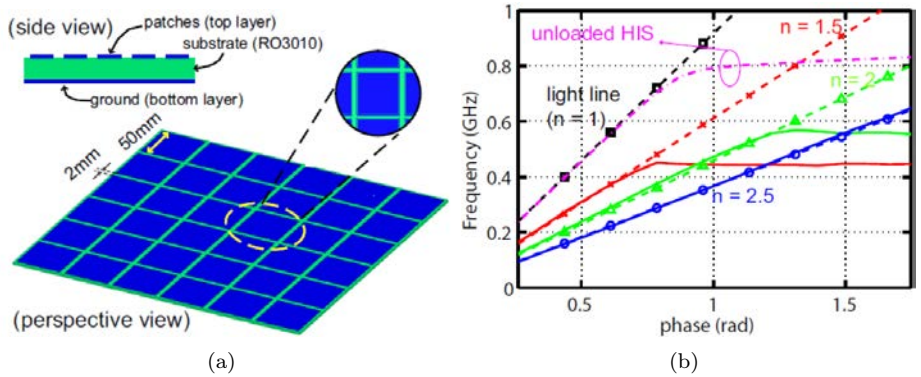

Figure 1.26: Performance of HIS structure presented by Long and D. Sievenpiper in [43]. (a) HIS structure and (b) performance.

Non-Foster circuits can also be used for increasing the operation bandwidth of Split-Ring Resonators (SRRs) [44] and many other applications as in [45, 46, 47, 48].

1.5 NIC Stability

One of the main difficulties of designing non-Foster circuits is their inherent unstablity due to the positive feedbak. Stephen D. Stearns, studied the stability of

non-Foster circuits and proposed that the circuit stability depends on its time domain behavior [49, 50]. He showed that for practical non-Foster circuits good results were achieved with modified Nyquist test, whereas numerical tests for external stability at the port as the Rollett factor ($K, |\Delta|$), Edward-Sinsky factor (μ), and B factor are problematic. This is because linear systems have hidden modes. that can be unstable but cannot be detected at ports. For a reminder the formula of the different stability factors are given below.

$$|\Delta| = |S_{11}S_{22} - S_{21}S_{12}| < 1 \tag{1.1}$$

$$K = \frac{1 - |S_{11}|^2 - |S_{22}|^2 + |\Delta|^2}{2|S_{12}S_{21}|} \geq 1 \tag{1.2}$$

$$B_1 = 1 + |S_{11}|^2 - |S_{22}|^2 - |\Delta|^2 > 0 \tag{1.3}$$

$$B_2 = 1 + |S_{22}|^2 - |S_{11}|^2 - |\Delta|^2 > 0 \tag{1.4}$$

$$\mu_1 = \frac{1 - |S_{11}|^2}{|S_{22} - \Delta S_{11}^*| + |S_{12}S_{21}|} \geq 1 \tag{1.5}$$

$$\mu_2 = \frac{1 - |S_{22}|^2}{|S_{11} - \Delta S_{22}^*| + |S_{12}S_{21}|} \geq 1 \tag{1.6}$$

Both K and μ factors can be derived from setting the input reflection magnitude in a two-port network to be less than unity. The advantage of μ factor is that only a single parameter has to be evaluated, unlike K factor that needs an auxiliary factor ($|\Delta|$). Furthermore, the magnitude of μ is a measure of the stability (a higher μ means better stability).
J. Loncar et al. studied the effect of transmission lines on the stability of networks containing ideal negative capacitors [51]. The authors showed that a network of negative and positive capacitors is stable if the overall capacitance is positive. However, inserting a transmission line in the middle yields the circuit unstable.

1.6 Conclusion

In this chapter we have presented a brief definition of non-Foster circuits and their different applications in antenna engineering. We have shown that non-Foter matching can surpass the fundamental limits on antenna Q and bandwidth. We have also shown that this type of matching can enhance the antenna NF, SNR and gain. We have equally shown that transistor-based NICs can achieve negative impedances up to high frequencies. We have arisen the stability issues of these kind of circuits. Most of the presented examples showed the feasibility of non-Foster circuits in the low UHF band(up till around $400MHz$). However, the realization of this type of circuits is more complicated at higher frequencies. This is mainly due to the parasitic elements and the low quality factors of surface-mount components. In the next chapter we will present a NIC circuit and its use for matching small antennas around $900MHz$.

Chapter 2

Realization of Negative Impedance Convertor (NIC)-Matched Antennas

2.1 Introduction

Non-Foster circuits can be realized by using Negative Impedance Inverters (NIIs) or Negative Impedance Convertors (NICs). On the other hands, NICs can be realized using Operational Amplifiers (OpAmps) [53, 54], Bipolar Junction Transistors (BJTs) [55, 56], Field Effect Transistors (FETs) [57] and so on. OpAmps-based NICs can be very interesting in low frequencies range. However, their use in high frequency ranges is limited by their limited bandwidth. On the other hand, transistor-based NICs are very interesting in high frequency ranges. In this chapter, first the possibility of realizing a NIC using OpAmps in the UHF band is investigated. Then a very small negative capacitor (high reactance) is realized by exploiting the parasitic capacitance of the transistors in order to match these antennas requiring high reactance values. The realistic implementation as linearity, losses, stability, intermodulation and gain compression issues are discussed. Next, the NIC is used to match a small Inverted-L Antenna (ILA) and the antenna experimental results are presented. Later, the NIC is also used to match the same antenna however on a smaller PCB. Finally, some conclusions are drawn.

2.2 OpAmp-Based NIC

A schematic of an OpAmp-based NIC is given in Figure 2.1. The functionality of this circuit can be derived as follows:

$$V^- = V^+ = V_{in} \tag{2.1}$$

$$V^- = V_{out}\frac{R_2}{R_1 + R_2} \tag{2.2}$$

From equations (2.1) and (2.2) we get:

$$V_{out} = A_v V_{in} = (1 + \frac{R_1}{R_2})V_{in} \tag{2.3}$$

$$\Rightarrow I_{in} = \frac{V_{in} - V_{out}}{Z_L} = -\frac{R_1}{R_2 Z_L}V_{in} \tag{2.4}$$

$$\Rightarrow Z_{in} = \frac{V_{in}}{I_{in}} = -\frac{R_2}{R_1}Z_L \tag{2.5}$$

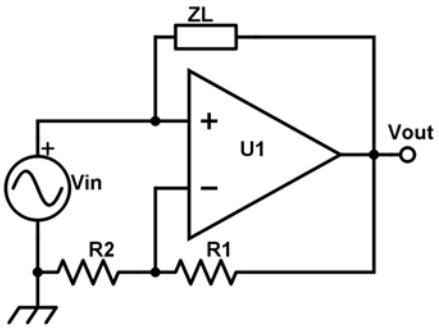

Figure 2.1: A schematic of OpAmp-based NIC.

Looking into the commercial OmAmps we found that AD8009 [58] from ANALOG DEVICES has a unity gain bandwidth of $1GHz$. An amplifier test circuit (Figure 2.2) has been realized. It is similar to the examples of non inverting amplifiers given in the data sheet. The expected gain is $0dB$ between the RF connectors, and the amplifier voltage gain is +2. Figure 2.3(a) shows that, similarly to the response behavior given in the data sheet, the amplitude has a resonance around $400MHz$. This resonance can be seen by the gain increment around this frequency. Moreover, the phase response is already affected at the low frequencies as can be seen from Figure 2.3(b); for an OpAmp well suited for the targeted band the phase should be around zero. Even-though, an improved circuit board may reduce parasitic capacitors, the data sheet shows that it is not possible to avoid such a resonance in the band of interest. A main condition to provide a negative impedance conversion with an OpAmp is to ensure a positive unity gain in the frequency range as in Equation 2.3. Hence, a high speed OpAmp as the AD8009 is unsuitable due to the important phase shift. Up to our knowledge, no better (in terms of bandwidth) OpAmps are available in the market.

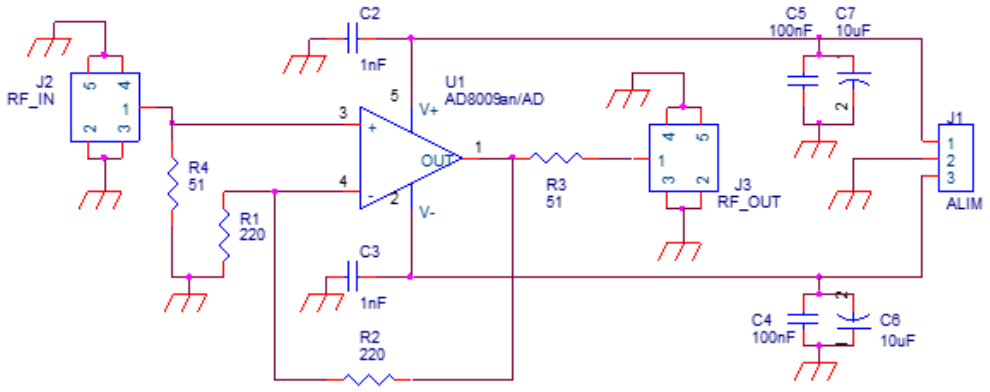

Figure 2.2: The OpAmp test circuit.

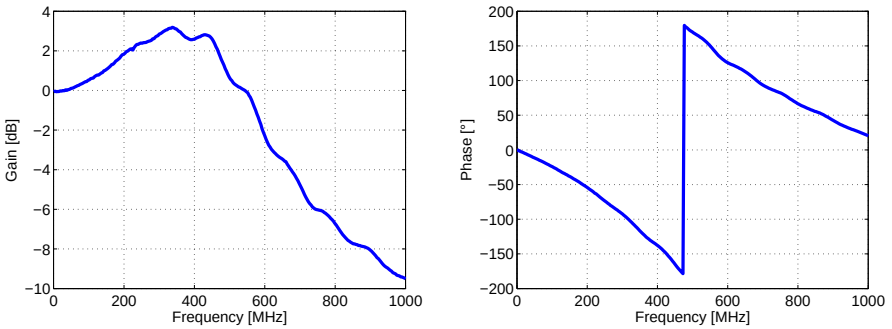

(a) (b)

Figure 2.3: The measured results of the OpAmp test circuit. (a) Gain and (b) phase.

2.3 Transistor-Based NIC

Looking into the available literature it can be seen that Linvill NIC [24] is the most used topology for obtaining a negative impedance. A schematic of Linvill circuit is given in Figure 2.4(a). The obtained impedance in this kind of circuits was analytically drawn in [59] by taking into account the transistor T-model (the emitter and base are represented by their resistors r_e and r_b while the collector is represented by a current controlled current source in parallel with the collector resistor r_c) shown in Figure 2.4(b). It should be noticed that Z_d is the DC blocking capacitor in the feedback path, Z_g is equivalent to the base current setting resistances. It can be found that:

$$Z_1 = \frac{V_1}{I_1} = 2r_e + 2(1-\alpha)r_b + \frac{2Z_g(2Z_d + Z_A)(1-\alpha)}{2Z_g + 2Z_d + Z_A} - \frac{2\alpha Z_A Z_g}{2Z_g + 2Z_d + Z_A} \tag{2.6}$$

and when $Z_d = 0$:

$$Z_1 = 2r_e + 2(1-\alpha)r_b + \frac{2Z_A Z_g(1-2\alpha)}{2Z_g + Z_A} = 2r_e + 2(1-\alpha)r_b + Z_N(1-2\alpha) \tag{2.7}$$

where $Z_N = \frac{2Z_A Z_g}{2Z_g + Z_A}$
Now assuming a good transistor: $\alpha = \frac{\beta}{\beta+1} \approx 1$ and $r_e \approx 0$ we can see that the input impedance can be written as:

$$Z_1 \approx -Z_N \tag{2.8}$$

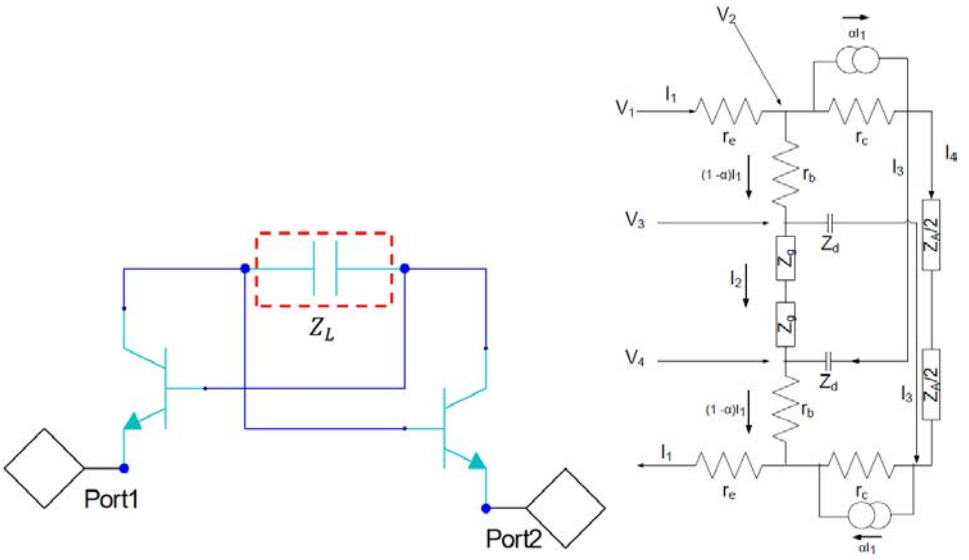

(a) (b)

Figure 2.4: Schematic of Linvill NIC. (a) A general one and (b) by taking into account transistor T-model.

However, in practice the obtained impedance depends of the biasing conditions of the transistors. Moreover, the design of NIC circuits is a very complicated issue. This design becomes even more challenging when targeting at higher frequencies (due to the active components non-linearity) and when targeting at high impedance values (due to the parasitic elements).

2.4 NIC Realization

2.4.1 Circuit Topology

Keum Su Song is one of the few authors detailing the functionality of the circuit [52]. The designed circuit therein to obtain a negative capacitor of $6.8pF$ around $300MHz$ is given in Figure 2.5. As it can be noticed, an inductor is connected in parallel with the feedback capacitor for low frequency stabilization. The biasing of the two transistors are separated via a capacitor of $680pF$. This capacitor is, in turn, connected in series with a parallel RL circuit for high frequency stabilization. High inductance and small capacitance are used as RF chock. Finally, capacitors of $680pF$ are used for DC blocking.

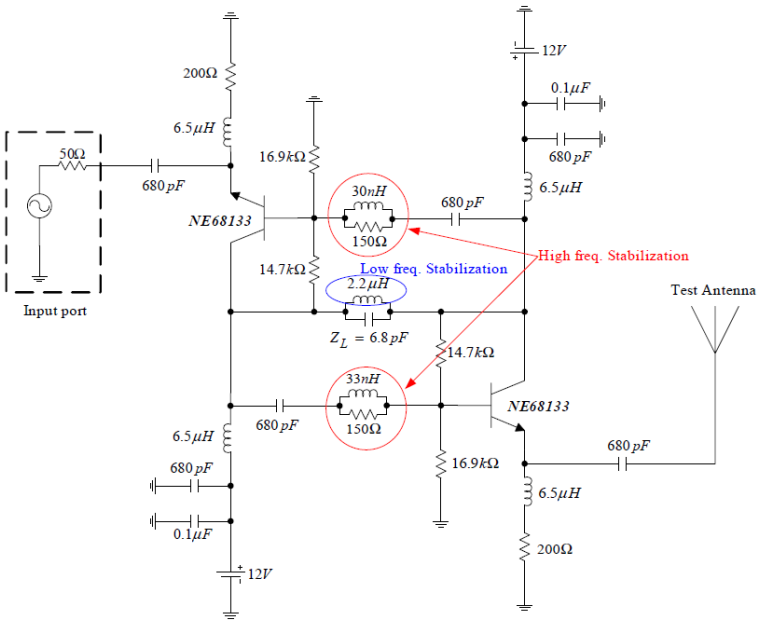

Figure 2.5: A schematic of the stabilized NIC in [52].

We started our work with the simulation of the same circuit with ANSYS Designer to investigate its performance. The simulation is done by including the transistor Pspice model while the lumped components are assumed to be ideal. The obtained results shown in Figure 2.6 show that the circuit has a very low frequency oscillation (seen as $S_{11} > 0dB$) around $30MHz$. As it can also be noticed the circuit presents a non-Foster behavior (the imaginary part of the impedance decreases with the frequency) till $834MHz$. As for the circuit resistance (losses), it increases with the frequency till $2.52GHz$ when it stabilizes.

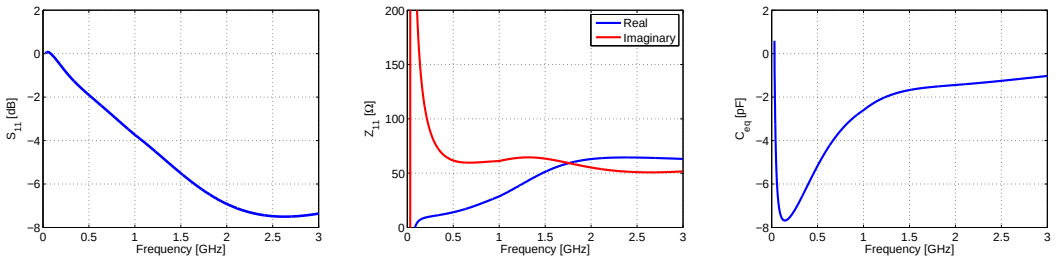

(a) (b) (c)

Figure 2.6: The regenerated results from [52]. (a) Input reflection coefficient magnitude in dB, (b) input impedance and (c) equivalent capacitance.

We targate at matching small antennas far from their inherent resonances. Under these conditions, the antenna will have a very high reactance. Hence, we started optimizing this circuit to obtain a very small capacitance (very high reactance) in the UHF band. The active component is changed to BFR93A [60] because it is better suited for higher frequencies (it has a transition frequency of $F_T = 6GHz$). The schematic of the initial designed circuit is given in Figure 2.7. A prototype of the circuit was realized and measured. It was noticed that the circuit measured parameters are different from the simulated ones as it can be seen in Figure 2.8.

The measured circuit has a resonance around $1.5GHz$ while the simulated one has a plat response.

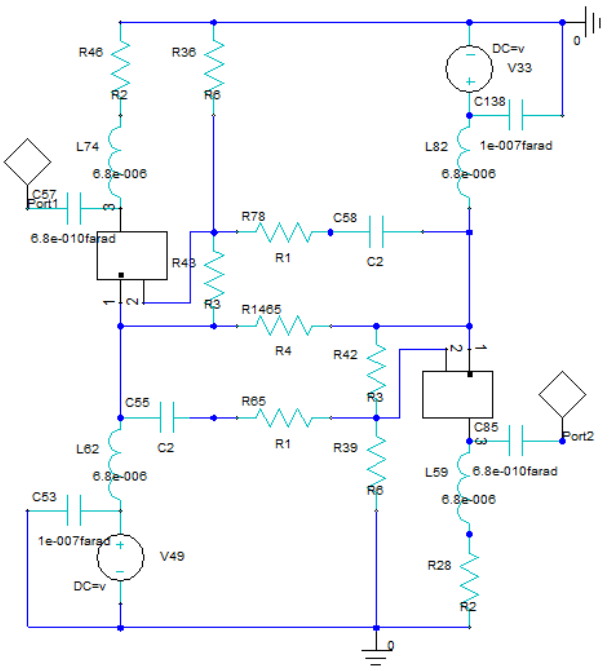

Figure 2.7: The initial simulated schematic of the designed circuit.

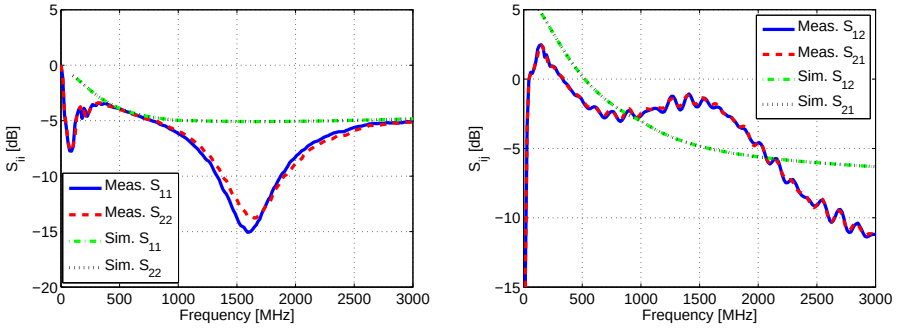

(a) (b)

Figure 2.8: The S parameters magnitude in dB of the initial circuit. (a) S_{ii} and (b) S_{ij}.

To further understand the circuit function, a more realistic model of the circuit was simulated. In this model, the parasitic elements of the transistor were taken into consideration. The ideal inductors were replaced with their realistic model taking into account their Q and self resonance frequency. Finally, transmission lines corresponding to the circuit board topology were included. These lines have a length of $L = 1.4mm$ a width of $W = 0.8mm$ and are printed on Rogers Duroid 5880. The final schematic is shown in Figure 2.9 and its simulated results are compared to the measured ones in Figure 2.10. As it can be seen, the simulated results are in a very good agreement with the measured ones. The difference at low frequencies (below $400MHz$) is probably due to the calibration limitation.

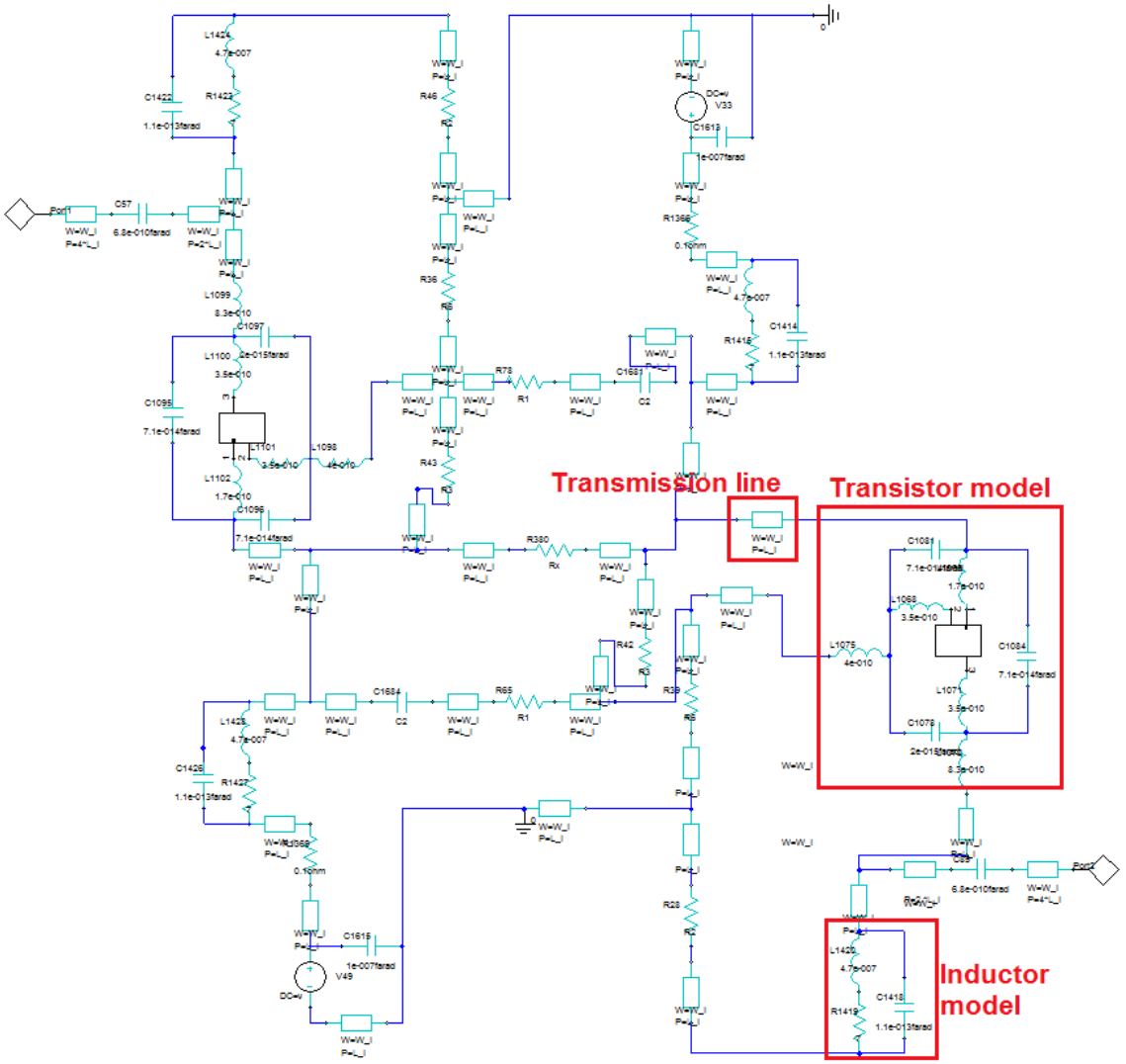

Figure 2.9: The final simulated schematic of the designed circuit.

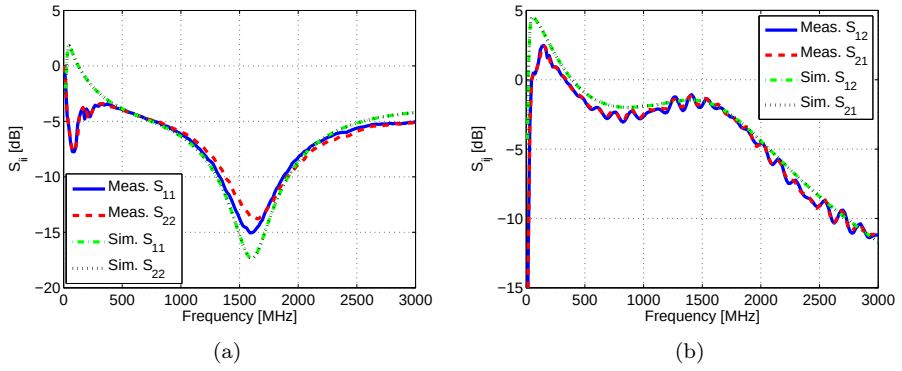

(a) (b)

Figure 2.10: The S parameters magnitude in dB of the final circuit. (a) S_{ii} and (b) S_{ij}.

2.4.2 Parametric Analysis

After having a good simulation model, a long optimization process (in terms of the circuit loss and stability) was started. A parametric analysis showed that the circuit losses can be reduced by reducing the value of R_1 (connecting between the collector of one transistor and the base of the other) as shown in Figure 2.11. It should be noticed that, as the circuit is symmetric, only S_{11} and S_{12} are shown. Changing the value of this resistance from 0Ω to 500Ω increases the circuit losses at $910MHz$ from $0.03dB$ to $3.98dB$. However, as it can be seen from the same figure reducing this value below 100Ω causes a high frequency oscillation (seen as $S_{11} > 0dB$) at $2.3GHz$, this trend was validated via measurements. This oscillation is due to the effect of the transmission lines in the feedback path and cannot be controlled. This high frequency oscillation will have inter-modulation products in the band of interest and cannot be tolerated. Accordingly the value of this resistance was chosen to be 100Ω.

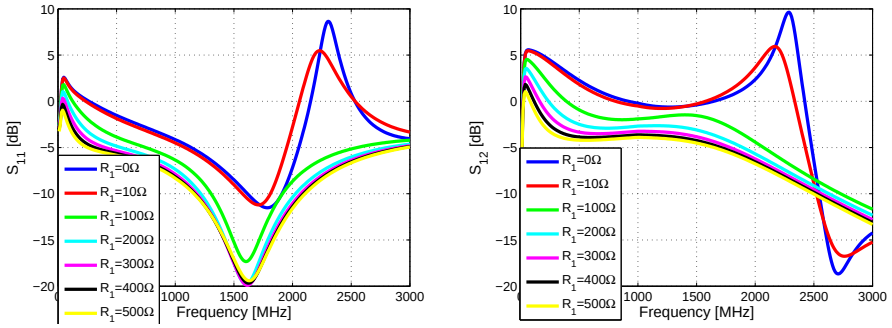

(a) (b)

Figure 2.11: The effect of the resistance R_1 on (a) S_{11} and (b) S_{12}.

Another possible solution is adding a capacitance in parallel with this resistance (R_1) to reduce its effect at high frequencies. As it can be seen from Figure 2.12, adding a capacitance of $6.8pF$ reduces the circuit losses from $1.95dB$ to $1.18dB$. However, this yields to near oscillation conditions at $2.2GHz$. In measurements, the circuit is not stable, hence, this option was also excluded.

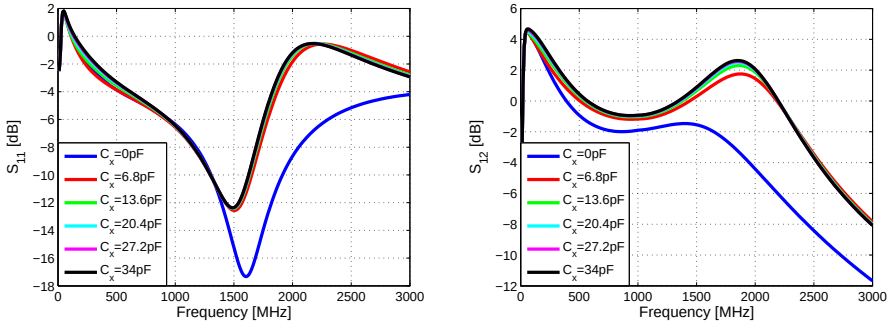

(a) (b)

Figure 2.12: The effect of connecting a capacitance C_x in parallel with the resistance R_1 on (a) S_{11} and (b) S_{12}.

Finally, we studied the effect of the collector current I_C on the circuit parameters, the DC voltage V_{DC} was varied from 0 to $10V$ with a step of $2.5V$. This is equivalent to collector currents of $(0, 2.25, 7.95, 13.95, 20.17)mA$ and V_{CE} voltages of $(0, 2.24, 4.08, 5.89, 7.67)V$. As it can be seen from Figure 2.13, starting from $2.5V_{DC}$ the two transistors are properly biased and the increasing the biasing current does not significantly affect the circuit performance.

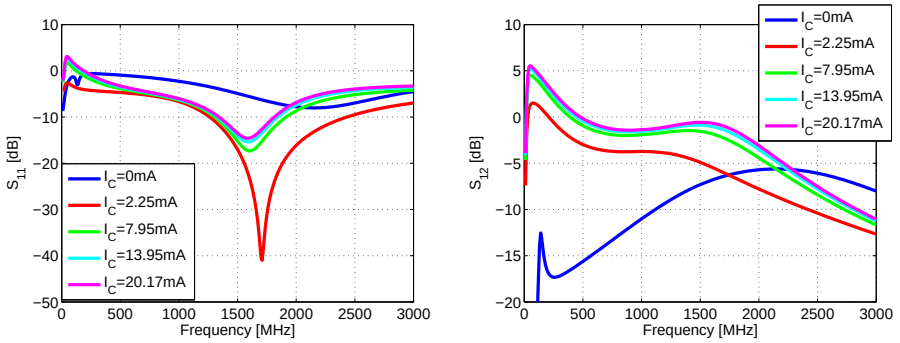

(a) (b)

Figure 2.13: The effect of biasing on (a) S_{11} and (b) S_{12}.

After this optimization process the circuit component values were fixed and the circuit stability (in simulation) was tested using the different stability criteria and the obtained results are given in Figure 2.14. As it can be noticed, B factor shows that the circuit is unconditionally stable ($B > 0$) starting from $690MHz$ while both K and μ show that the circuit unconditionally stable ($K \geq 1, |\Delta| < 1$ and $\mu \geq 1$) starting from $1.48GHz$.

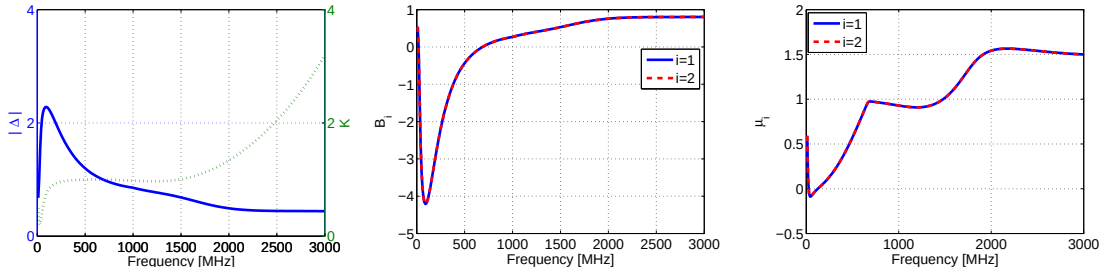

(a) (b) (c)

Figure 2.14: Calculated stability factors of two-port NIC in simulation. (a) Roulette factor, (b) B and (c) μ.

To further investigate the circuit stability we plotted the two ports stability circles in the unstable band at $110MHz$, $510MHz$ $910MHz$ and $1310MHz$. As a reminder, the input (load) circle center C_i and radius R_i are given by:

$$C_i = \frac{{S_{11}}^* - \Delta^* S_{22}}{|S_{11}|^2 - |\Delta|^2} \tag{2.9}$$

$$R_i = \left| \frac{S_{12}S_{21}}{|S_{11}|^2 - |\Delta|^2} \right| \tag{2.10}$$

Similarly for the output (source) circle center C_o and radius R_o are given by:

$$C_o = \frac{{S_{22}}^* - \Delta^* S_{11}}{|S_{22}|^2 - |\Delta|^2} \tag{2.11}$$

$$R_o = \left| \frac{S_{21} S_{12}}{|S_{22}|^2 - |\Delta|^2} \right| \tag{2.12}$$

The obtained results are given in Figure 2.15 where for the first case the Smith chart origin is in the unstable region while in the others it is in the stable one. These results show that as the frequency increases the stability region increases and starting from $500MHz$ almost all of the smith chart is stable.

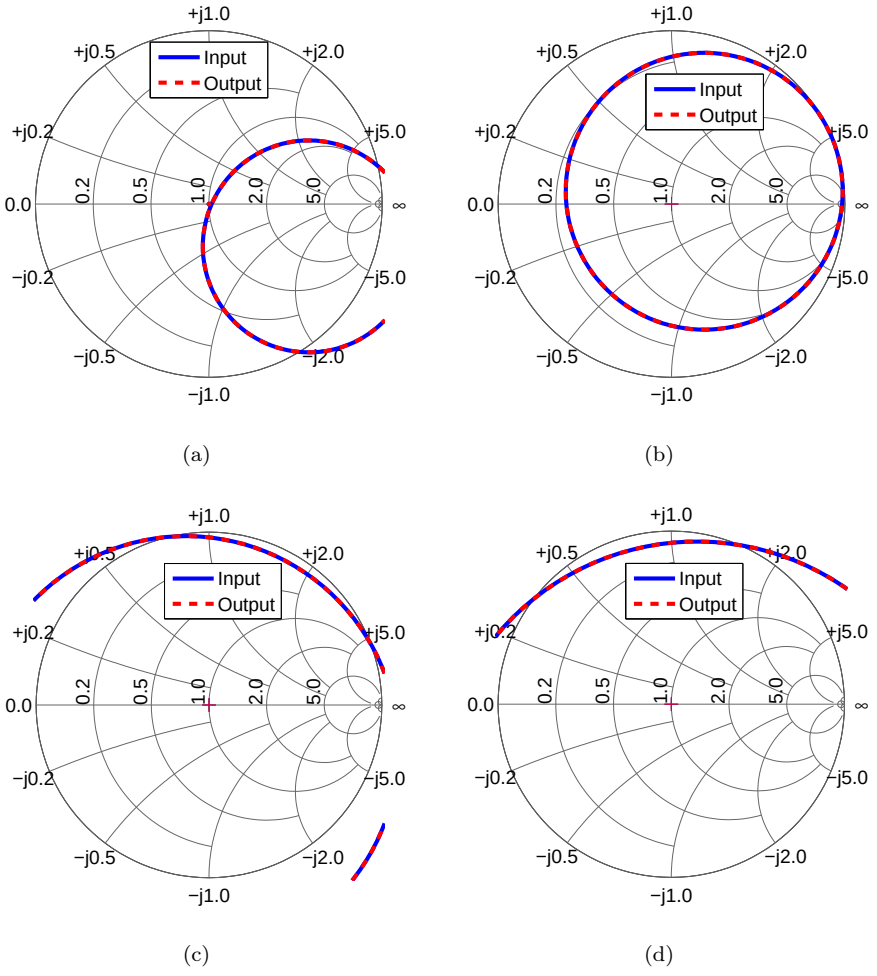

Figure 2.15: Two-ports NIC stability circles at (a) 0.11GHz, (b) 0.51GHz (c) 0.91GHz and (d) 1310MHz.

A prototype of the circuit was fabricated as shown in Figure 2.16(b). The circuit is supplied by 5 V_{DC}, it consumes a current of $16.5mA$ or equivalently a DC power of $82.5mW$. To have a stable circuit, the circuit overall impedance should be positive. Consequently, the circuit output is connected to a lumped network. Then, the circuit (alone) reactance can be de-embedded. The measured de-embedded reactance of this circuit is shown in Figure 2.17(a). As it can be noticed, the reactance decreases with frequency which means that the circuit has a non-Foster behavior (it acts as a

negative capacitance). The value of the equivalent capacitance can be calculated as follows:

$$C_{eq} = \frac{-1}{wX} \tag{2.13}$$

where $w = 2\pi f$ is the angular frequency and X is the measured reactance. The value of the equivalent capacitance is given in Figure 2.17(b).

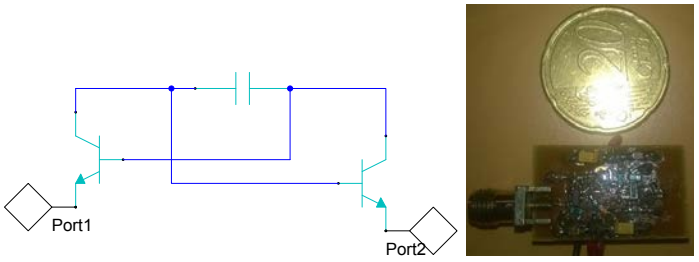

(a) (b)

Figure 2.16: Proposed NIC circuit. (a) General schematic of Linvill floating-type circuit and (b) a photograph of the prototype.

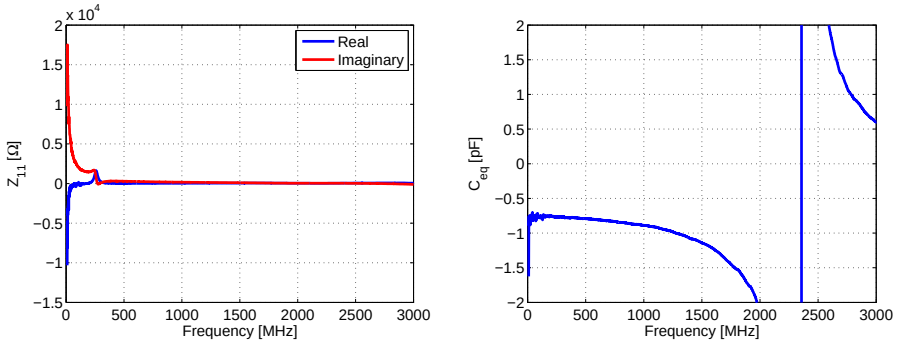

(a) (b)

Figure 2.17: Measured de-embedded parameters of NIC circuit. (a) De-embedded input impedance and (b) equivalent capacitance.

After verifying that the circuit is indeed of the type non-Foster, we shall now proceed with its characterization in terms of losses, stability and linearity.

2.4.3 Losses Analysis

A two-port version of the circuit was fabricated to measure the circuit losses. Figure 2.18(a) shows a photograph of the prototype and Figure 2.18(b) shows its measured S parameters. As it can be noticed, the circuit is not well matched for the whole band (the circuit should be matched when its terminated with the antenna). Taking into account the reflection (mismatch) losses given in Figure 2.18(c), the circuit internal losses (independent from the matching) are given in Figure 2.18(d). It can be noticed that the circuit has a positive gain of $7dB$ at $0.165GHz$, as the frequency increases, this gain decreases and starting from $1.06GHz$ the circuit becomes lossy.

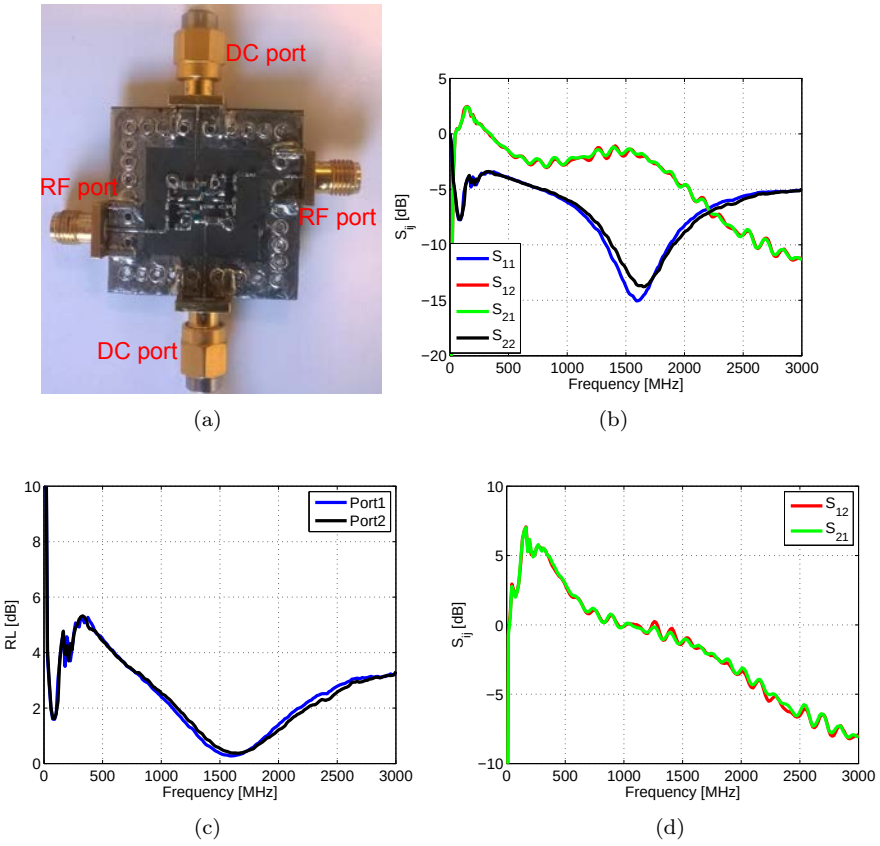

Figure 2.18: Measured parameters of two-port NIC. (a) Fabricated prototype, (b) S parameters, (c) losses due to the mismatch and (d) calculated gain.

2.4.4 Stability Analysis

The circuit S parameters were also used to study its stability using the different stability factors namely K, Δ, B and μ. The obtained results are given in Figure 2.19. B parameter shows that the circuit is unconditionally stable starting from $0.52GHz$ while both K and μ factors show that the circuit is unconditionally stable starting from $1.5GHz$.

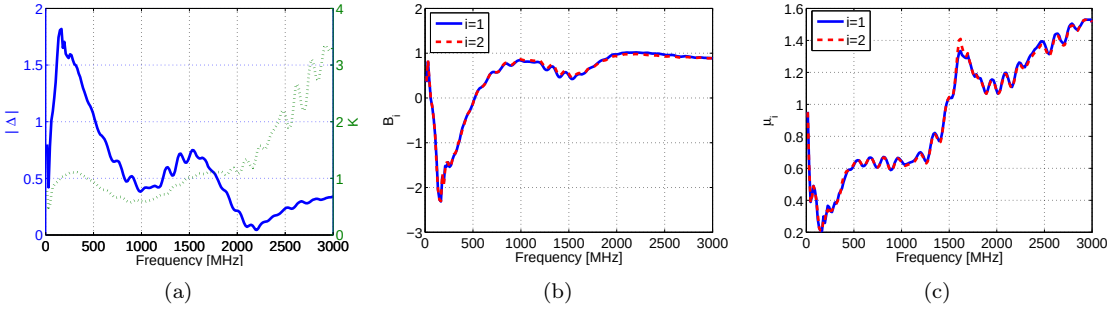

Figure 2.19: Calculated stability factors of two-port NIC. (a) Roulette factor, (b) B and (c) μ.

To investigate the stabilization possibilities of the circuit, its two ports stability circles were plotted in the unstable region at the following frequencies: $(0.11, 0.51, 0.91, 1.31)GHz$.

The obtained results are given in Figure 2.20 where for all cases the origin of the smith chart is in the stable region. As predicted by the results of μ factor, as the frequency increases, the stable region also increases.

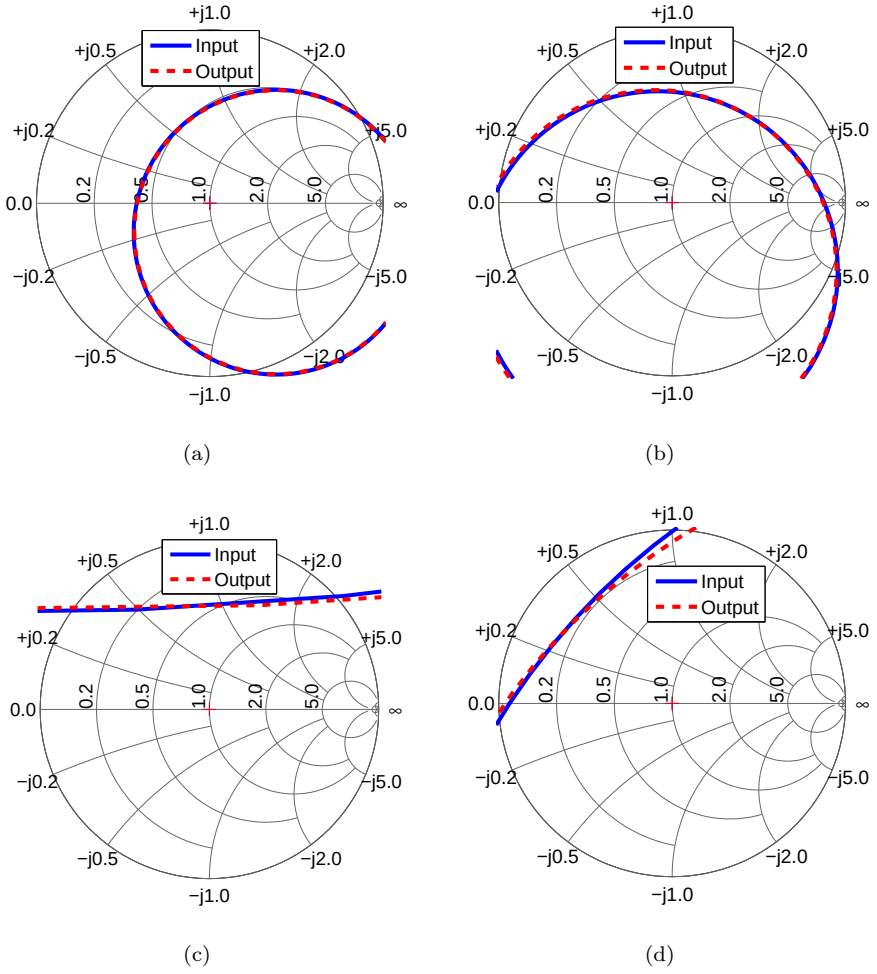

Figure 2.20: Two-ports NIC stability circles at (a) 0.11GHz, (b) 0.51GHz, (c) 0.91GHz and (d) 1.31GHz .

2.4.5 Gain Compression Analysis

Later, to evaluate the circuit linearity, it was tested for the gain compression at $910MHz$. The measurement set up and the obtained results are given in Figure 2.21. As it can be seen, the circuit has an output $1dB$ gain compression point at $7.8dBm$ and an output saturation point at $15.6dBm$. Since the circuit has a transducer gain of $-2.9dB$ at this frequency, the input $1dB$ gain compression point and saturation point are respectively $10.7dBm$ and $18.5dBm$. No values of these parameters for this type of circuits are given in the available literature for comparison.

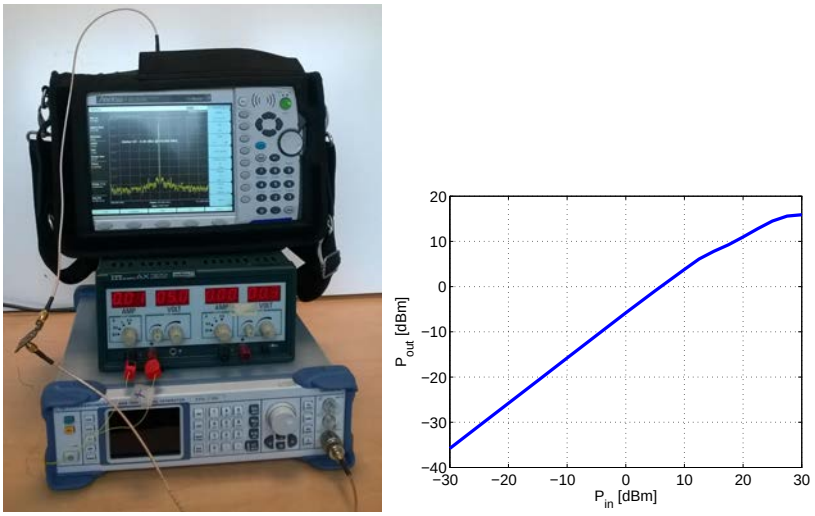

(a) (b)

Figure 2.21: The gain compression measurement. (a) Set up and (b) obtained results.

2.4.6 Inter-Modulation Analysis

Finally, the circuit was tested for two harmonics inter-modulation problems. The test set up is shown in Figure 2.22. Two signal generators are used to generate two tones at $910MHz$ and $920MHz$ with an equal power changing from $-20dBm$ to $0dBm$. The obtained results are given in Figure 2.23. The n^{th} order Output Intercept Point (OIP_n) can be calculated as follows:

$$OIP_n = P_{out} + \frac{\Delta P_n}{n-1} \tag{2.14}$$

where P_{out} is the main harmonic power and $\Delta P_n = P_{out} - P_n$ P_n being the n^{th} Harmonic power level. Accordingly, the first two OIPs are given by:

$$OIP_2 = P_{out} + \Delta P_2 \approx 30dBm \tag{2.15}$$

and

$$OIP_3 = P_{out} + \frac{\Delta P_3}{2} \approx 19dBm \tag{2.16}$$

Figure 2.22: The circuit inter-modulation measurement set up.

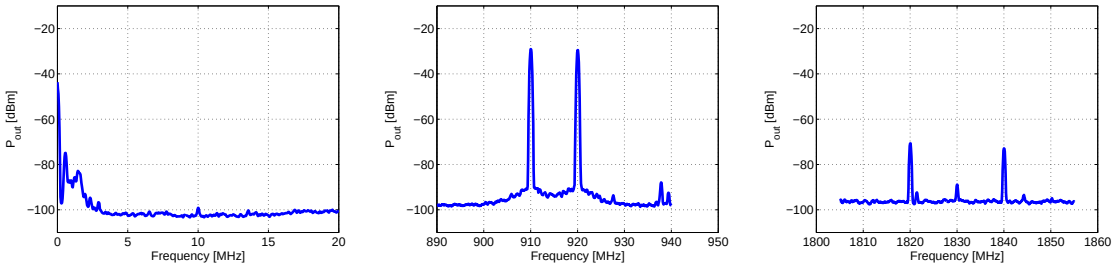

(a) (b) (c)

Figure 2.23: The circuit inter-modulation measurement results for $P_{in} = -20dBm$. (a) $w_a - w_b$, (b) $2w_a - w_b$ and (c) $3w_a - w_b$.

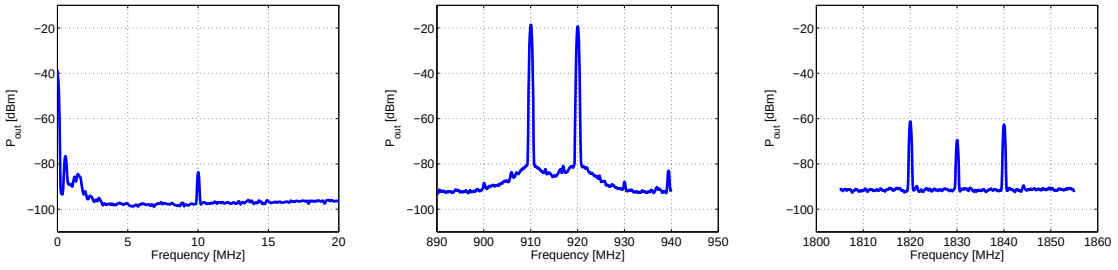

(a) (b) (c)

Figure 2.24: The circuit inter-modulation measurement results for $P_{in} = -10dBm$. (a) $w_a - w_b$, (b) $2w_a - w_b$ and (c) $3w_a - w_b$.

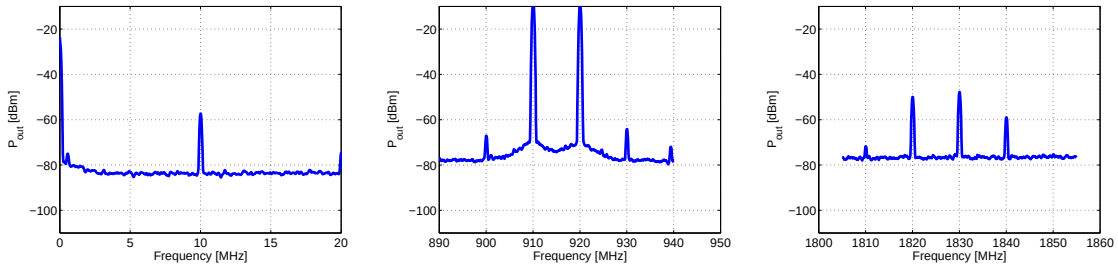

Figure 2.25: The circuit inter-modulation measurement results for $P_{in} = 0dBm$. (a) $w_a - w_b$, (b) $2w_a - w_b$ and (c) $3w_a - w_b$.

Then the n^{th} order Input Intercept Point (IIP_n) can be calculated from:

$$IIP_n = OIP_n - G \tag{2.17}$$

where G is the circuit gain. The circuit was also tested when the tones are at $910MHz$ and $911MHz$ revealing $OIP_2 \approx 28.2dBm$ and $OIP_3 \approx 17.7dBm$. These OIPs are in the average value of this type of circuits.

2.4.7 Noise Figure Measurement

Finally, the circuit Noise Figure (NF) is measured as shown in Figure 2.26(a). The noise level of the output of two stages of wide-band Low Noise Amplifiers [61] terminated at the input with a matched load P_{LNA} is registered, to be sure that the noise level is above the analyzer noise. Then, the circuit is connected between the output of the LNA and the spectrum analyzer and the corresponding noise level $P_{circuit+LNA}$ is registered. The circuit gain $G_{circuit}$ is also measured. Consequently, the circuit NF can be approximately estimated as follows:

$$NF = P_{circuit+LNA} - P_{LNA} - G_{circuit} \tag{2.18}$$

It should be noticed that the measurement is done with an $RBW = 1KHz, VBW = 0.3KHz$ and with no attenuation in the spectrum analyzer. The averaged obtained results given in Figure 2.26(b) shows that the circuit has a very low NF in the UHF band, this value around $910MHz$ is about $0.4dB$.

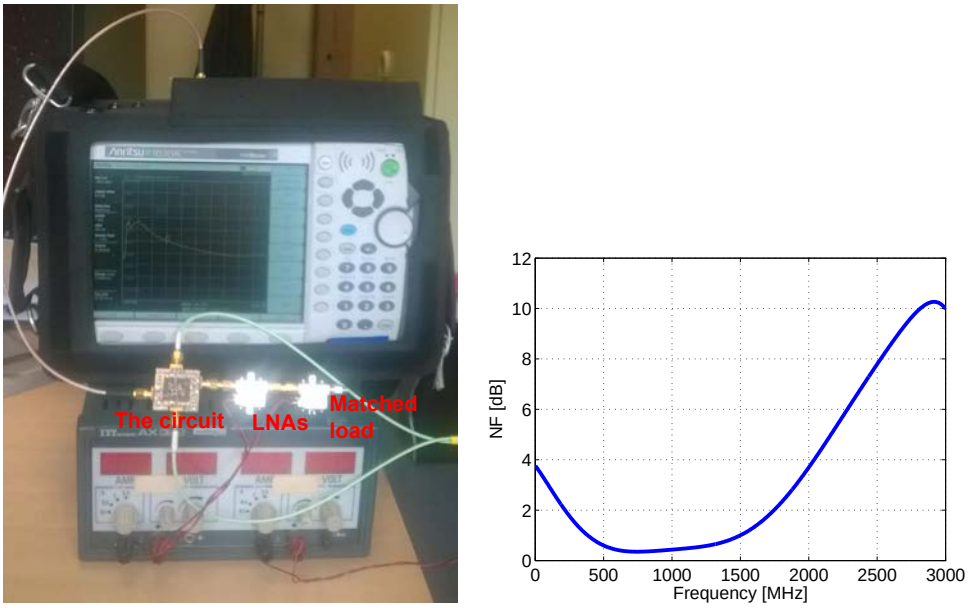

(a) (b)

Figure 2.26: The circuit NF measurement. (a) The set up and (b) the obtained value in dB.

After verifying the good functionality of the circuit (in terms of losses, stability, linearity, inter-modulation and noise), in the next section it will be used to match different small ILAs.

2.5 NIC-Matched ILA on a PCB

2.5.1 Antenna Structure

The first proposed antenna is an ILA of 9.5×19.5 mm^2 integrated on a Printed Circuit Board (PCB) of 100×60 mm^2 as shown in Figure 2.27(a). This antenna, printed on a 0.8mm-thick Rogers Duroid 5880 substrate, has a measured resonance frequency of 2.39 GHz (2.27(b)). The antenna measured input impedance after an appropriate rotation for eliminating the SMA effect is given in Figure 2.27(c). As it can be noticed, till $2.4GHz$ the antenna reactance is negative and it increases with the frequency. Hence, the antenna can be modeled as a resistance in series with a capacitance (this is the general case for dipole- monopole type antennas). To eliminate the antenna reactance around 910 MHz, a negative capacitor of 0.87 pF, $0.78pF$ in simulation, is required (Figure 2.27(d)). It can also be noticed that the changes in the required capacitance value is rather small in UHF band.

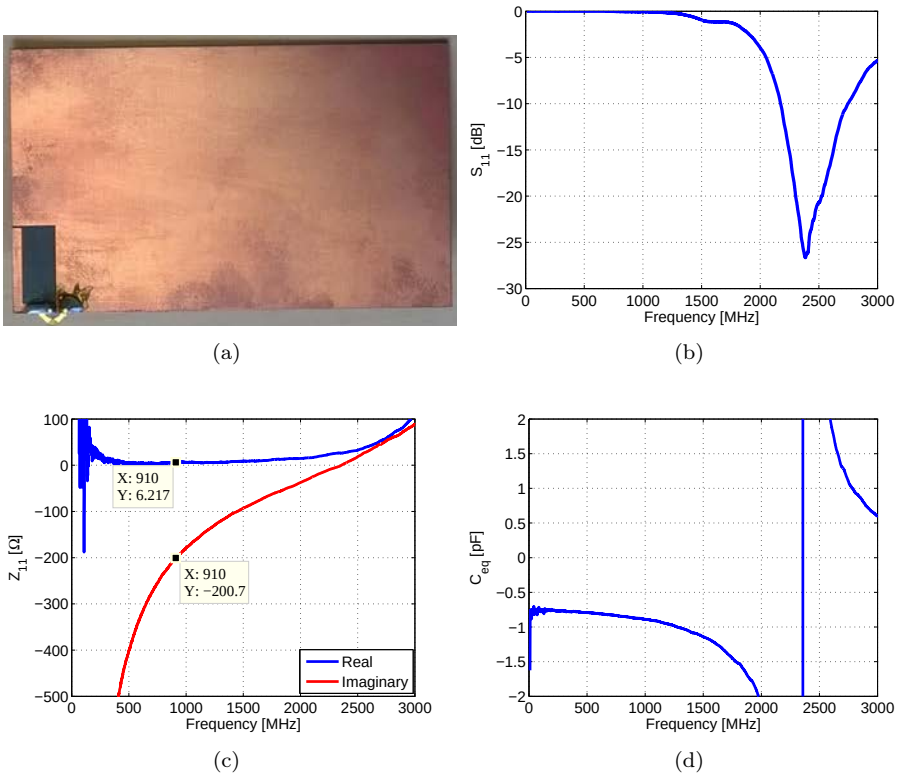

Figure 2.27: Passive ILA measured results. (a) Realized prototype, (b) input reflection coefficient magnitude in dB, (c) input impedance and (d) required negative capacitor.

2.5.2 Active Antenna Performance

2.5.2.1 Matching Performance

A prototype of the antenna with the integrated non-Foster circuit was realized and measured. Figure 2.28 shows a photograph of the active antenna with the NIC circuit on the bottom side. Figure 2.29(a) shows the antenna measured input reflection coefficient magnitude in dB. It can be noticed that the antenna has a $S_{11} < -10dB$ impedance bandwidth of 91% (matched throughout $(0.85-2.28)GHz$ frequency band). The antenna input impedance is given in Figure 2.29(b). Using this impedance, the antenna Q is calculated using (2.19) and compared to McLean limit on antenna Q in Figure 2.29(c) [6]. As it can be seen, in contrary to the passive (standalone) antenna, the active (non-Foster) antenna Q is lower than McLean limit almost for the entire observed band.

$$Q = \left| \frac{imag(Z)}{real(Z)} \right| \tag{2.19}$$

(a) (b)

Figure 2.28: A photograph of the fabricated active antenna. (a) Top view and (b) bottom view.

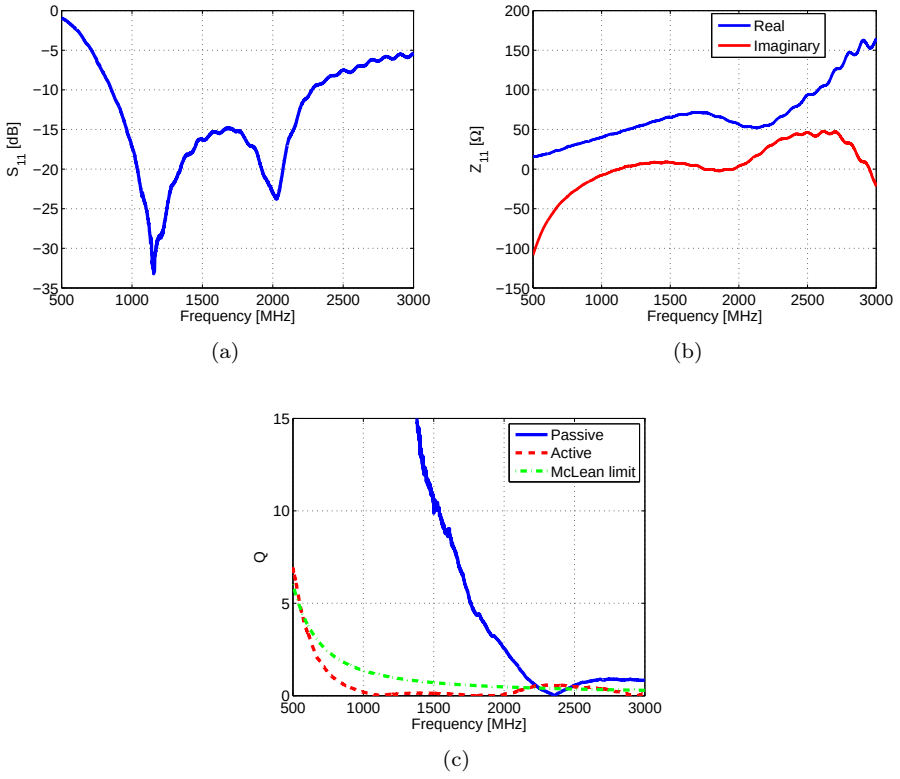

(a) (b) (c)

Figure 2.29: Active antenna measured parameters. (a) Fabricated prototype, (b) input reflection coefficient magnitude in dB, (c) input impedance and (d) Q.

2.5.2.2 Stability, Noise and Linearity Performance

The antenna stability has been underlined using a spectrum analyzer (DSA1030 [62]) with a Power Spectral Density (PSD) of $-134dBm/Hz$. Figure 2.30 shows the power of the different harmonics measured by the spectrum analyzer when connected to the antenna in anechoic environment. It can be noticed that no visible additive noise affects the bandwidth of interest (around $910MHz$). To investigate the added noise by the non-Foster circuit, we compare the output of the spectrum analyzer when connected to the non-Foster antenna and when connected to a 50Ω load. The measurement conditions are the same as before, however, the results are averaged on 10 cycles for fair comparison. The obtained results given in Figure 2.31 show

that no visible noise is added by the non-Foster.

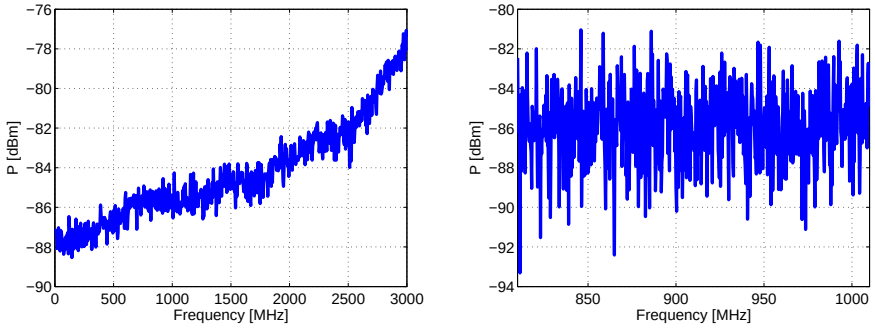

(a) (b)

Figure 2.30: The noise floor level of the spectrum analyzer terminated at the input with the non-Foster matched antenna. (a) On $(0.01 - 3)GHz$ frequency band and (b) on $(0.81 - 1.01)GHz$ frequency band.

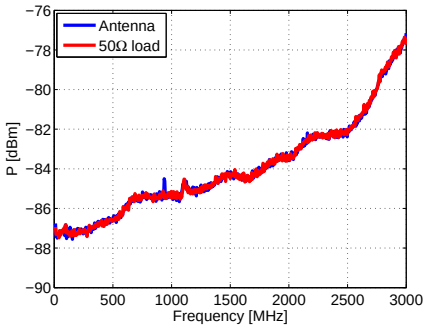

Figure 2.31: A comparison between the noise floor levels of the spectrum analyzer terminated at the input with a matched load and non-Foster matched antenna.

2.5.2.3 Radiation Performance

Both passive and active antennas far-field properties were measured in SATIMO SG 32 near-field measuring system. Figure 2.32(a) shows antennas' measured realized gains. As it can be noted, and as could be predicted from the two-port circuit measured S parameters, the active antenna is reciprocal (has a similar performance in both transmission and reception). This performance is better than the passive antenna till around $2GHz$. Around the band of interest, the active antenna has a realized gain of $-7dBi$. This gain increases upto $1dBi$ around $2Ghz$ where it starts decreasing again due to the circuit losses. Figure 2.32(b) shows the antennas' measured total efficiency. As it can be noticed, the active antenna has a total efficiency of 10% around the band of interest. Finally, to simplify the comparison, the realized gain- and the efficiency- improvement are given in Figure 2.33. As it can be noticed, at the band of interest, the antenna presents a gain improvement of $7dB$ and n efficiency improvement by a factor of 5.6.

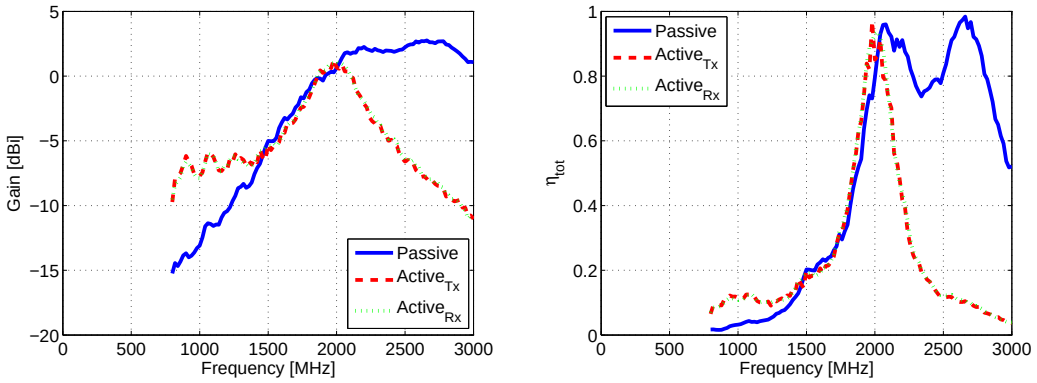

(a) (b)

Figure 2.32: The antenna far-field performance. (a) Realized gain and (b) total efficiency.

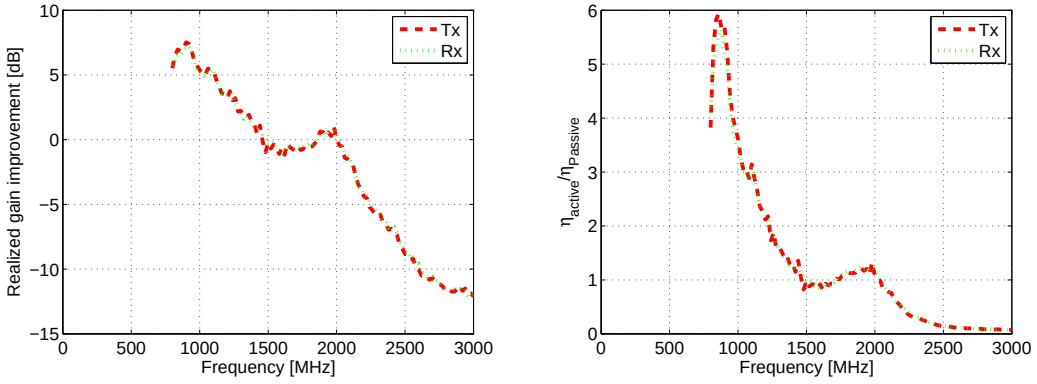

(a) (b)

Figure 2.33: The active/ passive antenna far-field performance improvement. (a) realized gain and (b) total efficiency.

2.6 NIC-Matched ILA on Small PCB

2.6.1 Antenna Structure

This antenna is similar to the previous one. However, it is cropped to fit in a USB PCB board with total dimensions of $90 \times 35mm^2$ as shown in Figure 2.34(a). Since the cropped ground plane is far from the monopole, and hence, it has a small participation in the radiation, the antenna overall performance is not significantly altered as it can be seen from the antenna measured input reflection coefficient magnitude in dB given in Figure 2.34(b) and impedance given in Figure 2.34(c). The value of the required negative capacitor is given in Figure 2.34(d). As it can be seen a negative capacitor of $0.96pF$, $0.76pF$ in simulation, is required to match the antenna at $910MHz$.

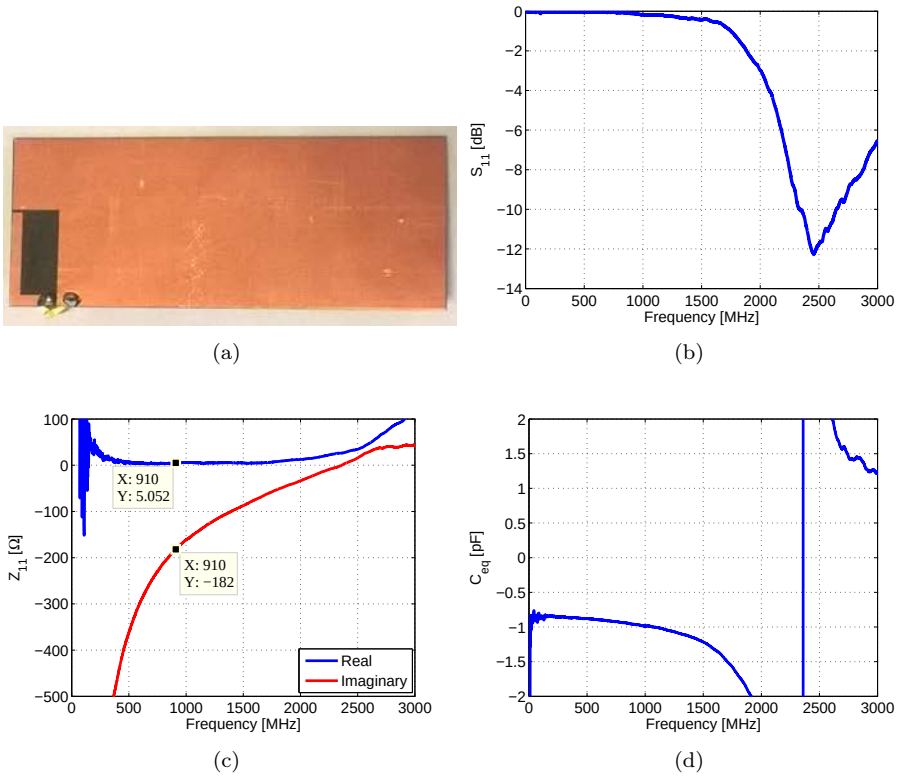

(a) (b) (c) (d)

Figure 2.34: Passive ILA on a small PCB measured results. (a) Realized prototype, (b) input reflection coefficient magnitude in dB, (c) input impedance and (d) required negative capacitor.

2.6.2 Active Antenna Performance

2.6.2.1 Matching Performance

A prototype of the antenna with the non-Foster circuit was realized and measured. Figure 2.35 shows a photograph of the active antenna and Figure 2.36(a) shows its measured input reflection coefficient magnitude in dB. It can be noticed that antenna has an impedance bandwidth of 92% (matched throughout $(0.86-2.33)GHz$ frequency band). The antenna input impedance is given in Figure 2.36(b) and its calculated Q given in Figure 2.36(c). It can be noticed, as in the case of the first antenna, the active antenna presents a Q lower than the limit given by McLean.

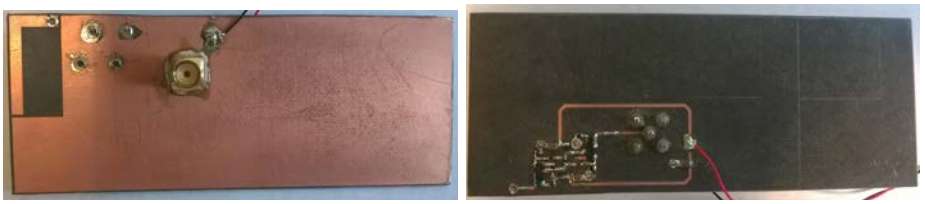

(a) (b)

Figure 2.35: A photograph of the fabricated active antenna on a small PCB. (a) Top view and (b) bottom view.

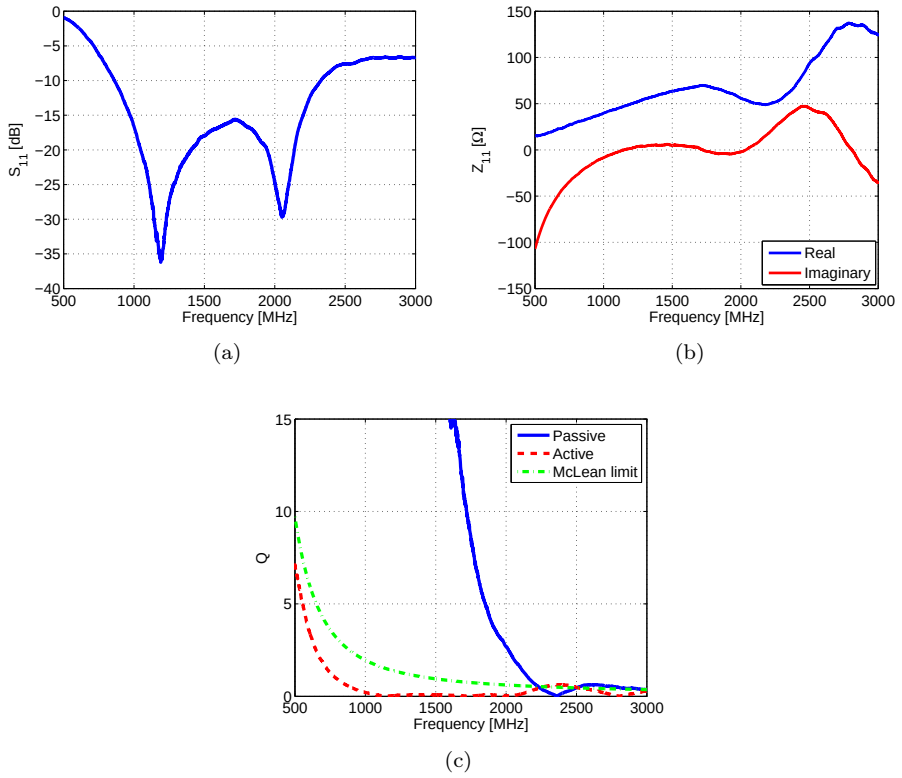

Figure 2.36: The measured parameters of the active antenna on a small PCB. (a) Input reflection coefficient magnitude in dB, (b) input impedance and (d) Q.

2.6.2.2 Stability and Noise Performance

As in the previous case, the antenna stability has been underlined using a spectrum analyzer. Figure 2.37 shows the noise floor of the spectrum analyzer when connected to the antenna. as it can be noticed the antenna is stable in the entire observed frequency band. As done previously, the output of the spectrum analyzer when connected to the non-Foster antenna and when connected to a 50Ω load are compared. The obtained results given in Figure 2.38 show that the added noise by the non-Foster circuit is negligible in the band of interest. The two small peaks at $100MHz$ and $1105MHz$ are residuals of FM and television (DSTV) bands.

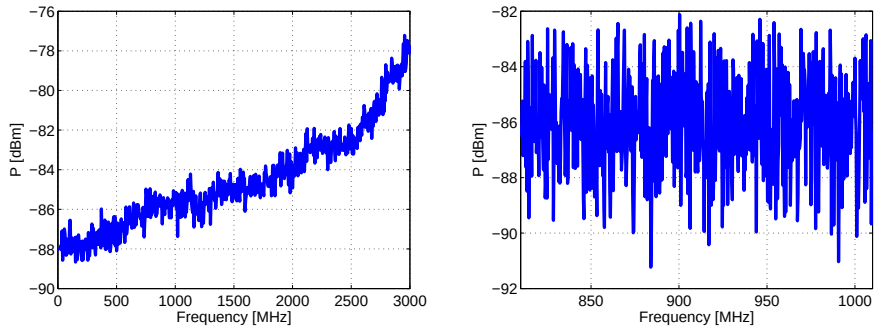

(a) (b)

Figure 2.37: The noise floor level of the spectrum analyzer terminated at the input with the non-Foster matched antenna on a small PCB. (a) On $(0.01 - 3)GHz$ frequency band and (b) on $(0.81 - 1.01)GHz$ frequency band.

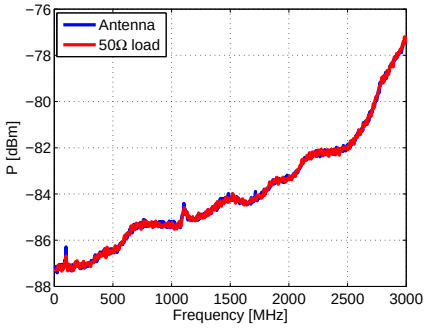

Figure 2.38: A comparison between the noise floor levels of the spectrum analyzer terminated at the input with a matched load and non-Foster matched antenna on a small PCB.

2.6.2.3 Radiation Performance

As in the previous case, both passive and active antennas far-field properties were measured in SATIMO SG 32 near-field measuring system. Figure 2.39(a) shows antennas' measured gains. As it can be noted, also this active antenna is reciprocal and it has a performance better than the passive one till around $2GHz$. Around the band of interest the active antenna has a measured gain of $-6dBi$. Figure 2.39(b) shows the antennas' total efficiency. As it can be noticed around the band of interest, the active antenna has an efficiency 9%. This efficiency increases upto 90% around $2GHz$ when it starts decreasing again due to the circuit losses. The same remarks can be made concerning the antenna realized gain- and the total efficiency-improvement compared to the passive antenna given in Figure 2.40.

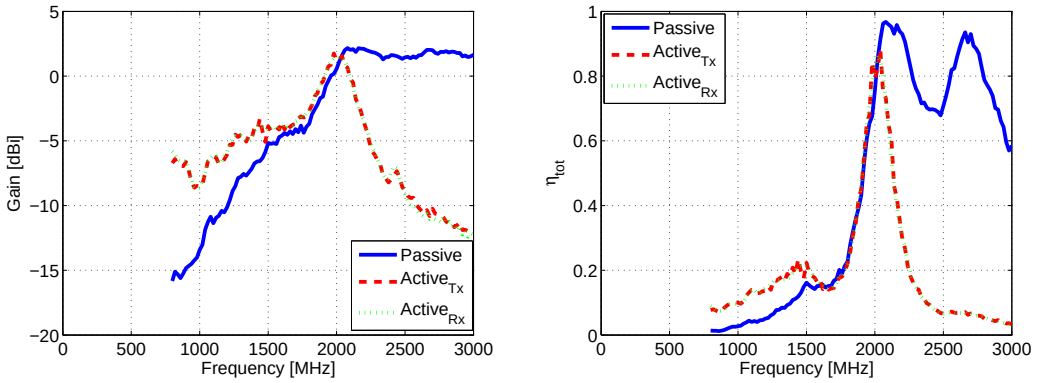

(a) (b)

Figure 2.39: The antenna on a small PCB far-field performance. (a) realized gain and (b) total efficiency.

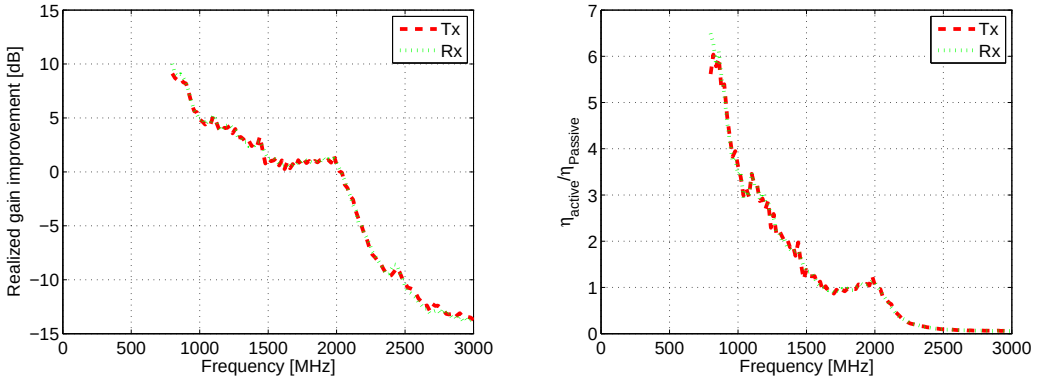

(a) (b)

Figure 2.40: The active/passive antenna on a small PCB far-field performance improvement. (a) Realized gain and (b) total efficiency.

2.7 Conclusion

A negative capacitor based on Linvill floating-type NIC was realized exploiting the parasitic capacitance of the transistors. The circuit had almost no losses in the band of interest. The circuit stability was studied using the different stability criteria namely K, μ and B. Furthermore, the stability circles demonstrated that a capacitive load is required to stabilize the circuit. Hence, a monopole type antenna that can be modeled as a capacitor in series with a small resistance (as Inverted-L Antenna (ILA)) was a suitable choice. The circuit acceptable linearity performance was underlined. Then, the circuit was used to match a miniature ILA in the $(0.76 - 2.17)GHz$ band. The antenna stability and low noise were underlined. The antenna demonstrated a significant improvement in its efficiency compared to the passive one. Later, the NIC was also used to match an ILA with the same dimensions as before but on a smaller PCB yielding a similar performance. The measured Q of both antennas is lower than Chu-McLean fundamental limit on antenna Q.

Chapter 3

Superdirective Antenna Arrays, Literature Review

3.1 Introduction

Antenna directivity is a very important parameter, and hence, it has been the subject of significant research. Early works focused on the upper limits of a single antenna- and antenna arrays- directivity [65]-[69]. Bowkamp and de Bruijn [64], Riblet [65], Hansen [66] and Uzkov [67] stated that any directivity can be attained for a given aperture. R.F. Harrington showed that, in a single antenna permitting a highest mode order of N, the directivity can attain N^2+2N, described as normal directivity [8]. Harrington also provided a relationship between the antenna size and N as $N = ka$, where k is the wave number and a is the radius of the sphere enclosing the entire antenna structure. I. Uzkov demonstrated that for a zero-spaced N isotropic radiators the maximum directivity is given by:

$$D = \sum_{n=1}^{N-1}(2n+1)[P_n(cos(\theta))]^2 \tag{3.1}$$

where P_n is n order Legendre polynomial. Since the maximum directivity is in the end-fire direction (for $\theta = 0$), this directivity is given by:

$$D = \sum_{n=1}^{N-1}(2n+1)[P_n(1)]^2 \tag{3.2}$$

and since $P_n(1) = 1, \forall n > 0$, the directivity is given by:

$$D = \sum_{n=1}^{N-1}(2n+1) = N^2 \tag{3.3}$$

The same limit was derived by E. N. Gilbert and S. P. Morgan in [69] and was validated by C.O. Stearns [70] and C.T. Tai [71]. Bloch et al. showed that in a 0.2λ spaced four-element dipole array a directivity enhancement of $10.1dB$ can be achieved compared with the unit-element [76]. Due to some losses in the feeder and the dipoles themselves, the authors measured an enhancement of $8.7dB$ as in Figure 3.1.

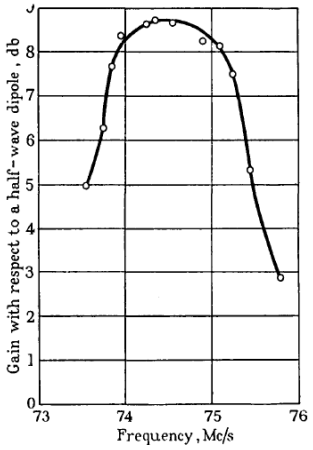

Figure 3.1: The directivity improvement of a four 0.2λ spaced dipoles array as presented by Bloch [76].

A superdirective antenna is one whose directivity is much greater than a reference antenna of the same size [77]. Superdirective arrays are achieved by decreasing the inter-element spacing. An interesting chapter summarizing early works on superdirective arrays is presented in [78].

3.2 Optimization Methods

Multiple design methods can be used to obtain superdirective arrays. Some of the most known ones are Hassen-Woodyard [79], Schelkunoff [80] and Dolph-Chebyshev [81]. In an N-element linear array along z-axis as with uniform amplitude and spacing (d) as in Figure 3.2, the array factor (AF) is give by:

$$AF = \sum_{n=1}^{N} e^{j(n-1)\psi} \tag{3.4}$$

where $\psi = kd\ cos\theta + \beta$ and $k = \frac{w}{c} = \frac{2\pi}{\lambda}$ is the wave number.

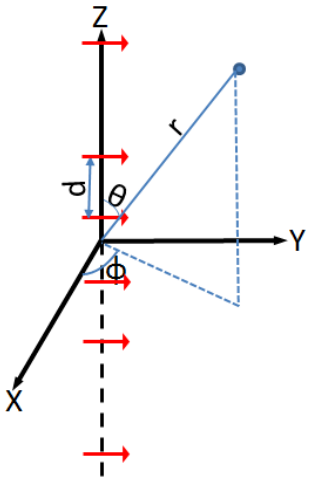

Figure 3.2: The geometry of N-element array along Z-axis.

If the reference point is the array center, this equation can be rewritten as:

$$AF = \frac{sin\left(\frac{N}{2}\psi\right)}{sin\left(\frac{1}{2}\psi\right)} \tag{3.5}$$

This array factor has a maximum value of N to normalize it to unity, it can be written as:

$$AF = \frac{1}{N}\left(\frac{sin\left(\frac{N}{2}\psi\right)}{sin\left(\frac{1}{2}\psi\right)}\right) \tag{3.6}$$

To point the main beam in the broadside direction ($\theta_0 = 90^o$), the required phase shift between the elements should be zero and all the elements should have the same excitation magnitude, i.e:

$$\psi = kd\ cos\theta|_{\theta=90^o} + \beta = 0 \Rightarrow \beta = 0 \tag{3.7}$$

The inter-element distance can be of any value. As the inter-element increases the obtained directivity also increases till around $d = 0.8\lambda$ (it depends on the number of the elements) when it starts decreasing. However, starting from $d = \lambda$ local maxima (grating lobes) appear. Figure 3.3 shows different parameters of 10-element,0.25λ-spaced ordinary broadside array. As it can be noticed, the maximum linear (dimensionless) directivity in the broadside direction is around 5.2.

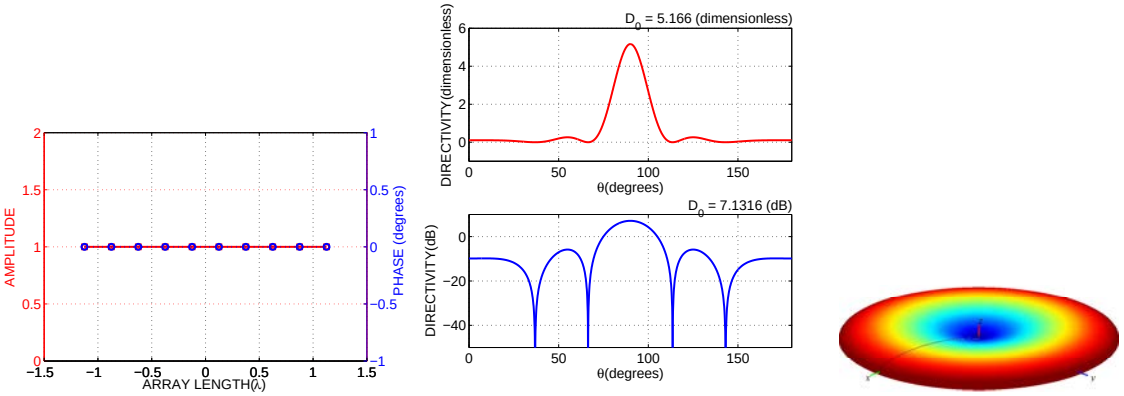

(a) (b) (c)

Figure 3.3: The different parameters of 10-element, 0.25λ-spaced uniform broadside array. (a) Excitation coefficients, (b) 2D total directivity radiation pattern and (c) 3D total directivity radiation pattern.

The required phase shift between elements for directing the main beam in the end-fire direction ($\theta_0 = 0^o \text{or} 180^o$) is given by:

$$\begin{aligned} &\psi = kd\ cos\theta|_{\theta=0^o} + \beta = 0 \Rightarrow \beta = -kd \quad \text{for maximum in} \quad \theta_0 = 0^o \\ &\psi = kd\ cos\theta|_{\theta=180^o} + \beta = 0 \Rightarrow \beta = kd \quad \text{for maximum in} \quad \theta_0 = 180^o \end{aligned} \tag{3.8}$$

This leads to a linear directivity of:

$$D_0 \approx 4N\left(\frac{d}{\lambda}\right) \tag{3.9}$$

Figure 3.4 shows different parameters of 10-element,0.25λ-spaced ordinary end-fire array. As it can be noticed, the maximum linear directivity in the end-fire direction is around 10.

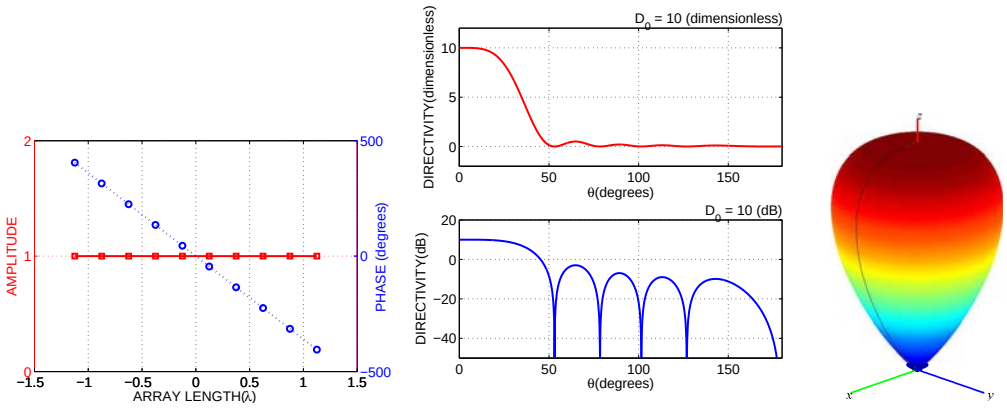

(a) (b) (c)

Figure 3.4: The different parameters of 10-element, 0.25λ-spaced uniform end-fire array. (a) Excitation coefficients, (b) 2D total directivity radiation pattern and (c) 3D total directivity radiation pattern.

3.2.1 Hansen-Woodyard Method

To increase the directivity of a large end-fire array[1], Hansen and Woodyard proposed that the required phase shift between closely-spaced elements of a very long array should be:

$$\beta = -\left(kd + \frac{2.92}{N}\right) \; for \; maximum \; in \; \theta_0 = 0^o \tag{3.10}$$

$$\beta = +\left(kd + \frac{2.92}{N}\right) \; for \; maximum \; in \; \theta_0 = 180^o \tag{3.11}$$

This leads to a linear directivity of:

$$D_0 \approx 1.805 \left[4N\left(\frac{d}{\lambda}\right)\right] \tag{3.12}$$

which is 1.805 times the one of an ordinary end-fire array. For large uniform arrays these conditions only yield an improved directivity (compared to a classical end-fire array) if the inter-element distance is around $\lambda/4$. Figure 3.5 shows different parameters of 10-element,0.25λ-spaced Hansen-Woodyard end-fire array. As predicted, the maximum linear directivity in the end-fire direction is around 18 which is 1.8 times the one of the ordinary array.

[1]Hansen-Woodyard work was based on an infinitely long antenna with continuous distribution. Hence, it gives good results for very long closely spaced arrays.

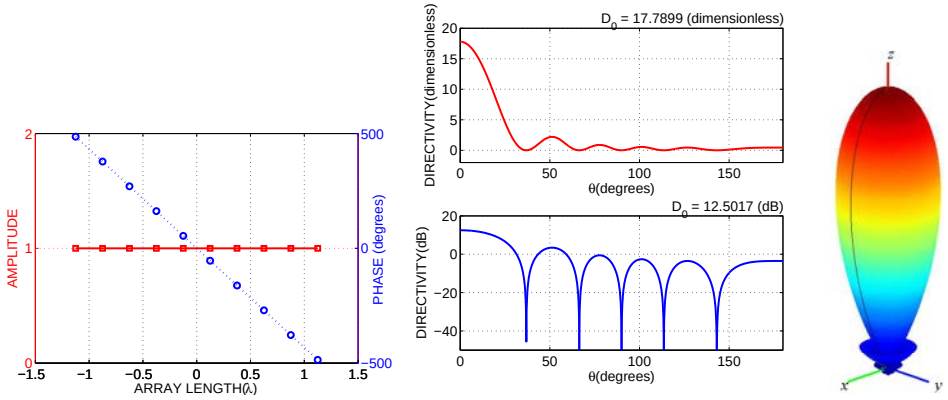

(a) (b) (c)

Figure 3.5: The different parameters of 10-element, 0.25λ-spaced Hansen-Woodyard end-fire array. (a) Excitation coefficients, (b) 2D total directivity radiation pattern and (c) 3D total directivity radiation pattern.

3.2.2 Dolph-Chebyshev Method

Dolph-Chebyshev array is a tradeoff between uniform and binomial arrays. The excitation coefficients of this array a_n are related to Chebyshev polynomials and it yields an array factor of:

$$AF(even) = \sum_{n=1}^{N} a_n cos[(2n-1)u] \tag{3.13}$$

$$AF(odd) = \sum_{n=1}^{N+1} a_n cos[2(n-1)u] \tag{3.14}$$

where $u = \frac{\pi d}{\lambda} cos\theta$. This array is based on a desired main-to-side lobe voltage ratio R_0. For large Dolph-Chebyshev arrays not very close to end-fire and with Side Lobe Levels (SLLs) between -20 and $-60dB$ a broadening factor f can be calculated as:

$$f = 1 + 0.636\left(\frac{2}{R_0} cosh[\sqrt{(cosh^{-}1R_0)^2 - \pi^2}]\right)^2 \tag{3.15}$$

Then the directivity is given by:

$$D_0 = \frac{2R_0^2}{1 + (R_0^2 - 1)f\frac{\lambda}{(L+d)}} \tag{3.16}$$

Figure 3.6 shows different parameters of 10-element,0.25λ-spaced Dolph-Chebyshev array for $R_0 = 15dB$. As it can be noticed, the maximum linear directivity in the broadside direction is around 5.3 which is slightly higher than the ones achieved with ordinary broadside array.

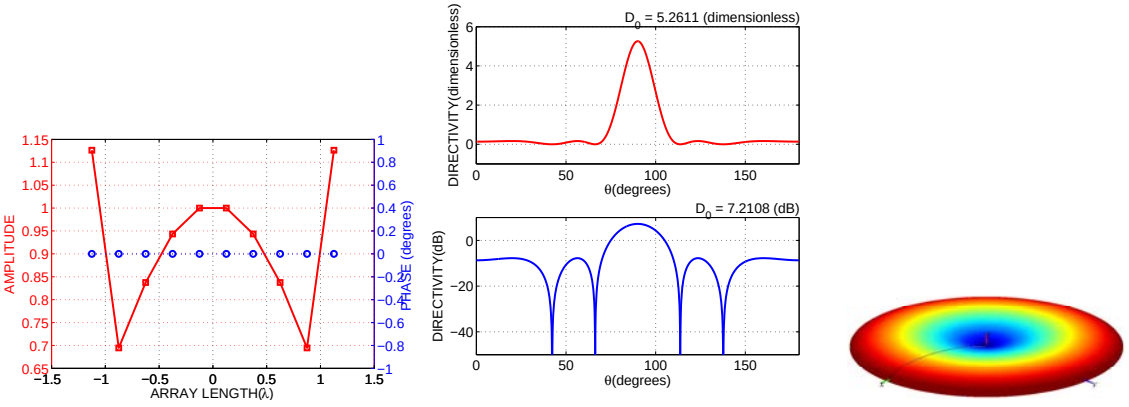

(a) (b) (c)

Figure 3.6: The different parameters of 10-element, 0.25λ-spaced Dolph-Chebyshev array for $R_0 = 20dB$. (a) Excitation coefficients, (b) 2D total directivity radiation pattern and (c) 3D total directivity radiation pattern.

It can be noticed, that in the three above-mentioned optimization methods the obtained directivity is proportional to its dimensions. This leads to a significant increment in the array dimensions for increasing its directivity.

3.2.3 Schelkunoff Method

Schelkunoff synthesis method permits designing arrays with nulls in specified directions. This method requires knowing the number of the nulls and their direction. The array factor of uniformly distributed elements with a spacing d, progressive phase β and non-uniform magnitude a_n can be written as:

$$AF = \sum_{n=1}^{N} a_n e^{j(n-1)(kd\ cos\theta+\beta)} = \sum_{n=1}^{N} a_n e^{j(n-1)\psi} \tag{3.17}$$

by taking a variable:

$$z = x + jy = e^{j\psi} = e^{j(kd\ cos\theta+\beta)} \tag{3.18}$$

the array factor can be rewritten as;

$$AF = \sum_{n=1}^{N} a_n z^{n-1} = a_1 + a_2 z + ... + a_n z^{N-1} \tag{3.19}$$

This polynomial of $(N-1)$ degree can be rewritten as:

$$AF = a_n(z - z_1)(z - z_2)...(z - z_{N-1}) \tag{3.20}$$

where $z_1, z_2, ...z_{N-1}$ are the roots of the polynomial. Then, the magnitude of the array factor can be written as:

$$|AF| = |a_n||z - z_1||z - z_2|...|z - z_{N-1}| \tag{3.21}$$

It should be noticed that all z lie on the unit circle. To clarify the design of this kind of arrays, let us take an example of an array with an inter-element distance

of $\lambda/8$ with nulls at $\theta_n = 0^o$, 90^o, 180^o. In this case the value of the roots can be calculated from:

$$z_n = e^{j\psi_n} = e^{j(kd\ cos\theta_n + \beta)} \tag{3.22}$$

Hence, this roots are: $0.7071 + j0.7071, 1, 0.7071 - j0.7071$. Then the equivalent polynomial can be calculated as follows:

$$AF = (z - z_1)(z - z_2)(z - z_3) = z^3 - 2.4142z^2 + 2.4142z - 1 \tag{3.23}$$

and the required excitation coefficients are $a_1 = -1$, $a_2 = 2.4142$, $a_3 = -2.4142$ and $a_4 = 1$. The normalized obtained array factor is given in Figure 3.7 and compared for different inter-element distances.

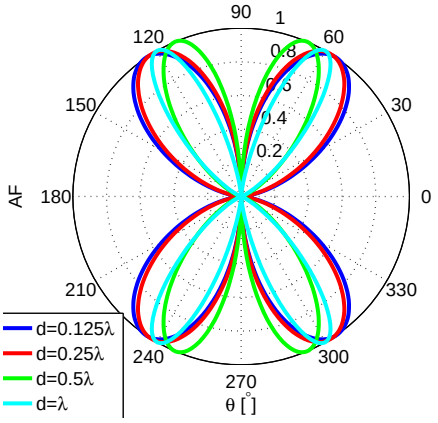

Figure 3.7: The normalized array factor of four-element Schelkunoff array with nulls at 0^o, 90^o and 180^o for different distances.

It should be noticed, that the higher the number of the elements the more control we have on radiation pattern. To illustrate this we took a Schelkunoff array with an inter-element distance of 0.125λ and nulls at 0^o, 90^o with a number of the elements of 3, 5, 7 or 9 (the same root is repeated multiple times) and plotted the normalized array factors in Figure 3.8. It can be noticed, as the number of the elements increases the beamwidth decreases. The achieved directivity is respectively $8.5dBi$, $11dBi$, $12.6dBi$ and $13.7dBi$.

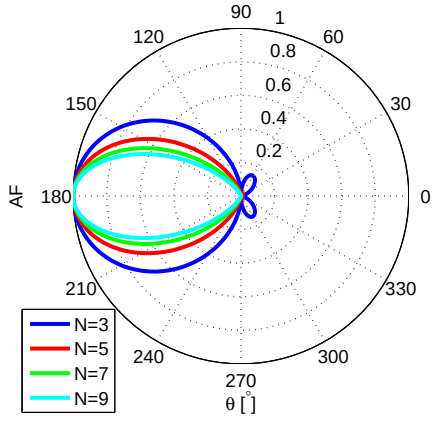

Figure 3.8: The normalized array factor of Schelkunoff array for nulls at 0^o, 90^o, a distance of 0.125λ and different number of elements N.

3.2.4 Yaghjian Method

Let us consider an array of N antennas located at positions r_n, $n = 1, 2, ..., N$ with respect to a fixed rectangular (xyz) coordinate system. The complex far-field radiated by the array in (θ, ϕ) is given by:

$$f(\theta, \phi) = \sum_{n=1}^{N} A_n f_n(\theta, \phi) e^{jk\hat{r}r_n} \tag{3.24}$$

where A_n are the complex excitation coefficients, $f_n(\theta, \phi)$ are the complex radiated far-fields and $\hat{r}$ is the unit vector in the far field direction (θ, ϕ). The array directivity is given by:

$$D(\theta, \phi) = \frac{|f(\theta, \phi)|^2}{\frac{1}{4\pi} \int_0^{2\pi} \int_0^{\pi} |f(\theta, \phi)|^2 sin(\theta) d\theta d\phi} \tag{3.25}$$

The current excitation coefficients that maximizes the directivity in the direction (θ_0, ϕ_0) are given by [82]:

$$a_{0n} = [H^*_{mn}]^{-1} e^{-jk\hat{r_0}r_m} f^*_m(\theta_0, \phi_0) f_n(\theta_0, \phi_0) \tag{3.26}$$

where $\hat{r_0}$ is the unit vector in the far field direction (θ_0, ϕ_0), and H_{mn} is given by:

$$H_{mn} = \frac{1}{4\pi} \int_0^{2\pi} \int_0^{\pi} f_m(\theta, \phi) f^*_n(\theta, \phi) e^{jk\hat{r}(r_m - r_n)} sin(\theta)\, d\theta\, d\phi \tag{3.27}$$

Now let us consider an array of N isotropic radiators equally-spaced by a distance d along the z axis with the first element located in the coordinate system origin. The calculated excitation coefficients of two, three and four-element arrays are given in Figure 3.9, Figure 3.10 and Figure 3.11. This excitation coefficients reveal that, for an array of fixed number of elements and for small distances, high excitation magnitudes are required and as the distance increases the excitation magnitude decreases. For $d = 0.5\lambda$ all the excitation magnitudes are equal.

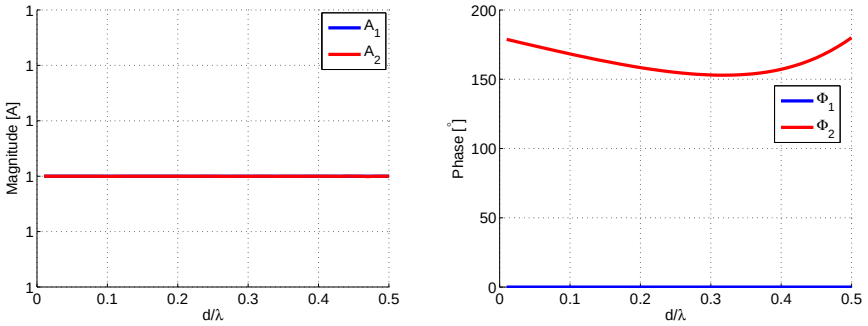

(a) (b)

Figure 3.9: Two d-spaced isotropic array optimal excitation coefficients. (a) Magnitude and (b) phase.

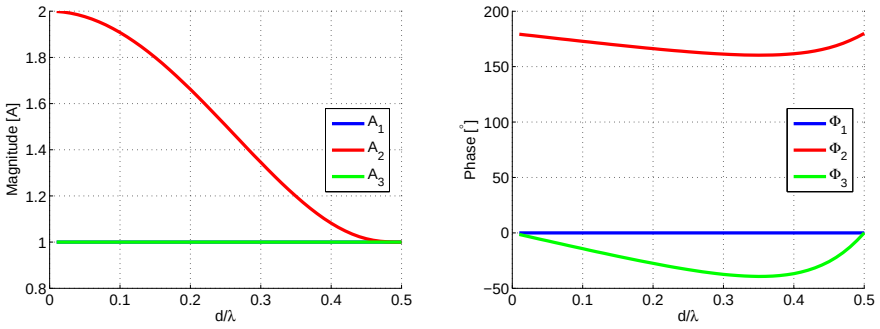

(a) (b)

Figure 3.10: Three d-spaced isotropic array optimal excitation coefficients. (a) Magnitude and (b) phase.

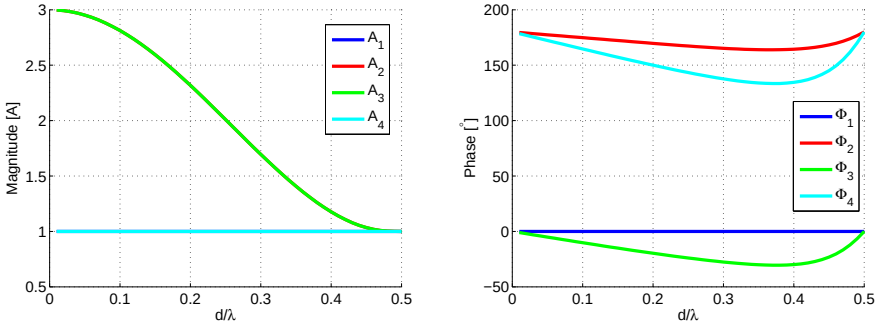

(a) (b)

Figure 3.11: Four d-spaced isotropic array optimal excitation coefficients. (a) Magnitude and (b) phase.

By applying these excitation coefficients, the maximum directivity that can be obtained as a function of the inter-element distance is given in Figure 3.12(a). It may be noted that when the distance between the elements approaches zero the array directivity approaches N^2. Increasing the spacing decreases the directivity in the main direction and increases it the backward direction (Figure 3.12(b)). At 0.5λ the directivity in both end-fire directions are equal to N (refer to Figure 3.12(c)).

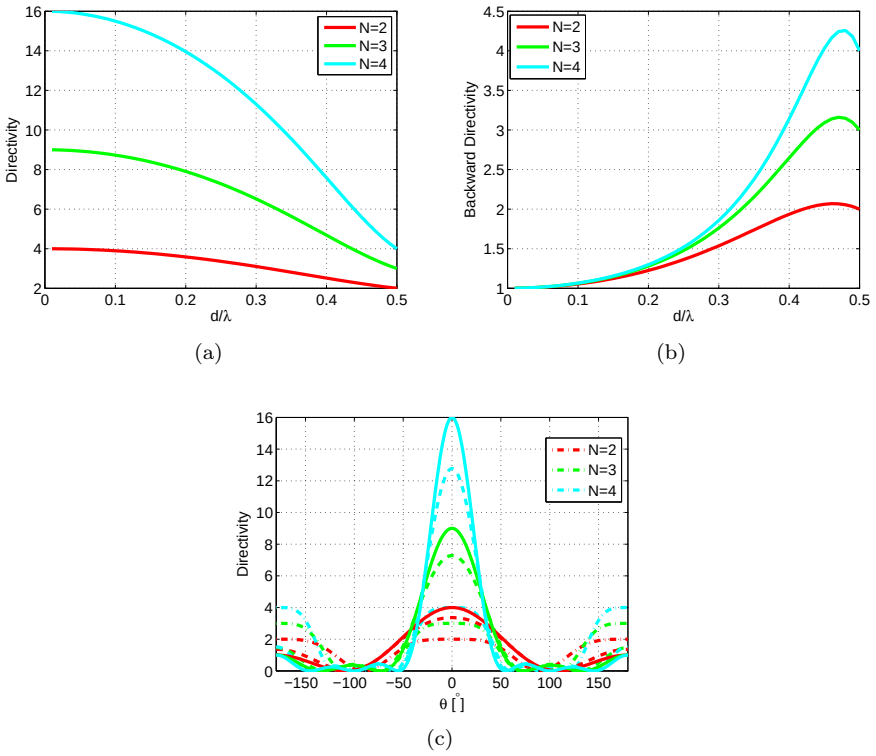

Figure 3.12: The performance of N-element d-spaced isotropic array. (a) The directivity in the main end-fire direction (b) the directivity in the backward en-fire direction and (c) the 2D total directivity radiation pattern for d=0.01 (continuous), d=0.25 (dashed) and d=0.5 (dashed-dotted).

The method was practically validated via the design of a three-element fully-driven monopole-based array. In agreement with the theory, the measured gain of the array increases with the decreasing spacing. However, according to the authors, for small inter-element distances ($d < 0.25\lambda$), the maximum gain cannot be achieved due to the ohmic losses as shown in Figure 3.13.

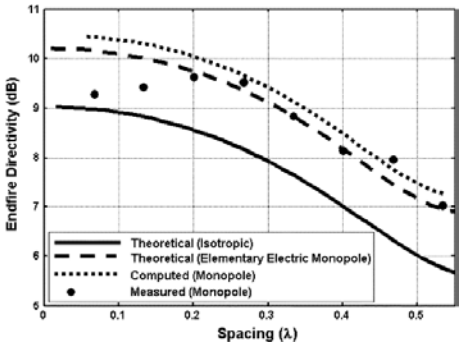

Figure 3.13: The directivity of three-element monopole array as presented by Yaghjian [82].

3.2.5 Spherical Wave Expansion Method

Recently a very interesting work on the design of superdirective antenna arrays based on spherical wave expansion was presented in [83]. The far-field $\overrightarrow{E}$ at a big distance ($kr \rightarrow \infty$) outside a sphere including all the sources is the linear combination of

far-field spherical wave pattern function $\overrightarrow{K}_{snm}$ [84], i.e:

$$\overrightarrow{E}(r,\theta,\phi) = \sqrt{\eta}\frac{k}{\sqrt{4\pi}}\frac{e^{jkr}}{kr}\sum_{s=1}^{2}\sum_{n=1}^{N}\sum_{m=-n}^{n} Q_{snm}\overrightarrow{K}_{snm}(\theta,\phi) \tag{3.28}$$

where Q_{snm} are the spherical wave coefficients. Then, the antenna directivity can be calculated from:

$$D(\theta,\phi) = \frac{\left|\sum_{snm} Q^{(3)}_{snm}\overrightarrow{K}_{snm}(\theta,\phi)\right|^2}{\sum_{snm}\left|Q^{(3)}_{snm}\right|^2} \tag{3.29}$$

where $Q^{(3)}_{snm}$ are the outgoing spherical wave coefficients. If all the spherical modes N can be weighted separately, the maximum directivity in a given direction $D(\theta_0,\phi_0)$ can be obtained if:

$$Q^{(3),max}_{snm} = c.\overrightarrow{K}^{*}_{smn}(\theta_0,\phi_0) \tag{3.30}$$

In the case of a P-element antenna array, the weighting is only possible on the excitation coefficients, and hence:

$$Q^{(3),max}_{snm} = c.\overrightarrow{K}^{*}_{smn}(\theta_0,\phi_0) = \sum_{p=1}^{P} a_p.Q^{(3)}_{smnp} \tag{3.31}$$

where a_p is the weight applied on each mode series and $Q^{(3)}_{smnp}$ are the spherical wave coefficients of element p. This method was validated via a full wave simulation of three- and five-element dipole-based arrays for $1.36GHz$ with a fixed dimension of $0.4\lambda_0 \times 0.25\lambda_0$. The two arrays presented respectively a maximum total directivity of $10.4dBi$ and $14.5dBi$. Figure 3.14 shows the arrays' geometries and the obtained results. As it can be noticed, both arrays achieve higher directivities than Harrington's limit and renormalized one [19].

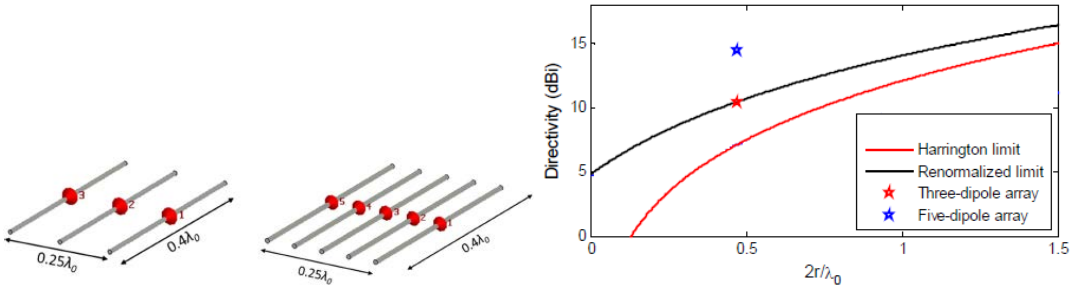

(a) (b)

Figure 3.14: The designed arrays in [83]. (a) Geometry and (b) the obtained total directivity.

This method was also used in [85] to design a parasitic superdirective four-element compact antenna array for $868MHz$. The array electrical size was $0.45\lambda_0 \times 0.36\lambda_0$ and it presented a maximum directivity of $11.7dBi$.

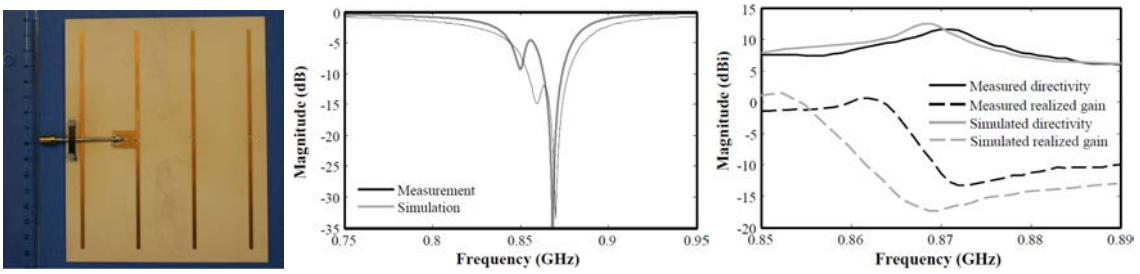

(a) (b) (c)

Figure 3.15: The proposed parasitic antenna in [85]. (a) The array geometry, (b) the input reflection coefficient magnitude in dB and (c) the end-fire total directivity and gain as a function of frequency.

Superdirectivity can also be achieved by using some beam forming techniques like the one proposed by Capon [86].

3.2.6 Capon Method

Let us assume a system of M sensor Uniform Linear Array (ULA). The n^{th} instantaneous received signal can be written as [87]:

$$\mathbf{X}(n) = [x_1(n), x_2(n), ..., x_M(n)]^T = \sum_{i=1}^{P} \mathbf{a}(\theta_i) s_i[n] + \mathbf{n}[n] \tag{3.32}$$

where $x_i(n)$ is the received data at i^{th} antenna, $[.]^T$ denotes the transpose, $s_i[n]$ is the i^{th} source, $\mathbf{n}[n]$ is a $M \times 1$ noise vector wit a power of σ^2 and

$$\mathbf{a}(\theta_i) = [1, e^{-jkd\ sin(\theta_i)}, ..., e^{-jkd(M-1)\ sin(\theta_i)}]^T \tag{3.33}$$

is a $M \times 1$ the steering vector of i^{th} signal in direction θ_i. Assuming that the incident signal and the noise are uncorrelated the covariance signal can be written as:

$$\mathbf{R}_{xx} = E[\mathbf{X}[n]\mathbf{X}[n]^H] = \sum_{i=1}^{P} \sigma_i^2 \mathbf{a}(\theta_i)\mathbf{a}(\theta_i)^H + \sigma_i^2 \mathbf{I} \tag{3.34}$$

where $E[.]$ denotes the expected value, $[.]^H$ is the Hermitian transpose, σ_i^2 is the i^{th} source power, and $\mathbf{I}$ is $M \times M$ identity matrix. In practice $\mathbf{R}_{xx}$ is replaced by the sample covariance matrix:

$$\widehat{\mathbf{R}}_{xx} = \frac{1}{N} \sum_{n=1}^{N} \mathbf{X}[n]\mathbf{X}[n]^H \tag{3.35}$$

where N is the number of snapshots. Assuming that the p^{th} signal is the Signal Of Interest (SOI), Capon beam-former is the solution of the following optimization problem:

$$\begin{array}{ll} \text{minimize} & \mathbf{W}^H \widehat{\mathbf{R}}_{xx} \mathbf{W} \\ \text{subject to} & \mathbf{W}^H \mathbf{a}(\overline{\theta}_p) = 1 \end{array} \tag{3.36}$$

where $\mathbf{W}$ is $M \times 1$ complex weight vector and $\overline{\theta}_p$ is the presumed steering direction. This leads to the following weighting:

$$\mathbf{W} = \frac{\widehat{\mathbf{R}}_{xx}^{-1} \mathbf{a}(\overline{\theta}_p)}{\mathbf{a}^H(\overline{\theta}_p) \widehat{\mathbf{R}}_{xx}^{-1} \mathbf{a}(\overline{\theta}_p)} \tag{3.37}$$

and the total beam-former power is:

$$P_0 = \frac{1}{\mathbf{a}^H(\bar{\theta}_p)\widehat{\mathbf{R}}_{xx}^{-1}\mathbf{a}(\bar{\theta}_p)} \tag{3.38}$$

This method has some similarity with Schelkunoff's one because it aims at maximizing the signal received from a certain direction while minimizing the others.
After defining the superdirective arrays and listing some of the most known optimization methods, in the next section we will present some of the practical superdirective array realizations.

3.3 Superdirective Antennas Realizations

In the recent years, a significant research was done on the design of two-element parasitic superdirective arrays [88]-[102]. O'Donnell and Yaghjian showed that, in wire-type arrays, for small distances, the parasitic array (the parasitic element being short-circuited) presents approximately the same directivity as the fully-driven one [88]. The authors studied three different arrays as it can be seen in Figure 3.16. They showed that the parasitic array exhibits a new resonance frequency f_{a0} which is usually lower than the single-element resonance f_0, and two new superdirective resonances f_d, f_r emerge on either side of f_{a0} at which the parasitic element behaves as a director or a reflector.

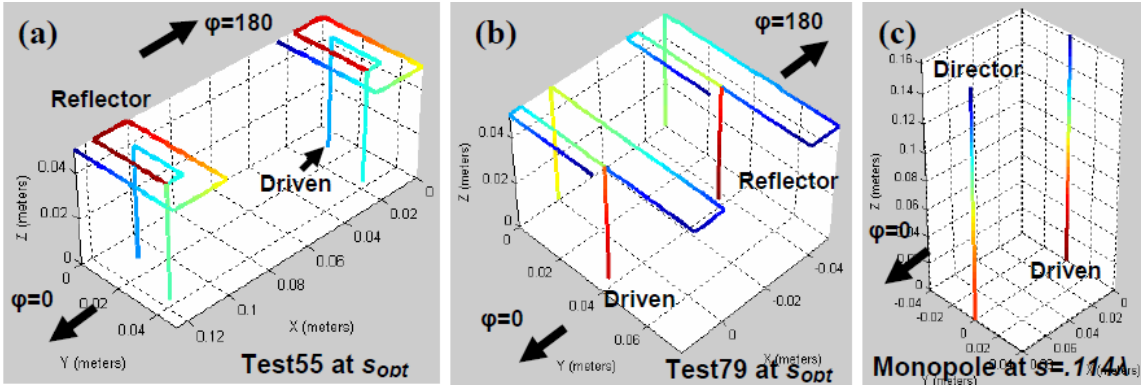

(a)

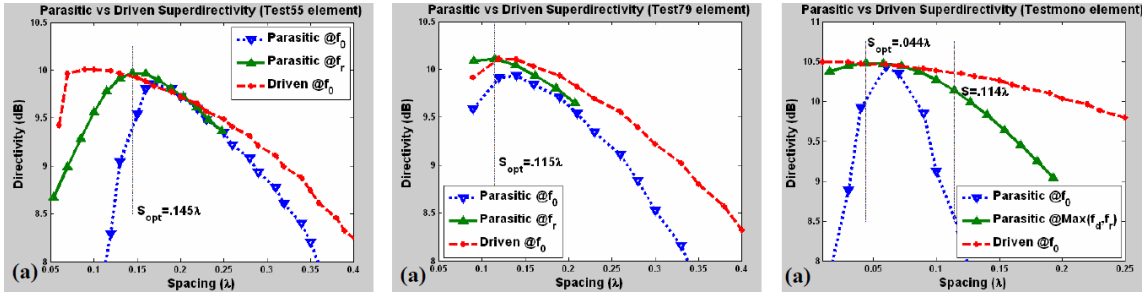

(b)

Figure 3.16: The tested scenarios and the obtained results in [88]. (a) The array geometries and (b) the obtained results.

O'Donnell et al. also studied the effect of the frequency optimization on a parasitic two-element array [89]. The authors compared the current phase differences after

parasitic array frequency optimization to the theoretical phase differences required for driven array to achieve superdirectivity. The authors showed that using the parasitic element as a director can approximately achieve the same results as the fully-driven array for a limited distance range. The authors also tested three different arrays two electrically small ones and a classic monopole. Figure 3.17 shows one of the scenarios and the obtained results.

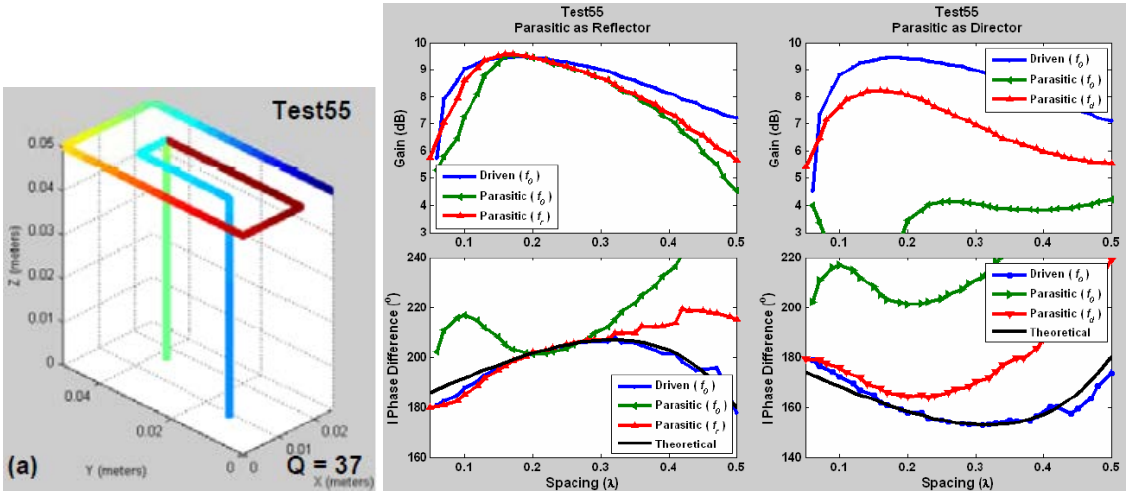

(a) (b)

Figure 3.17: The tested scenarios and the obtained results in [89]. (a) The array geometries and (b) the obtained results.

An efficient electrically small, two-element, closely-spaced and mounted on a ground plane Yagi antenna for the $450MHz$ band was presented in [90]. The antenna total volume was $0.065\lambda \times 0.095\lambda \times 0.095\lambda$ and it presented a measured gain of $8.1dBi$ toward the director direction. Figure 3.18 shows the antenna geometry and obtained results. As it can be noticed, the antenna array presents a significant improvement in the directivity in the forward direction and reduces the backward radiation.

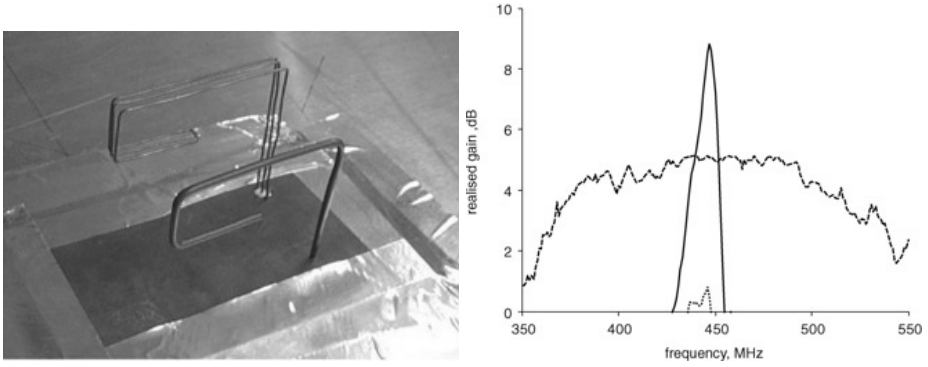

(a) (b)

Figure 3.18: The proposed antenna in [90]. (a) The array geometry and (b) the obtained results (quarter wave monopole (dashed), small Yagi in forward direction (continous) and small Yagi in backward direction (dotted)).

Best et al. presented a two-element impedance-matched multiple arm folded monopole array for $433MHz$ band [91]. The inter-element distance is 0.103λ, the antenna has an impedance bandwidth of $4.9\%(433.7 - 455.3)MHz$. The directivity changes from $10.13dBi$ at $433.7MHz$ to $10.16dBi$ at $455.3MHz$, with a peak of $10.2dBi$ at $443.8MHz$. Figure 3.19 shows the array geometry and the obtained results. It should be noted that one of the elements is matched using tuning capacitors.

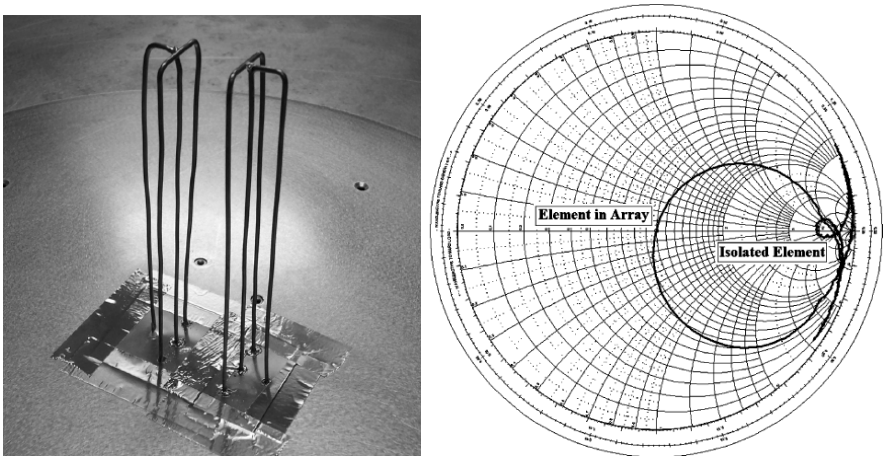

(a) (b)

Figure 3.19: The proposed parasitic antenna in [91]. (a) The array geometry, (b) the input reflection coefficient.

Furthermore, Yaghjian et al. showed possible end-fire supergain 3D wire ESA arrays over a large ground plane [92]. The authors showed that, in both fully-driven and parasitic array, starting from a an inter-element distance of 0.15λ supergain can be achieved. Figure 3.20 shows the driven array designed for $400MHz$ band and Figure 3.21 shows the parasitic array designed for $876MHz$ band.

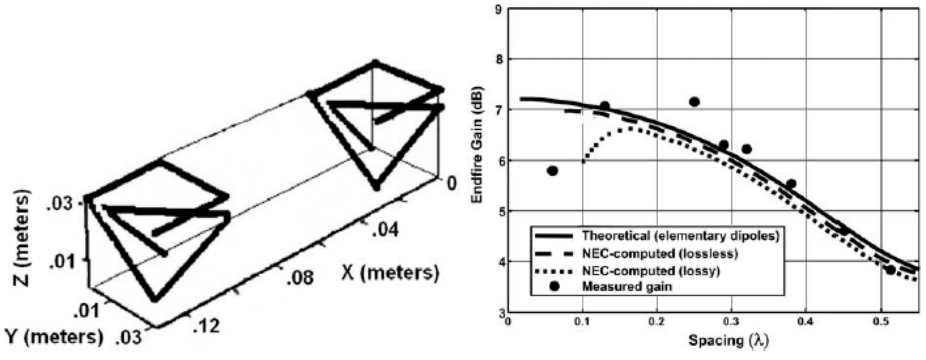

(a) (b)

Figure 3.20: The proposed driven antenna in [92]. (a) The array geometry and (b) the obtained results.

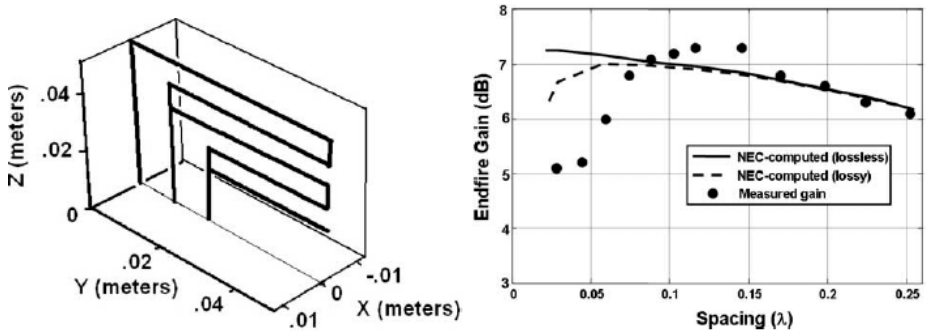

(a) (b)

Figure 3.21: The proposed parasitic antenna in [92]. (a) The array geometry and (b) the gain vs. inter-element spacing.

S. M. Mazinani and H. R. Hassani presented a wide-band array of two planar monopole antenna with loading plates [93]. With an inter-element distance of $2cm$ and a relative phase shift of 135^o, the antenna produces $(3.1 - 7.5)GHz$ impedance bandwidth with $(7.7 - 10.1)dBi$ of directivity (Figure 3.22). This antenna has an efficiency of $60\% - 91\%$ over the bandwidth.

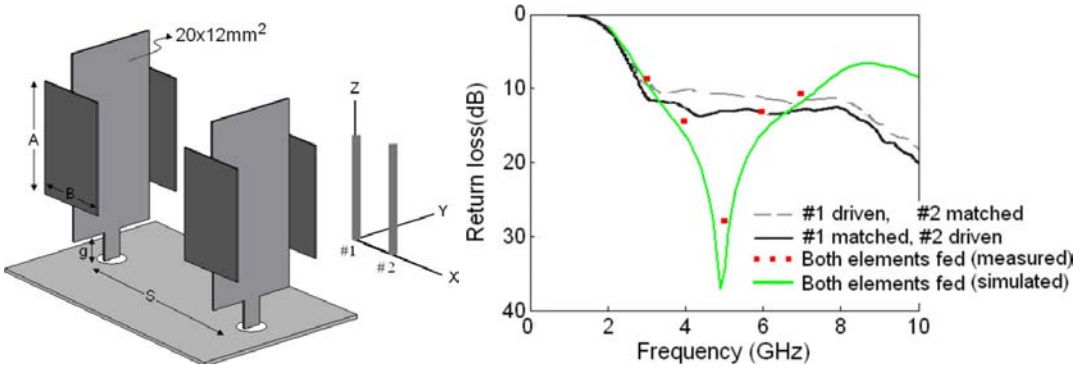

(a) (b)

Figure 3.22: The proposed antenna in [93]. (a) The array geometry and dimensions and (b) the input reflection coefficient magnitude in dB.

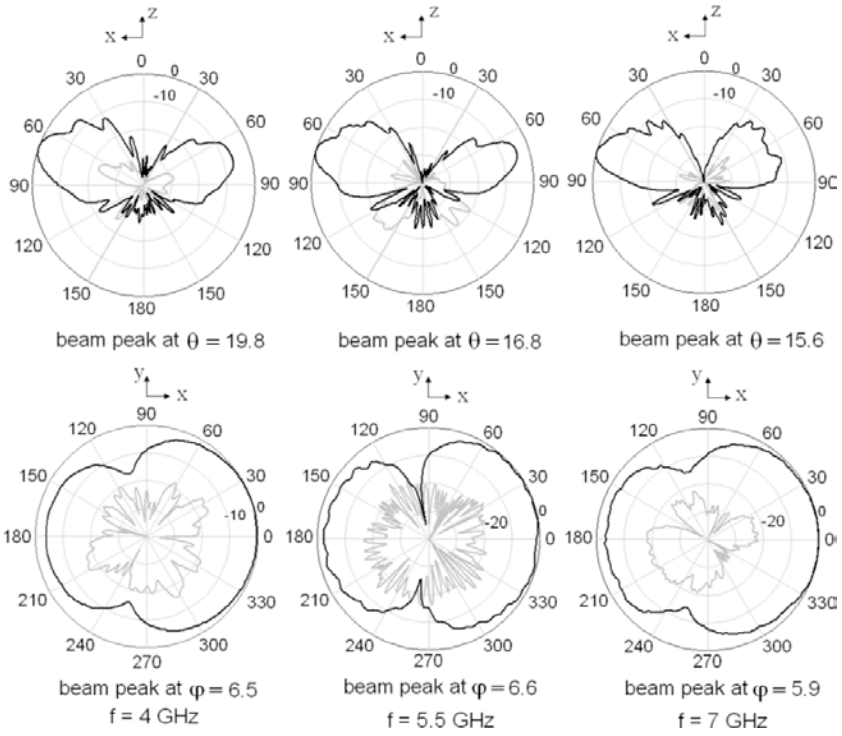

Figure 3.23: The proposed antenna in [93] normalized E-plane and H-plane co-polar (black) and cross-polar (gray) radiation pattern.

In [94] a superdirective array of small resonant magnetic dipole elements is designed on a large ground plane. This array exhibits a high directivity with a good efficiency of 61%. Figure 3.24 shows the antenna geometry and measured radiation patterns. Furthermore, we can note that in most of these superdirective arrays, the authors used one driven-element while short-circuiting the others to let them operate as passive director/reflector in Yagi-Uda like manner.

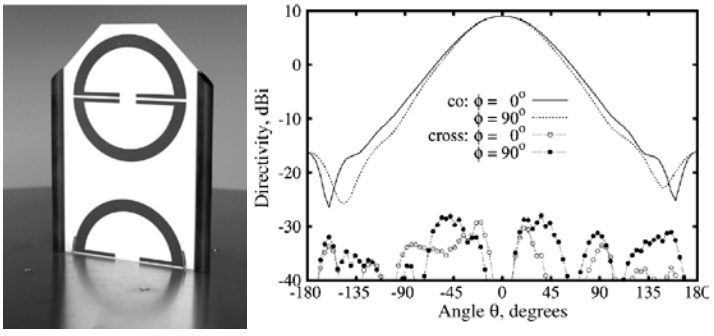

(a) (b)

Figure 3.24: The proposed parasitic antenna in [94]. (a) The array geometry and (b) the obtained results.

In [95], the author presented a modified dual linearly-polarized version of this antanna.
Lugo et al. presentend a superdirective antenna array composed of two closely spaced bow-tie monopoles fed by a power divider associated to a matching network

and a decoupling network for $5.5GHz$ band [96]. The inter-element spacing is 0.13λ and it achieved an experimental directivity of $10dBi$. Figure 3.25 shows the antenna geometry and the obtained results.

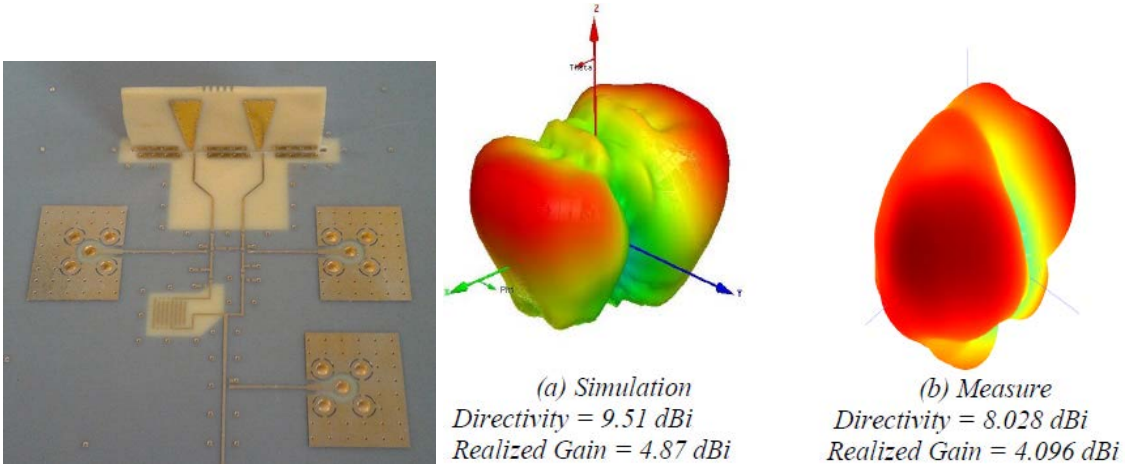

Figure 3.25: The proposed antenna in [96]. (a) The array geometry and (b) the obtained results.

In [97], the authors proposed using non-Foster elements to achieve a broadband parasitic high directive three-element dipole-based array for $868MHz$. The loads associated to each parasitic element were calculated using spherical wave expansion method and the concept was validated by electromagnetic simulations.

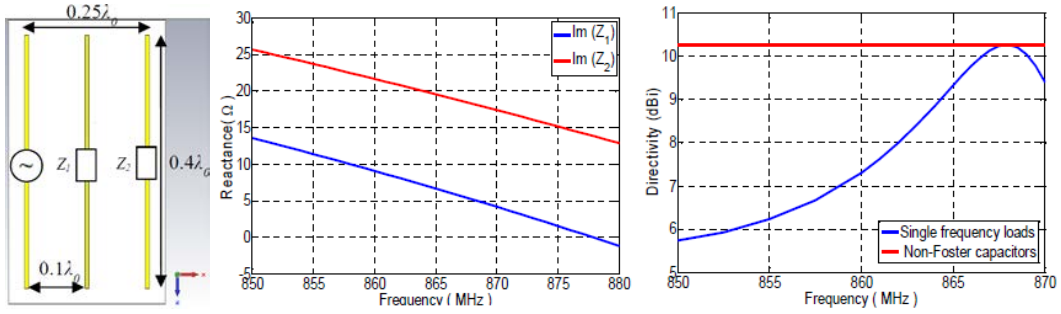

Figure 3.26: The proposed parasitic antenna in [97]. (a) The array geometry, (b) the reactance of the optimal loads associated to the parasitic elements, and (c) the simulated maximum directivity as a function of frequency.

Recently and in analogy with Superdirectivity, the authors in [98] demonstrated that the maximal backscattering of N isotropic antennas is $\frac{N^2(N+1)^2}{4\pi}$ as shown in Figure 3.27. It can be noticed that the backscattering is maximal when the inter-element is zero and as the distance increases it decreases. The authors also implemented a superbackscattering antenna array.

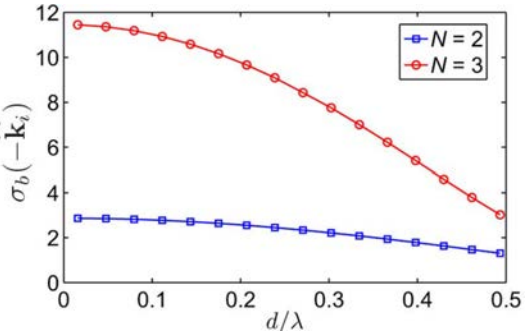

Figure 3.27: Optimized backscattering cross-section of N isotripic elements as a function of the elmenet separation [98].

3.4 Previous Works in IETR

There has been an important work on superdirective antennas in IETR. Jessen Narrainen compared three different methods (Yaghjian, Schelkunoff and Capon) for designing a three-element dipole-based array [99]. The array is designed for $1GHz$ and the dipole length is $144mm$. The obtained simulation results (using 4 NEC 2) shown in Figure 3.28 clearly shows that Yaghjian method presents the highest directivity.

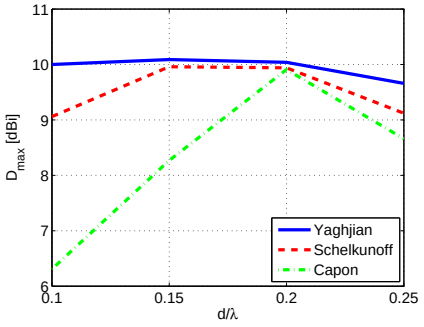

Figure 3.28: The directivity of a three-dipole array vs. spacing as reported in [99].

Later, an ESA printed on a PCB of $70\times110mm^2$ exhibiting a measured directivity of $3dBi$ and an efficiency of 14% was presented [100]. This antenna was then used to design a two-element parasitic array (the parasitic array is open-circuited) for $1.2GHz$ band. The array presented a directivity of $7.76dBi$ and an efficiency of 91.2%. Figure 3.29 shows the antenna geometry and the obtained results.

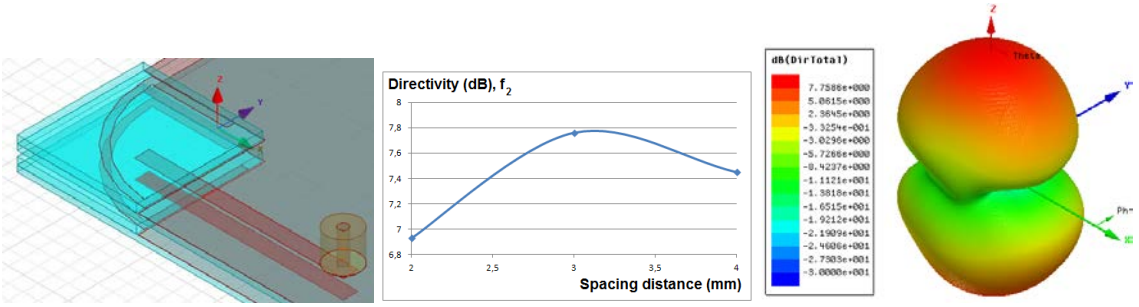

(a) (b) (c)

Figure 3.29: The proposed parasitic antenna in [100]. (a) The array geometry, (b) the total directivity as a function of the spacing and (c) the 3D total directivity radiation pattern for d=3mm.

Recently, a small two-element superdirective antenna array for $890MHz$ band based on a small loop antenna was designed [102]. The inter-element distance was set to 0.08λ, the parasitic element was loaded with a resistor of 300Ω. The antenna largest dimension (diagonal) was 0.14λ and it had a simulated directivity of $5.8dBi$ and radiation efficiency of 1.5%.

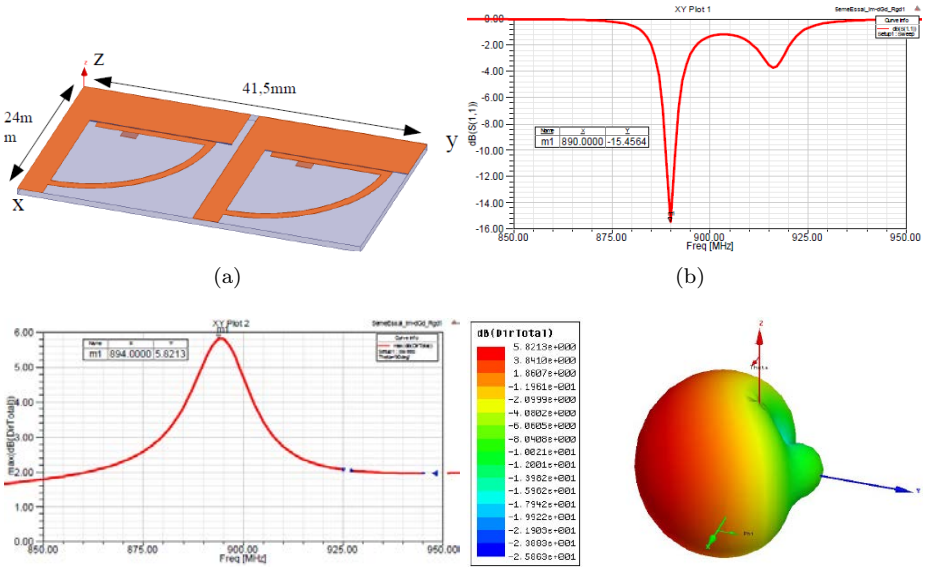

(a) (b) (c) (d)

Figure 3.30: The proposed parasitic antenna in [102]. (a) The array geometry and dimensions, (b) the input reflection coefficient magnitude in dB, (c) the end-fire total directivity as a function of frequency and (c) the 3D total directivity radiation pattern at the design frequency.

3.5 Conclusion

In this chapter, superdirective arrays were defined and their different optimization methods were presented. The state of the art on this kind of arrays was summarized showing that in some parasitic arrays a frequency optimization is required while in others resistive loads are applied which highly reduces the antenna efficiency. On the other hand, in the driven arrays feeding and decoupling networks are required. In the

next chapter, we will propose a simple design approach for parasitic superdirective antenna arrays. The proposed method can be applied for all distances and eliminates the need for feeding and decoupling networks and does not need any frequency optimization.

Chapter 4

Design of Parasitic Superdirective Antenna Arrays

4.1 Introduction

In the first chapter we presented the fundamental limits on Electrically Small Antenna (ESA) performance in function of its dimensions. In the previous chapter we presented the state of the art on superdirective arrays showing that these arrays can overcome Harrington limit on antenna directivity. This chapter presents the work done during this thesis concerning superdirective arrays. The rest of the chapter is organized as follows: First, the theoretical limits of superdirective arrays are studied. Then, a simple approach for designing parasitic superdirective antenna arrays is presented, its practical limitations are investigated and it is used to design ESA-based arrays for UHF band. Next, the integration of of a two-element array in a Printed Circuit Board (PCB) is discussed. After that, the measuring difficulties of such arrays are addressed. Later, the integration of such arrays in compact 3D and planar arrays is also detailed. Finally, the design of Circularly-Polarized (CP) antennas based on superdirective elements is investigated.

4.2 Superdirective Arrays Limits

The well known problems of suprdirctive arrays can be summerized by the efficiency drop and the sensitivity of the array when the number of the elements increases. To analyze theses limits, we consider an superdirective array of N isotropic elements designed following Yaghjian method presented in the previous chapter. It should be noticed that this method was chosen due to the results presented in [99] showing that this method has a very good performance. The excitation coefficients calculation and the achieved directivity of this array were presented in the previous chapter. Figure 4.1 shows the array total directivity and the power radiated by the array for normalized excitation coefficients power, i.e ($\sum_{n=1}^{N} A_n^2 = 1$). This power is calculated as follows:

$$P_{rad} = \frac{1}{2} \oiint_S Re(E \times H^*).ds \approx \frac{1}{2\eta} \oiint_S |E|^2 ds \approx \frac{1}{2\eta} \int_0^{2\pi} \int_0^{\pi} |E|^2 r^2 sin(\theta)\, d\theta\, d\phi \tag{4.1}$$

where η is intrinsic impedance of the medium (air) and r is the radius of the sphere over-which the radiated power is calculated. We can notice that, for a fixed number of elements, as the inter-element distance increases the obtained directivity decreases but radiated power increases. For a fixed distance, as the number of the elements increases, the obtained directivity increases but the radiated power decreases, and as a consequent, so does the radiation efficiency. So it can be concluded that the first theoretical limit is the important drop in the antenna efficiency as the number of the elements increases or the inter-element decreases. This is mainly due to the significant increment in the array excitation coefficients and the phase opposition between the adjacent elements.

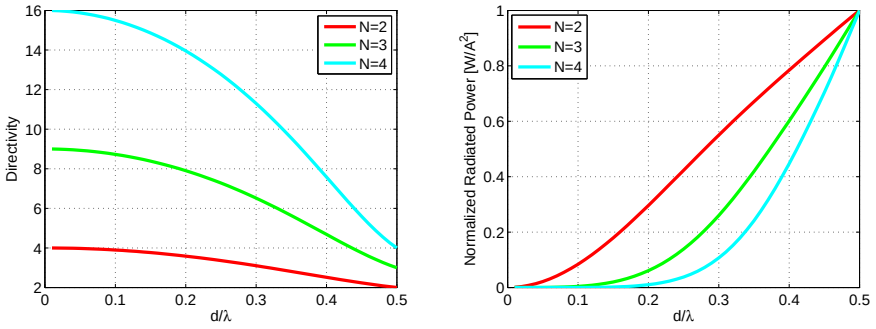

(a) (b)

Figure 4.1: The calculated parameters of N-element d-spaced isotropic superdirective array. (a) End-fire total directivity and (b) normalized transmitted power.

The second limit is the sensitivity of the superdirectivity. To put this forward, we re-calculated the directivity of an array of N isotropic elements when the coefficients magnitudes are estimated with an error of 5% or the phases are shifted by 5^o. Figure 4.2 shows the obtained results (since the symmetric elements have equal magnitudes, the array sensitivity toward the errors in these elements excitation is also the same, so they are not shown).

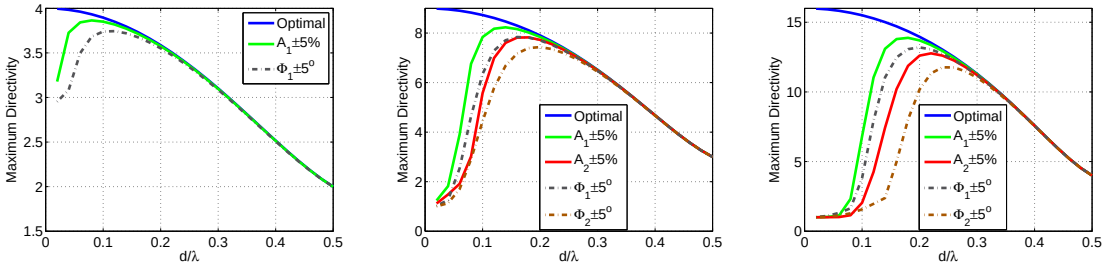

(a) (b) (c)

Figure 4.2: The effect of the error in the coefficients estimation on the directivity of N-element, d-spaced isotropic array. (a) N=2, (b) N=3 and (c) N=4.

It may be noted that, for small spacing, and due to the high excitation magnitudes, the array is very sensitive to the changes in the coefficients. It is also possible to notice that, for a fixed distance, increasing the number of the elements increases

the sensitivity of the directivity. For a distance $d = 0.1\lambda$ an error 5% in the estimation of first element magnitude reduces the directivity by 1.1%, 10.2% or 56.1% in case an array of two-, three- or four-elements, respectively. It is also observed that for an array of N elements, the array is more sensitive to the changes in the coefficients of the middle elements. This is due to the fact that the magnitudes of these coefficients are higher, and hence, their participation in the array radiation is higher.

4.3 Proposed Design Approach

In order to facilitate the design of superdirective arrays based on realistic (non-isotropic) antennas, we developed a design methodology that takes into account the antenna real parameters as presented in the flow chart given in Figure 4.3.

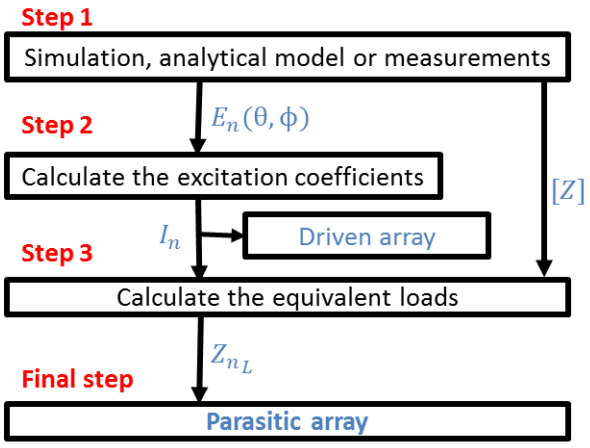

Figure 4.3: A flow chart of the proposed design methodology.

- In the first step, the antenna array is simulated via an electromagnetic simulator, ANSYS HFSS in our case [103], to obtain the radiated electrical field for each element in the entire space and the array impedance matrix.
- The radiated electrical fields are integrated in Uzkov-Altshuler equations to calculate the required excitation coefficients, i.e.

$$a_{0n} = [H^*_{mn}]^{-1} e^{-jk\hat{r_0}r_m} f^*_m(\theta_0,\phi_0) f_n(\theta_0,\phi_0) \tag{4.2}$$

and

$$H_{mn} = \frac{1}{4\pi}\int_0^{2\pi}\int_0^{\pi} f_m(\theta,\phi) f^*_n(\theta,\phi) e^{jk\hat{r}(r_m - r_n)} sin(\theta)\, d\theta\, d\phi \tag{4.3}$$

- However, in our case, and since the far field patterns' equations are not known, HFSS results are used instead and the following approximation for H_{mn} is used:

$$H_{mn} = \frac{1}{4\pi}\sum_{\theta=0}^{2\pi}\sum_{\phi=0}^{\pi} f_m(\theta,\phi) f^*_n(\theta,\phi) e^{jk\hat{r}(r_m - r_n)} sin(\theta)\Delta(\theta)\Delta(\phi) \tag{4.4}$$

where $\Delta(\theta) = \frac{2\pi}{N_\theta}$ and $\Delta(\phi) = \frac{\pi}{N_\phi}$ are the far field sampling step in spherical angles (θ,ϕ), N_θ and N_ϕ being the number of samples.

- It is well known that Equation 3.27 is the limit of Equation 4.4 when $\Delta(\theta)$ and $\Delta(\phi)$ tend to zero (N_θ and N_ϕ tend to infinity) [104]. Hence, the obtained parameters need to be slightly modified to maximize the directivity of the array.
- Then, the array voltage excitation coefficients vector [V] can be calculated as follows:

$$[V] = [Z][I] \Leftrightarrow V(n) = \sum_{m=1}^{N} Z_{nm} I_m \tag{4.5}$$

  where $[Z]$ is the array impedance matrix.
- Hence, the array active impedance vector [77] can be deduced from:

$$Z_{active}(n) = \frac{V(n)}{I(n)} = Z_{nn} + \sum_{\substack{m=1 \\ m \neq n}}^{N} Z_{nm} \frac{I_m}{I_n} \tag{4.6}$$

- Finally, one element can be excited while others can be loaded to obtain the same directivity as in the case of exciting all the elements. The load value is given by:

$$Z_L(n) = -Z_{active}(n) \tag{4.7}$$

It should be noticed that the impedance of the driven element (n) after loading the others can easily be calculated by collapsing a multi-port network to a one port. This impedance is given by [105]:

$$Z_{in} = Z_{nn} + \frac{1}{M_{nn}} \sum_{\substack{m=1 \\ m \neq n}}^{N} Z_{nm} C_{nm} \tag{4.8}$$

where M_{ij} is the minor obtained by deleting the row i and column j of the matrix $Z + Z_L$ and $C_{nm} = (-1)^{n+m} M_{nm}$. In the case of two-elements (n, m), when exiting element n and loading m, this impedance is given by:

$$Z_{in} = Z_{nn} - \frac{Z_{nm} Z_{mn}}{Z_{mm} + Z_L(m)} \tag{4.9}$$

and in the case of three elements (l, n, m), exciting l and loading the two others, this impedance is given by:

$$Z_{in} = Z_{ll} + \frac{Z_{ln} Z_{nl} (Z_{L(m)} + Z_{mm}) + Z_{lm} Z_{ml} (Z_{L(n)} + Z_{nn}) - Z_{ln} Z_{nm} Z_{ml} - Z_{lm} Z_{mn} Z_{nl}}{Z_{nm} Z_{mn} - (Z_{L(n)} + Z_{nn})(Z_{L(m)} + Z_{mm})} \tag{4.10}$$

In the next section, we will study the practical limitations of superdirective arrays based on full wave simulation of different dipole-based arrays.

4.3.1 Practical Limitations

To understand the proposed method's practical limitations, several parametric analysis based on dipole-based arrays are performed. The unit-element used in these analysis is a dipole of length ($l = 145mm$) and diameter ($d = 1mm$). This dipole

has a simulated resonance frequency around $1GHz$ and a quasi-omnidirectional radiation pattern with a maximum total directivity of $2.4dBi$.
We consider two-, three-, and four-element arrays with an inter-element distance varying from 0.05λ to 0.5λ. For each distance, first, the array excitation coefficients to maximize the end-fire ($\theta = 90, \phi = 0$) directivity at $1GHz$ are calculated. Then, the required loads are deduced and the array is transformed to a parasitic (loaded) one. For every distance, each time a different element is excited while the others are loaded.

4.3.1.1 Two-Elements Array

Figure 4.4(a) shows the maximum total directivity of the two-element array. The figure shows that due to the small mutual coupling, even for small distances the excitation coefficients can accurately be calculated. Hence, the theoretical limits for the antenna maximum end-fire directivity can be attained. Furthermore, the figure shows that both parasitic array configurations present almost the same total directivity. Figure 4.4(b) shows the obtained maximum total directivity when exciting the second element and neglecting the required negative resistances. It can be noticed that due to the small value of the required negative resistance neglecting it has a very small effect on the antenna directivity. Figure 4.9 shows that in this case, even for small distances a radiation efficiency of around 100% can be attained and the supergain can be achieved.

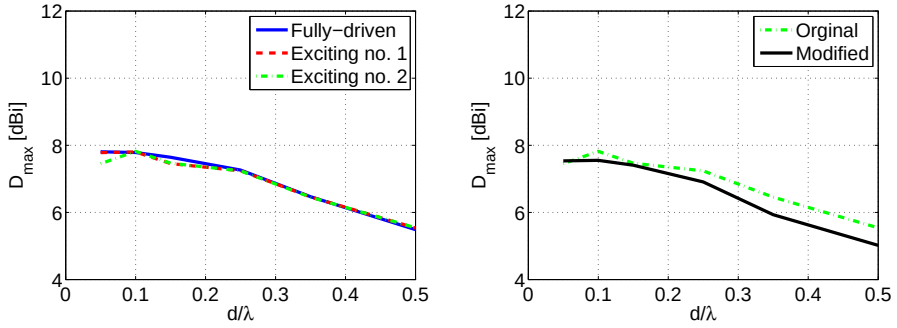

(a) (b)

Figure 4.4: Two-dipole array simulated total end-fire directivity. (a) Exciting the different elements and (b) exciting the second element and neglecting the negative resistances.

4.3.1.2 Three-Elements Array

The calculated excitation coefficients of the three-element array are given in Figure 4.5. The calculated required loads given in Figure 4.6 shows that, for small distances, two small negative resistances are required. As the distance increases, the value of the required negative resistances also increases and starting from 0.25λ three negative resistances are required. As for the required reactances, they are of capacitor nature with an increasing value with the distance.

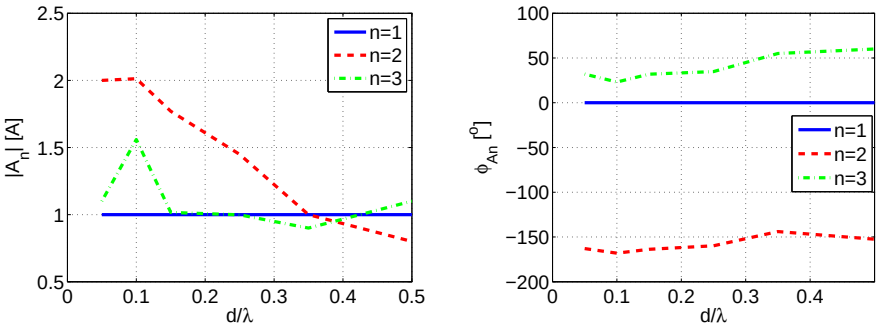

(a) (b)

Figure 4.5: Three-dipole array calculated excitation coefficients. (a) Magnitude and (b) phase.

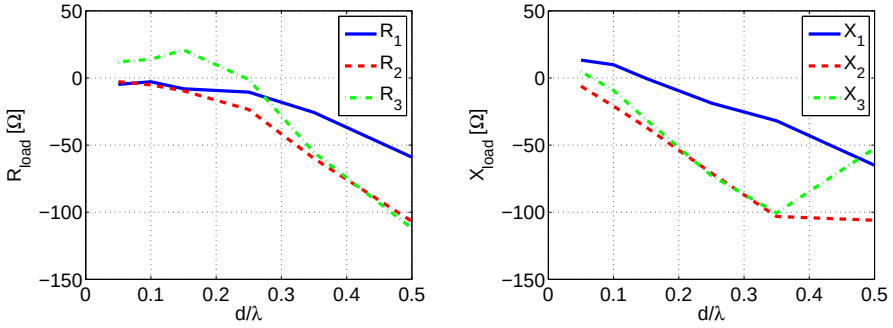

(a) (b)

Figure 4.6: Three-dipole array calculated required loads. (a) Resistance and (b) reactance.

Figure 4.7(a) shows the maximum directivity versus the inter-element distance. The figure shows that for small distances the maximum theoretical directivity cannot be attained. This is due to the high coupling in this case that results to a high sensitivity of the total radiation pattern to the excitation coefficients as is well described in [82]. The figure also shows that the different parasitic arrays achieve almost the same results as the fully driven one. Figure 4.7(b) shows the obtained maximum total directivity exciting the second element and neglecting the required negative resistances. It can be noticed that for small distances, neglecting the small negative resistance has a very limited effect on the antenna directivity. However, as the distance increases, due to neglecting two considerable negative resistances, the directivity degradation becomes more important.

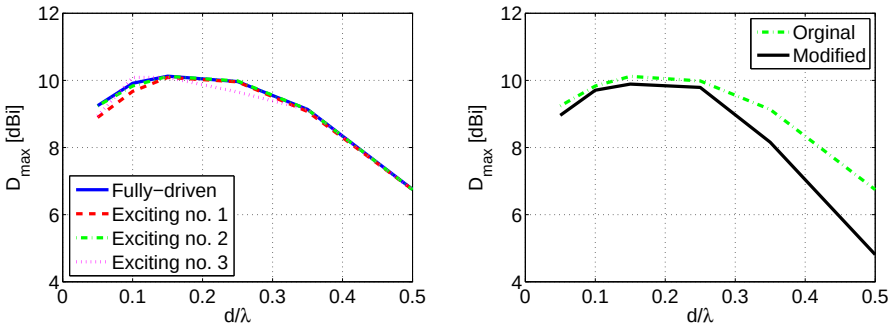

(a) (b)

Figure 4.7: Three-dipole array simulated total end-fire directivity. (a) Exciting the different elements and (b) exciting the second element and neglecting the negative resistances.

Finally, Figure 4.9 shows the array simulated radiation efficiency in this case. Due to the high mutual coupling and thus the significant ohmic loss resistances, the array has a very low radiation efficiency for small inter-element distance. However, as the distance increases the radiation efficiency also increases and around $d = 0.25\lambda$ this efficiency reaches 100%, and hence, not only superdirectivity can be achieved but also supergain.

4.3.1.3 Four-Elements Array

Fig 4.8(a) shows the obtained directivity of the four-element array. The figure shows that this array presents approximately the same directivity as the three-element one. This is due to the high sensitivity of the antenna directivity to the excitation coefficients as the number of the elements increases as shown in [106]. The figure also shows a considerable difference between the antenna directivity exciting the different elements. This is also due to the high sensitivity to the excitation coefficients. Figure 4.8(b) shows the obtained maximum total directivity when exciting the second element and neglecting the required negative resistances.

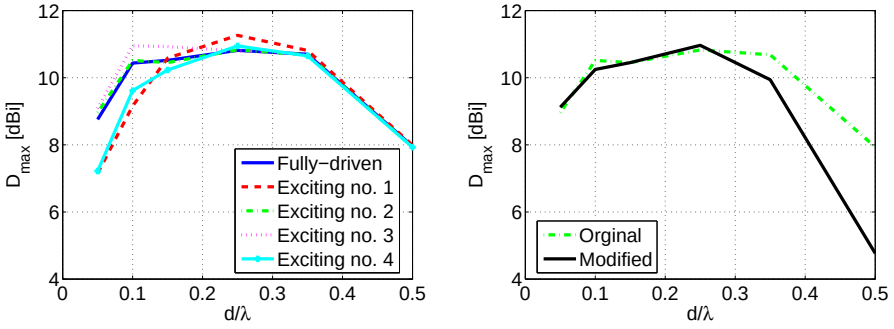

(a) (b)

Figure 4.8: Four-dipole array simulated total end-fire directivity. (a) Exciting the different elements and (b) exciting the second element and neglecting the negative resistances.

Figure 4.9 shows that in this case, even for relatively high distances the array has a very low radiation efficiency, and hence, the supergain cannot be achieved. The

antenna radiation efficiency reaches 100% when the inter-element distance is bigger than 0.3λ.

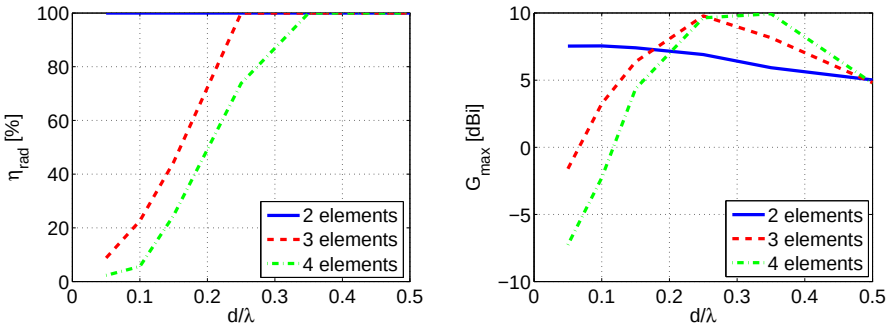

Figure 4.9: Simulated parameters of the different arrays when exciting the second element and neglecting the negative resistances. (a) radiation efficiency and (b) total gain in dB.

From this study it can be concluded that the proposed method is limited by the sensitivity in calculating the excitation coefficients and the attainable radiation efficiency as the number of the elements increases and the inter-element decreases. The results reveal that this sensitivity to the excitation coefficients do not decrease the antenna maximum end-fire directivity by more than $1dBi$ for two-, three- and four-element arrays if the spacing of the array elements is larger than about 0.05λ, 0.1λ and 0.2λ, respectively. However, once the excitation coefficients are calculated, the proposed loading method is not limited by the number of the elements nor by the inter-element distance. This analysis also showed that, due to practical limits and difficulties, the conception of superdirective arrays is a trade-off between array's directivity, radiation efficiency and size (number of elements and inter-element spacing). In the next section we will use the proposed design methodology to design different parasitic arrays based on Electrically Small Antennas (ESAs).

4.3.2 Application on ESAs

The proposed method was used to design multiple arrays based on three different ESAs namely a small spiral, a metamaterial inspired loop and a folded monopole.

4.3.2.1 Spiral-Based Array

The unit-element used in this study is a miniaturized spiral antenna [107]. This antenna is printed on a 0.835mm-thick FR4 substrate. The antenna total dimensions are approximately $25 \times 14.3mm^2(\frac{\lambda}{13} * \frac{\lambda}{23})$. The antenna has a $-10dB$ bandwidth of approximately $7.3MHz$ at a central frequency of $927MHz$. It has a directivity of $2.67dBi$ and a radiation efficiency of 6%. Figure 4.10(a), shows the antenna geometry and corresponding dimensions. Figure 4.10(b), shows the antenna simulated input reflection coefficient and Figure 4.10(c), shows the antenna simulated radiation pattern.

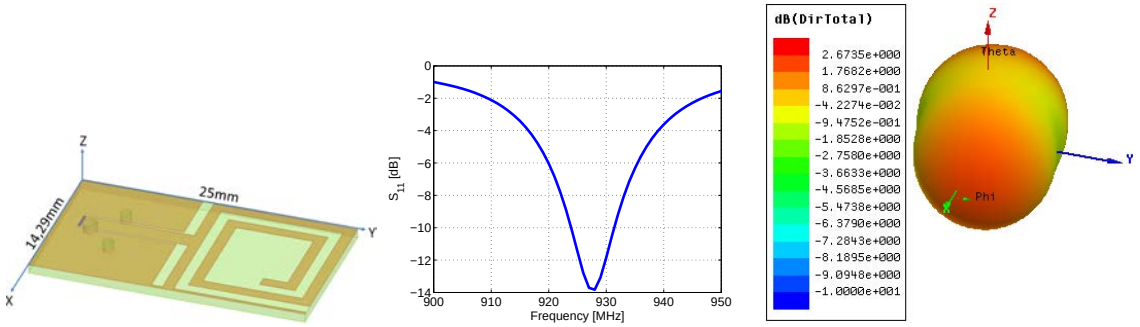

(a) (b) (c)

Figure 4.10: Miniaturized spiral antenna. (a) Antenna geometry and dimensions, (b) simulated input reflection coefficient magnitude in DB and (c) simulated 3D total directivity radiation pattern.

A two-element array with an inter-element distance of 0.05λ was designed. In this array where one element is fed and the second is loaded with a capacitor of $7.19pF$, a maximum total directivity of $5.7dBi$ is achieved. However, the array has a poor efficiency of 0.8%. This can be attributed to the high loss substrate (FR4) used in the design, the antenna very compact size, as well as the high mutual coupling in superdirective arrays. Figure 4.11(a) shows the array geometry and dimensions as well as the surface current distribution.[1] It can be noticed that the current on the two elements is out of phase, which is the condition for obtaining superdirectivity for very small inter-element distances. Figure 4.11(b) shows the array's simulated 3D directivity radiation patterns. The figure shows a well polarized pattern where the maximum co-polar directivity is the same as the total one. The figure also shows a small cross-polar radiation on the Z-axis with a maximum of $-2.2dBi$. The HPBW in horizontal and vertical planes (XOY and XOZ) are respectively 96^o and 116^o and the FBR is equal to $11.8dB$.

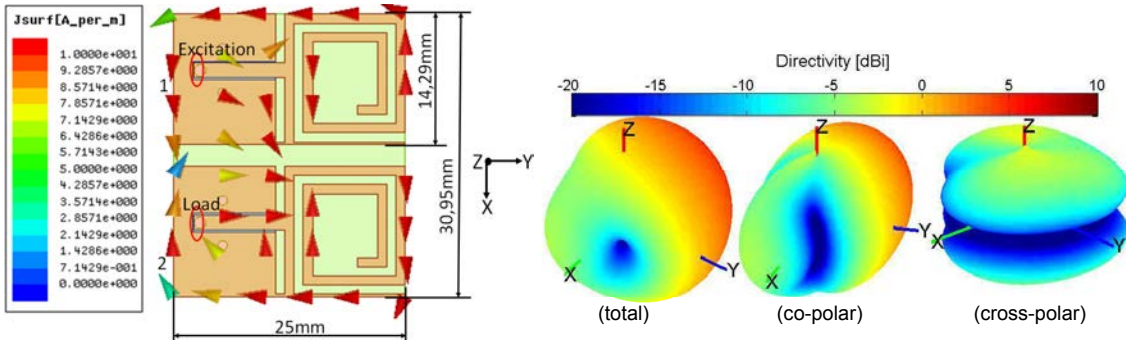

(a) (b)

Figure 4.11: Reference array. (a) Geometry, corresponding dimensions and surface current distribution and (b) simulated 3D directivity radiation patterns.

4.3.2.1.1 Integrating a Two-Element Array in a PCB

Due to the superdirectivity sensitivity to the surrounding environment, the integration of an array in a bigger PCB is not an easy task. Simply placing the antenna on

[1] In order to facilitate the comparison between the different scenarios, the same color-bar scale $(0 - 10[Amp/m])$ is used for all cases.

one corner of the PCB will lead to a complete lost of the superdirectivity phenomena. In this section, we will investigate, via different scenarios, the integration of a the previous array in a PCB with total dimensions of $110 \times 70 mm^2$. In each scenario the antenna is placed on a different location on the PCB. The array excitation coefficients are determined as detailed before to obtain the maximum end-fire directivity. Then, the array is transformed to a parasitic one where the first element is excited while the second one (refer to Figure 4.11(a) for elements notation) is loaded. The scenarios are evaluated based on the array directivity and radiation efficiency.

Scenario One Now the array is located on the top-left corner of the PCB. The ground plane of the antenna is directly connected to the one of the PCB. The antenna is $5mm$ away from the right-side of the PCB ground plane. Since the two elements have a common ground plane now, changing one element's excitation affects the current distribution on both elements. Hence, optimal current distribution cannot be achieved. Figure 4.12(a) shows the current distribution on the PCB in this case. We can note that only a small portion of the PCB is highly induced, and hence, the array efficiency improvement is limited (8.6%). The figure also shows that current on the PCB mainly flows in the X-axis direction, and hence, the PCB act as a monopole in the XOY plane and along X-axis. This is seen in the radiation pattern as a quasi-omnidirectional pattern in the YOZ plane and a null in the X-axis direction. However, since the current distribution on the two spirals is significantly higher than the one on the PCB, and the current on the two spirals being out of phase, the maximum directivity is still in the end-fire direction. Furthermore, the antenna is no longer superdirective, the array maximum total directivity is decreased to $2.7dBi$. The HPBW in horizontal and vertical planes are now 120^o and 128^o and the FBR level is equal to $10.9dB$. Figure 4.12(b) shows the simulated 3D directivity radiation patterns. The figure shows a significant increment in the cross-polar radiation with a maximum of $-0.2dBi$ in Z-axis direction.

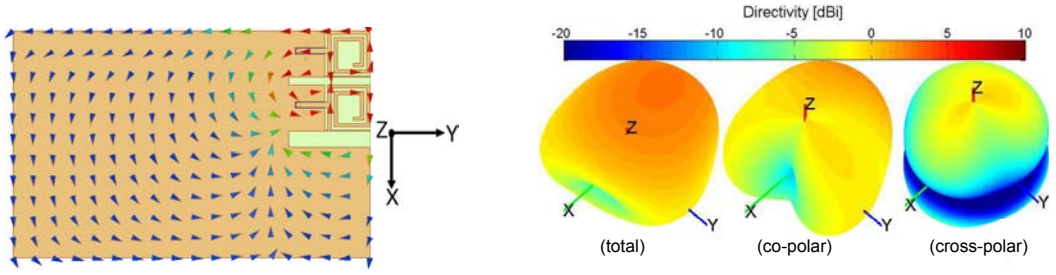

(a) (b)

Figure 4.12: Scenario one. (a) Geometry and surface current distribution and (b) simulated 3D directivity radiation patterns.

To reduce the negative effect of the PCB and depending on the current distribution seen previously, in the following scenarios we propose to first symmetrize the structure and second to add some slots to the PCB to change its current distribution.

Scenario Two In this scenario, the array is located on the top-center of the PCB. The PCB ground plane is divided into two sections and each section is connected to one element's ground plane. The separating distance between the two sections is

the same as the one between the two array elements ($2.38mm$). The array is $5mm$ away form the ground plane of the PCB on both sides. Figure 4.13(a) shows the current distribution on the PCB. The figure shows a significant current distribution on the PCB with the highest density being on the two sides of the separating slot, and hence, the array radiation efficiency is significantly improved to 15.9%. The figure also shows that the current on the two PCB portions is directional and out of phase (which reduces the radiation contribution of the PCB and improves the superdirectivity effect for very small separating distances), and hence, a good superdirectivity effect can be monitored. The array has a maximum total directivity of $5.9dBi$. The HPBW in horizontal and vertical planes are now respectively 80^o, 118^o and the FBR level is equal to $6dB$. Finally, the current on the two PCB sections surrounding the antenna array opposes the current on the rest of the PCB, and hence it slightly reduces the maximum achieved directivity and increases the antenna HPBW. Figure 4.13(b) shows the simulated 3D directivity radiation patterns. The figure shows a fairly polarized pattern where the maximum co-polar directivity is the same as the total one. The maximum cross-polar directivity is about $-3.1dBi$ in Z-axis direction.

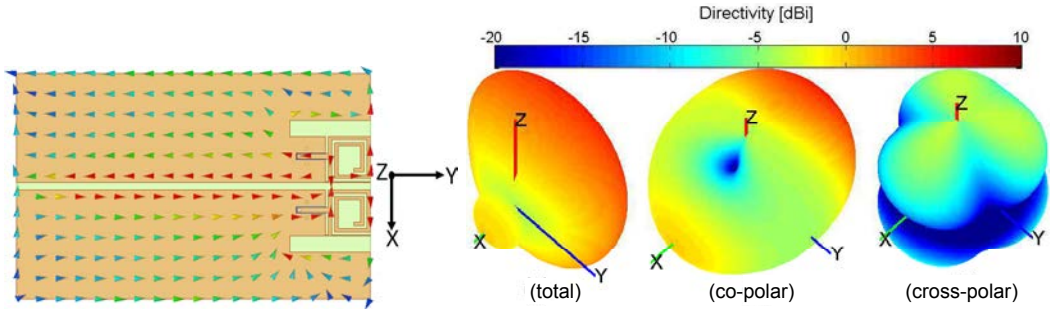

(a) (b)

Figure 4.13: Scenario two. (a) Geometry and surface current distribution and (b) simulated 3D directivity radiation patterns.

Scenario Three In this scenario, the two PCB sections that were surrounding the array elements in scenario two are removed. The distance between the two PCB sections is reduced to $0.5mm$ (this choice will be justified in the following section). Figure 4.14(a) shows the current distribution on the PCB. A behavior similar to the previous scenario is noticed with a very high current distribution on the PCB. The figure also shows that the current on the entire two PCB sections is directional and out of phase, and hence, a good superdirectivity can be achieved. The array has a maximum total directivity of $7.2dBi$ and a radiation efficiency of 12.7%. The HPBW in horizontal and vertical planes are now respectively 74^o, 108^o and the FBR level is equal to $6.1dB$. Figure 4.14(b) shows the simulated 3D directivity radiation patterns. The figure shows a further improvement in the array polarization. A small cross-polar radiation is observed on the Z-axis while this radiation is negligible elsewhere.

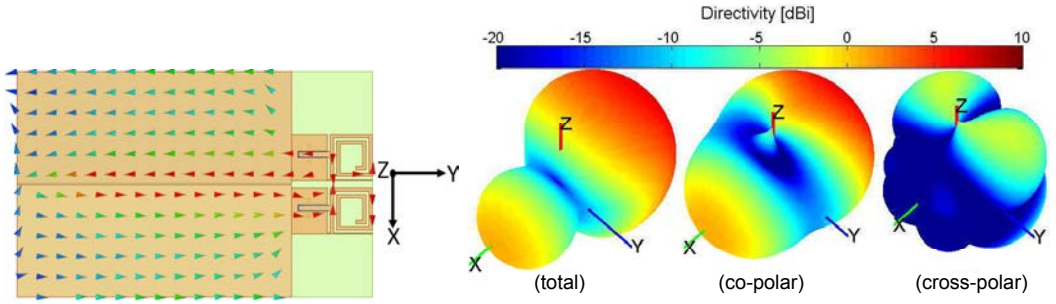

(a) (b)

Figure 4.14: Scenario three. (a) Geometry and surface current distribution and (b) simulated 3D directivity radiation patterns.

Table 4.1 summarizes the obtained results. The table clearly shows that scenario three is the best one, where we have an efficiency improvement by a factor of 16 and a directivity improvement of $1.5dB$ (a gain improvement of $13.6dB$).

Table 4.1: A summary of the simulated obtained results for different PCB integration configurations.

Scenario	$\eta[\%]$	η/η_{ref}	$D_{max}[dBi]$	$D_{max} - D_{ref_{max}}[dB]$
Reference	0.8	1	5.7	0
One	8.6	10.8	2.7	-3
Two	15.9	19.9	5.9	0.2
Three	12.7	15.9	7.2	1.5

Slot Effect To investigate the effect of the slot size between the two PCB sections on the array performance, the slot size in scenario three is varied from 0 to $30mm$ while the array's efficiency, directivity and input reflection coefficient are monitored. The effect of the slot size on the array directivity and efficiency are given in Figure 4.15(a). The figure shows that when the two PCB sections are connected, the array presents a minimal directivity as was seen in the fist scenario. Then, for a very small distance the array presents a maximal directivity and as the distance between the two sections increases the array directivity decreases. The figure also shows that the array efficiency increases with the slot size. This is mainly due to mitigating the effect of mutual coupling as the slot size increases which can be seen as an increment of the antenna electrical size. The slot size effect on the array reflection coefficient is given in Figure 4.15(b). The figure shows that as the slot size increases, the array resonance frequency decreases and the resonance level gets worse. From this study we can conclude that a slot size of $0.5mm$ is a good compromise between the array efficiency, maximum directivity and impedance matching.

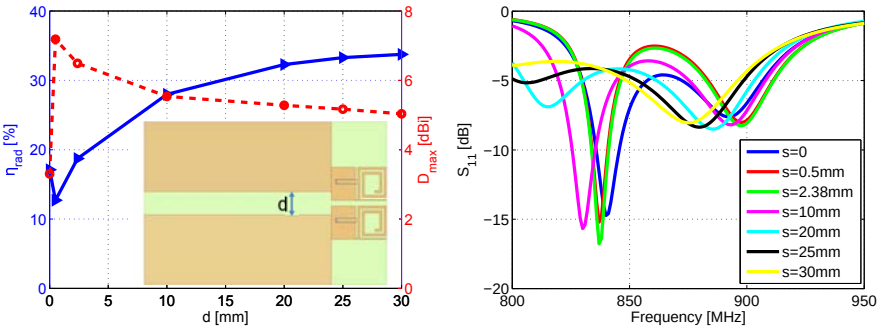

(a) (b)

Figure 4.15: The slot size effect on the array performance. (a) Maximum directivity and radiation efficiency and (b) input reflection coefficient.

Since scenario three presented the best performance, in the next section we will study the measurement difficulties concerning this scenario.

4.3.2.1.2 Measurements Difficulties

ESAs have low efficiencies and omni-directional radiation patterns. Consequently, they are not easy to be measured due to the severe effect of the coaxial cable, even though such a cable may not be present in the final application of the antenna. A poorly balanced antenna can result in common mode currents flowing on the feeding cable surface, which radiates and distorts the true radiation pattern of the Antenna Under-Test (AUT) [108]. There have been many reports about the influence of the coaxial cable on measured characteristics of ESAs (refer to [109] and the references therein). Furthermore, superdirective ESAs add the additional challenge of maintaining the superdirective pattern with the presence of the coaxial cable. This problem was highlighted in multiple works [101, 102]. In this section, we will study different scenarios for connecting the SMA connector and the coaxial cable to the antenna in order to minimize the cable radiation effect.

Scenario One In this scenario, the excitation system is directly connected to the array driven element as shown in Figure 4.16(a). Due to the excitation proximity to the radiating element the cable radiation affects the array radiation pattern. Hence, the array has equal radiation in both end-fire directions. Figures 4.20 compares the array input reflection coefficient in this scenario to the reference scenario one. As it can be noticed, the array original resonance frequency of $837MHz$ did not change. Figure 4.16(b) shows the array directivity radiation patterns. The figure shows that the superdirectivity effect is disturbed and the array maximum total directivity is reduced to $5.7dBi$. The figure also shows that the array co-polar directivity is reduced to $5.1dBi$ while the cross-polar one is augmented to $1dBi$. The HPBW in horizontal and vertical planes are respectively 82^o and 106^o and the FBR is equal to $3.2dB$ (Figure 4.21).

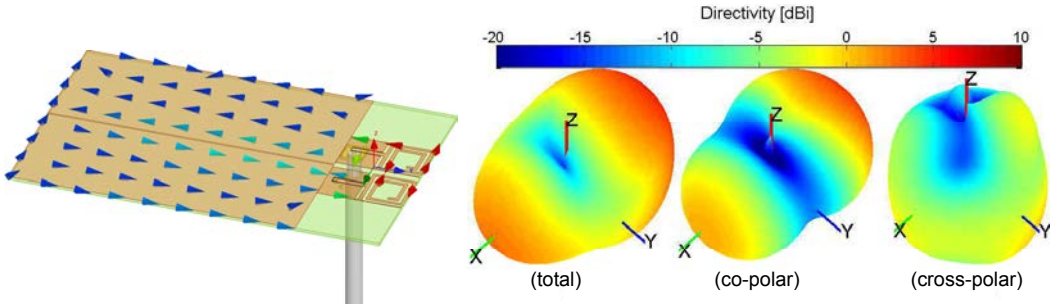

(a) (b)

Figure 4.16: Feeding scenario one. (a) Geometry and surface current distribution and (b) simulated 3D directivity radiation patterns.

Scenario Two In order to reduce the the excitation system effect, the array excitation is extended to the extreme-side of the PCB where a minimal surface current distribution is observed. Figure 4.17(a) shows that the current distribution is maximal around the excitation line and the slot between the two ground planes. On the other side, the rest of the ground plane has negligible contribution in the array radiation. Figure 4.20 shows that the array resonance frequency is shifted to $835MHz$ and its matching is lost. This can be attributed to the high coupling between the slot between the two PCB parts and the excitation line, which results in changing the characteristic impedance of the coplanar excitation line. Figure 4.17(b) shows that the array superdirective radiation pattern is also lost and the array has a maximum total directivity of $3.7dBi$. The figure also shows a comparable co-polar and cross-polar directivity (about $2.5dBi$). The HPBW in horizontal and vertical planes are respectively 322^o and 208^o and the FBR is equal to $2.1dB$ (Figure 4.21).

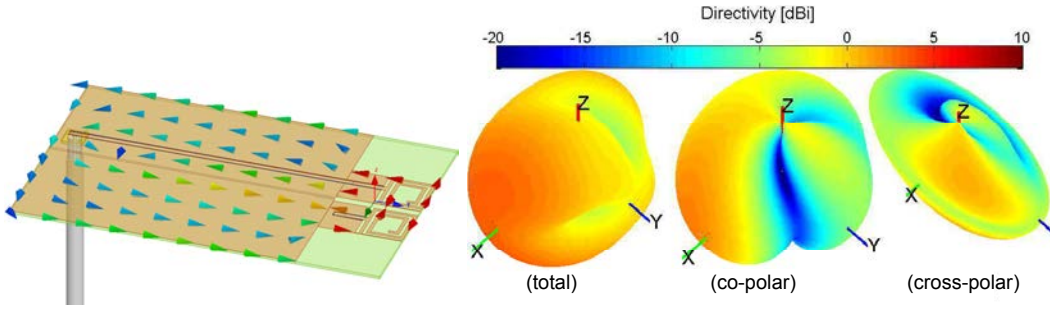

(a) (b)

Figure 4.17: Feeding scenario two. (a) Geometry and surface current distribution and (b) simulated 3D directivity radiation patterns.

Scenario Three In this scenario, the array excitation line is extended to the left-side of the PCB where also a minimal current distribution on the array surface is observed. Figure 4.18(a) shows the array geometry in this scenario and the surface current distribution. The Figure shows that the current distribution is approximately the same as in the reference scenario. Consequently, the cable radiation is mitigated and the array both input reflection coefficient and radiation pattern are preserved. Figure 4.20 shows that the array original resonance frequency of $837MHz$

is shifted to $840MHz$. Furthermore, Figure 4.18(b) shows that the array is superdirective with a maximum total directivity of $6.8dBi$. The array co-polar directivity is $6.6dBi$ while the cross-polar one is $-1dBi$. The HPBW in horizontal and vertical planes are 76^o and 110^o respectively and the FBR is equal to $6.4dB$ (Figure 4.21).

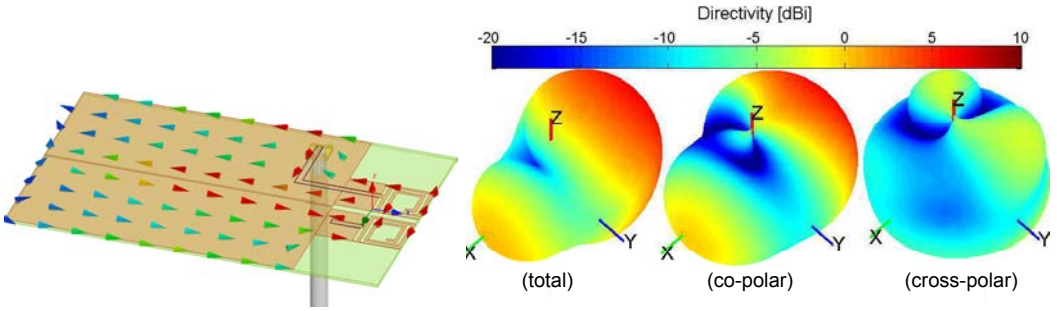

(a) (b)

Figure 4.18: Feeding scenario three. (a) Geometry and surface current distribution and (b) simulated 3D directivity radiation patterns.

Scenario Four This scenario is similar to the previous one, however, a horizontal the excitation system is connected to the array. Figure 4.19(a) shows the array geometry and surface current distribution. The figure also shows that the current distribution is similar to the reference scenario's one. Hence, as it can be noticed from Figure 4.19(b) the array original superdirective radiation pattern is maintained with a maximum total directivity of $6.8dBi$. It can also be noticed that the array co-polar directivity is about $6.8dBi$ while the cross-polar one is about $-1dBi$. The HPBW in horizontal and vertical planes are respectively 72^o and 118^o and the FBR is equal to $6.8dB$ (Figure 4.21). Figure 4.20 shows that the array resonance frequency is shifted to $841MHz$.

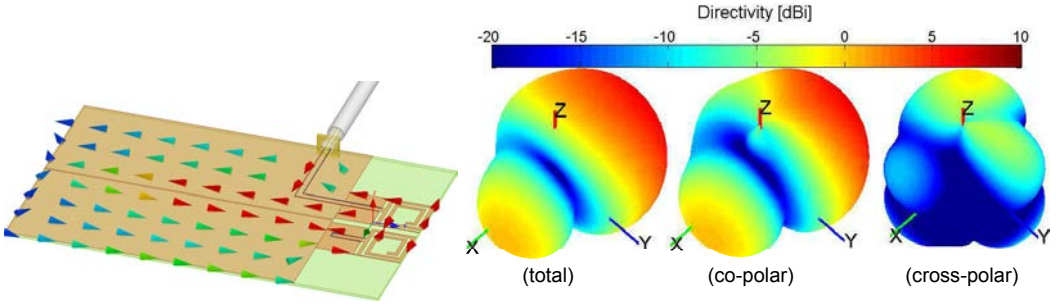

(a) (b)

Figure 4.19: Feeding scenario four. (a) Geometry and surface current distribution and (b) simulated 3D directivity radiation patterns.

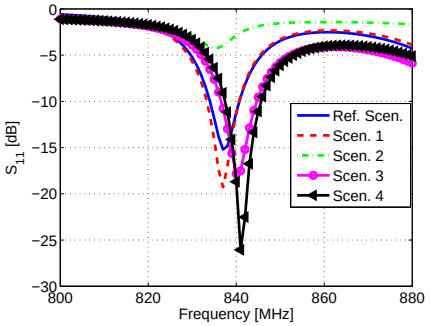

Figure 4.20: Simulated input reflection coefficient magnitude for all scenarios.

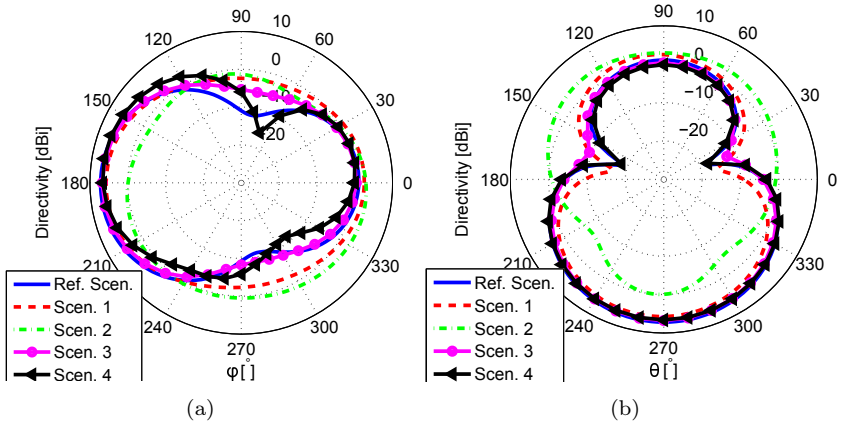

Figure 4.21: Simulated 2D total directivity radiation pattern for all scenarios. (a) Horizontal plane and (b) vertical plane.

Results Validation via Measurements To validate the simulation results, prototypes of scenarios one, three and four were fabricated and measured. Photographs of the prototypes are given in Figure 4.22.

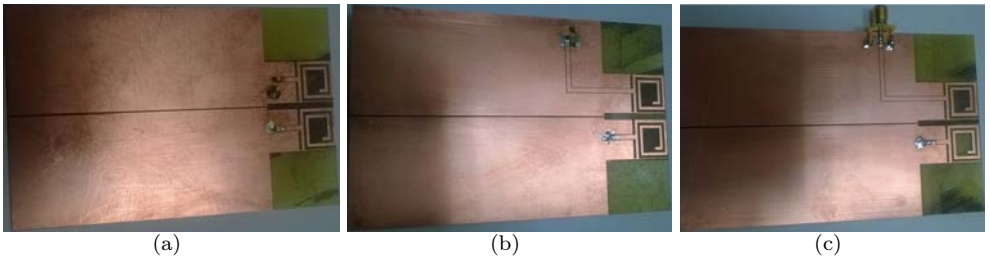

Figure 4.22: Photographs of the fabricated prototypes. (a) Scenarios one, (b) scenarios two and (c) scenarios three.

The measured input reflection coefficient for different scenarios is given in Figure 4.23. The obtained resonance frequencies are in very good agreement with simulated ones. A difference less than 2% is noticed for all scenarios. This difference is probably due to the dispersion of the commercial SMD loads. The measured resonances are wider than the simulated ones while the measured resonances are weaker than the

simulated ones. This can be due to higher dielectric losses in measurement than simulation.

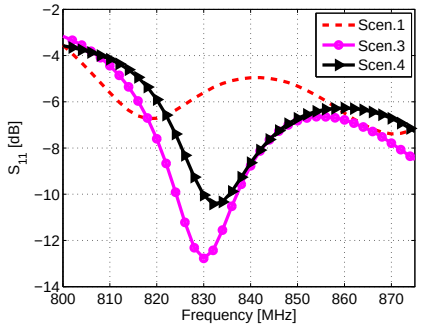

Figure 4.23: Measured input reflection coefficient magnitude for different scenarios.

The 3D far-field radiation patterns are measured in SATIMO stargate (SG 32) near-field measurement system and shown in Figure 4.24. There is a good agreement with the simulation results in the main beam direction. The difference in the backward direction can be attributed to the measuring system and environment. The measured HPBW in horizontal and vertical planes are respectively 84^o and 118^o for scenario one, 79^o and 136^o four scenario three and 68^o and 89^o for scenario four. The maximum total directivity for the three scenarios are respectively $5.6dBi$, $5.9dBi$ and $7.3dBi$. Finally, Figure 4.25 shows the measured 3D total directivity radiation patterns for scenarios one, three and four.

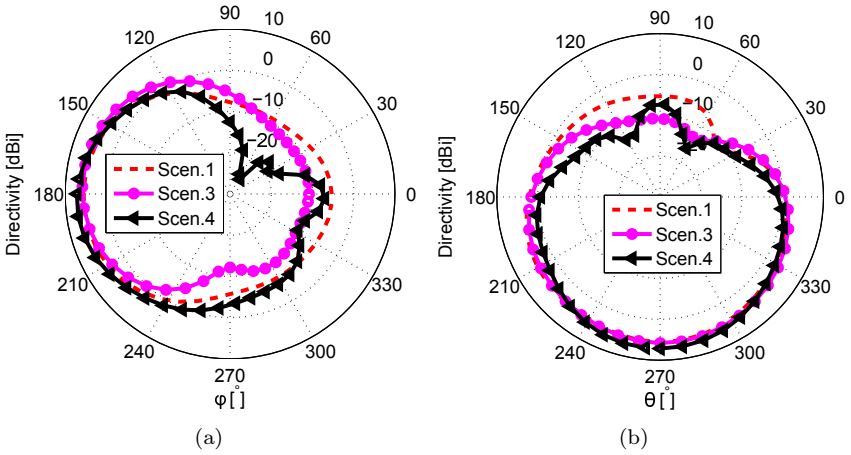

Figure 4.24: Measured 2D total directivity radiation pattern for different scenarios. (a) Horizontal plane and (b) vertical plane.

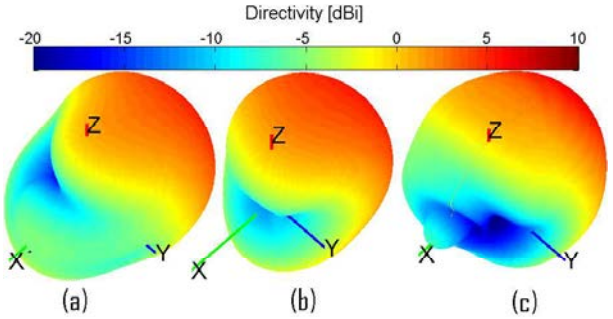

Figure 4.25: Measured 3D total directivity radiation patterns for different scenarios. (a) Scenario one, (b) scenario three and (c) scenario four.

Table 4.2 lists the antenna simulated and measured resonance frequency (f_c) and maximum total directivity (D_{max}) for all scenarios.

Table 4.2: A summary of the simulated and measured results of different coaxial cable connection configurations.

Scenario	Simulation		Measurement	
	$f_c[MHz]$	$D_{max}[dBi]$	$f_c[MHz]$	$D_{max}[dBi]$
Reference	837	7.2	-	-
One	837	5.7	818	5.6
Two	835	3.7	-	-
Three	840	6.8	830	5.9
Four	841	6.8	832	7.3

In this section, measuring superdirective ESAs integrated in PCBs was investigated. Different scenarios for connecting the excitation system to the antenna were evaluated. The obtained results showed that a proper connection of the excitation system can reduce its negative effects, and hence, the antenna can be measured. It should be noticed that each antenna is a particular case, hence a similar study should be performed to investigate the optimal feeding configuration. To design relatively efficient superdirective arrays, one should start with unit elements with an acceptable efficiency. Hence, in the following sections more efficient unit-elements will be used.

4.3.2.2 Loop-Based Arrays

The proposed method was also used to design different ESA-based planar arrays with an inter-element distance of $34.3mm(0.1\lambda)$. The unit-element used in these arrays is a miniaturized printed half-loop antenna. The loop is shorted to the ground plane and loaded by a capacitance to reduce its dimensions. This capacitance is realized by two metallic strips separated by a gap of $0.1mm$. The antenna is fed by coupling through a microstrip line located on the bottom side. The antenna is printed on a 0.8mm-thick Rogers RO4003 substrate and its dimensions are $24mm \times 20mm$ corresponding to $\frac{\lambda}{14} \times \frac{\lambda}{17}$ for a resonance frequency of $906MHz$. The antenna has an impedance bandwidth of $2.6MHz$.[2] It has a simulated total directivity of $2.2dBi$ and radiation efficiency of 32%. Figure 4.26(a) shows the antenna geometry

[2] The ($S_{11} < -6dB$) criterion will be considered for the impedance bandwidth, while $D_{max} - 1dB$ will be considered for the directivity one.

and dimensions, Figure 4.26(b) shows its input reflection coefficient magnitude and Figure 4.26(c) shows its quasi-isotropic total directivity radiation pattern with a null following z-axis.

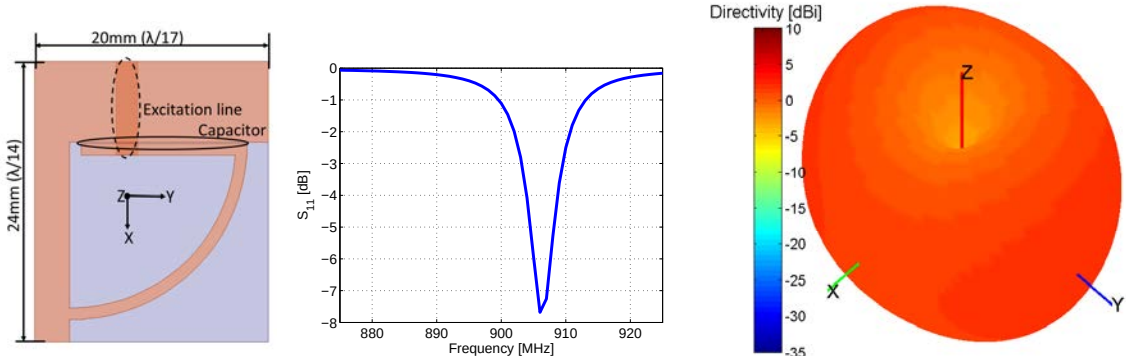

(a) (b) (c)

Figure 4.26: The miniaturized unit-element. (a) Geometry and dimensions, (b) simulated input reflection coefficient magnitude and (c) simulated 3D total directivity radiation pattern.

4.3.2.2.1 Two-Element Array

Figure 4.27(a) shows this array's geometry and dimensions. Figure 4.27(b) shows that, due to mutual coupling, the antenna resonance frequency is shifted to $905MHz$, hence, the array is designed for this frequency with a size factor ($ka = 0.56$).

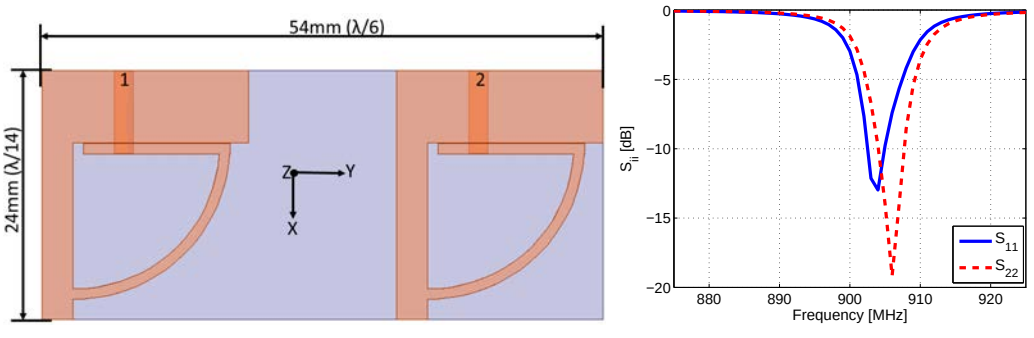

(a) (b)

Figure 4.27: Two-element array. (a) Geometry and dimensions and (b) simulated input reflection coefficient magnitude.

Exciting the second element with a current of $1.32e^{j150.4^o}$ relative to the first one, a maximum total directivity of $7.1dBi$ is achieved at the same frequency. In the parasitic array, where the first element is excited while the second one is loaded with a capacitor of $5.1pF$, a maximum directivity in the end-fire direction of $7dBi$ is achieved. Due to the limited efficiency of the unit-element and the mutual coupling, the array radiation efficiency decreases to 7.1%. Figure 4.28 shows the simulated 3D total directivity radiation patterns for both the fully-driven array and the parasitic one.

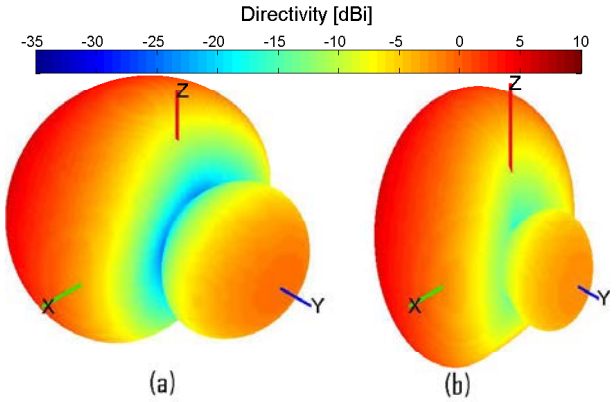

Figure 4.28: Two-element array's simulated 3D total directivity radiation pattern. (a) Fully-driven array and (b) parasitic one.

Figure 4.29 shows both the driven and parasitic array's 2D radiation patterns in horizontal and vertical planes (XOY and YOZ). The figure shows a very good agreement between the two cases. In the fully driven array, the Half-Power Beamwidth (HPBW) in horizontal and vertical planes are respectively 105^o and 80^o and the Front to Back Ratio (FBR) is equal to $7.8dB$. In the parasitic array, the HPBW in horizontal and vertical planes are respectively 110^o and 80^o and the FBR is equal to $9dB$.

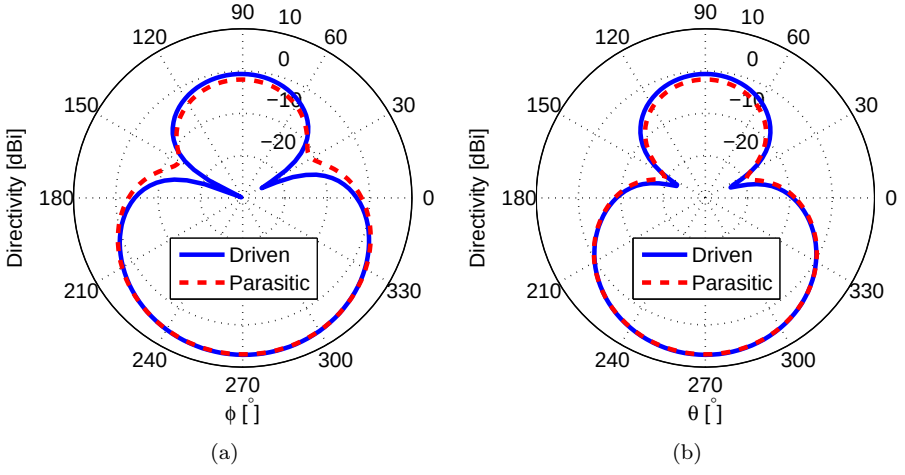

Figure 4.29: Two-element array's simulated 2D total directivity radiation patterns. (a) Horizontal plane and (b) vertical plane.

Figure 4.30 shows that the parasitic array end-fire total directivity ($D_{(\theta=90^o,\phi=270^o)}$) is maximal around the antenna resonance of $905MHz$. The array has an impedance bandwidth of $2.1MHz$ and an adjacent resonance frequency appears. The array has a directivity bandwidth of $1.7MHz$.

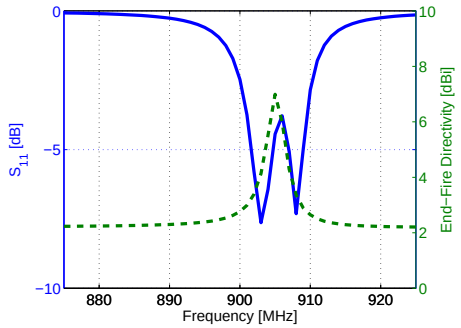

Figure 4.30: Parasitic two-element array's simulated input reflection coefficient magnitude and end-fire total directivity.

Finally Figure 4.31 shows that the surface current distribution of parasitic array is similar to the one of the fully-driven array (the same color range will be used for the upcoming arrays). Furthermore, as expected, we can note that the current on the two elements is out of phase.

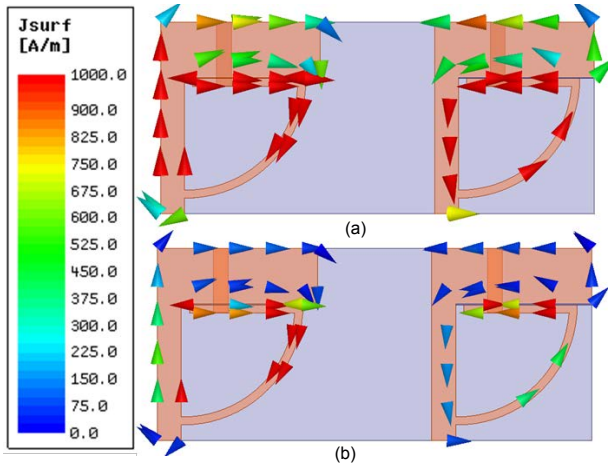

Figure 4.31: Two-element array's simulated surface current distribution.(a) Fully-driven array and (b) parasitic one.

However due to this array very small size ($\frac{\lambda}{6.1} \times \frac{\lambda}{13.8}$), the results cannot be validated via measurements. To put forward this problem, the antenna was simulated with an SMA connector and a 20cm-long coxial cable in the antenna plane (horizontal) or vertical to it as shown in Figure 4.32.

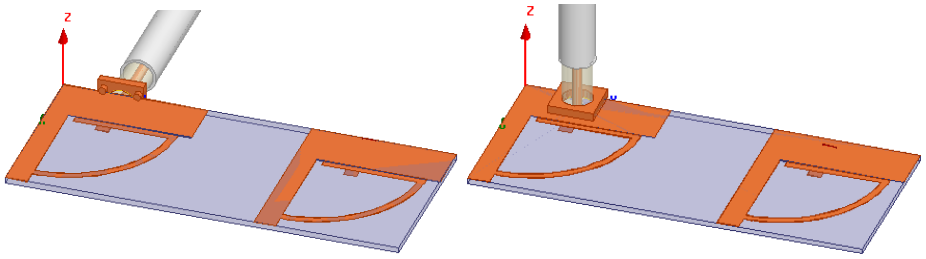

(a) (b)

Figure 4.32: Two-element array simulation with (a) a horizontal coaxial cable and (b) a vertical one.

The simulated input reflection coefficient magnitude in dB given in Figure 4.33 shows that the resonance frequency is shifted to $890MHz$. This can be attributed to the cable participation in the antenna radiation which can be seen as an increment in the antenna radiation aperture.

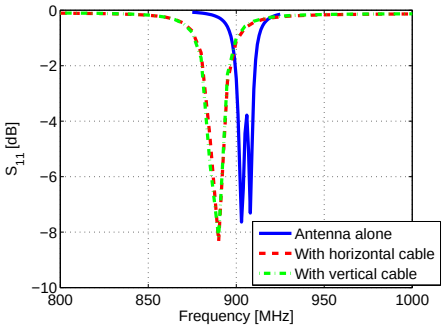

Figure 4.33: Two-element array simulated S_{11} in dB with an excitation cable.

The antenna simulated 3D total directivity radiation pattern given in Figure 4.34 shows that in both cases the radiation pattern has a null following the cable axis implying that it is mainly dominated by the cable radiation. The importance of the cable radiation can also be observed from the antenna simulated radiation efficiency which is increased from the original one of 7.1% to around 78%.

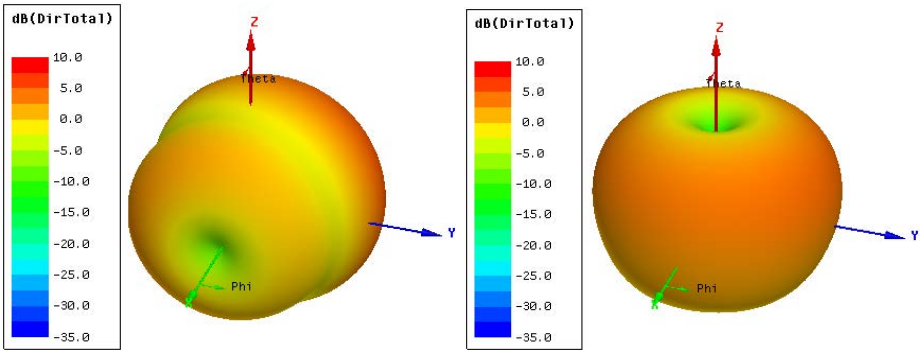

(a) (b)

Figure 4.34: Two-element array simulated 3D total directivity radiation pattern at the design frequency with (a) a horizontal coaxial cable and (b) a vertical one.

To facilitate the antenna measurements, the following antennas will be designed with a bigger ground plane as done before.

4.3.2.2.2 Two-Element Array on a PCB

The previous array is integrated in a PCB with total dimensions of $110 \times 70mm^2$. Figure 4.35(a) shows the antenna geometry and dimensions. The slot size of $5mm$ is chosen to obtain a good compromise between the obtained maximum directivity and radiation efficiency. Figure 4.35(b) shows the input reflection coefficient magnitude of both elements. We can note that, in this case, and due to the mutual coupling and the big size of the ground plane, the antenna resonance frequency is shifted to $866MHz$. Hence, the array is designed for this frequency with a size factor ($ka = 1.18$).

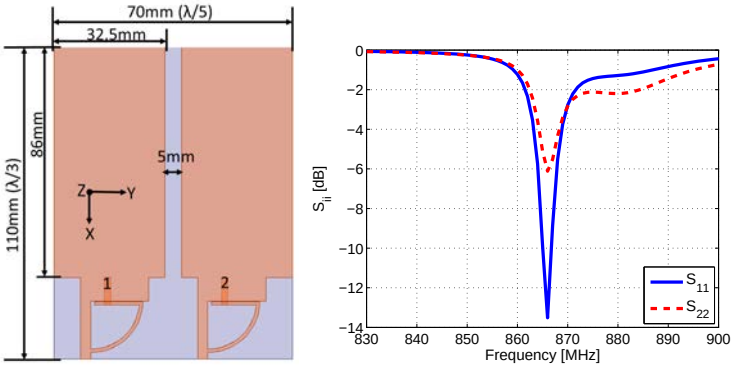

(a) (b)

Figure 4.35: Two-element array mounted on a PCB. (a) Geometry and dimensions and (b) simulated input reflection coefficient magnitude.

Exciting the second element with a current of $0.55e^{-j101.6^o}$ relative the first one, a maximum total directivity of $7.2dBi$ is achieved. In the parasitic array, where the second element is excited while the first one is loaded with an inductor of $4.35nH$, a maximum directivity of $7.2dBi$ is also achieved. Figure 4.36 illustrates the 3D total directivity radiation patterns and Figure 4.37 shows 2D radiation patterns in horizontal and vertical planes. We can see an excellent agreement between the two cases where the HPBW in horizontal and vertical planes are respectively 74° and 110°. The fully-driven array's FBR is about $7.2dB$ while the parasitic array's one is about $8.4dB$.

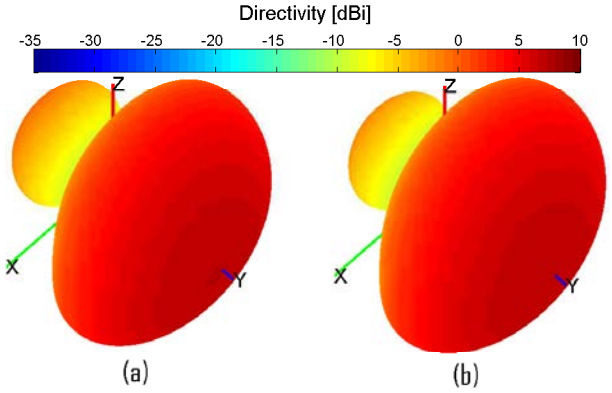

Figure 4.36: Two-element array mounted on a PCB's simulated 3D total directivity radiation pattern. (a) Fully-driven array and (b) parasitic one.

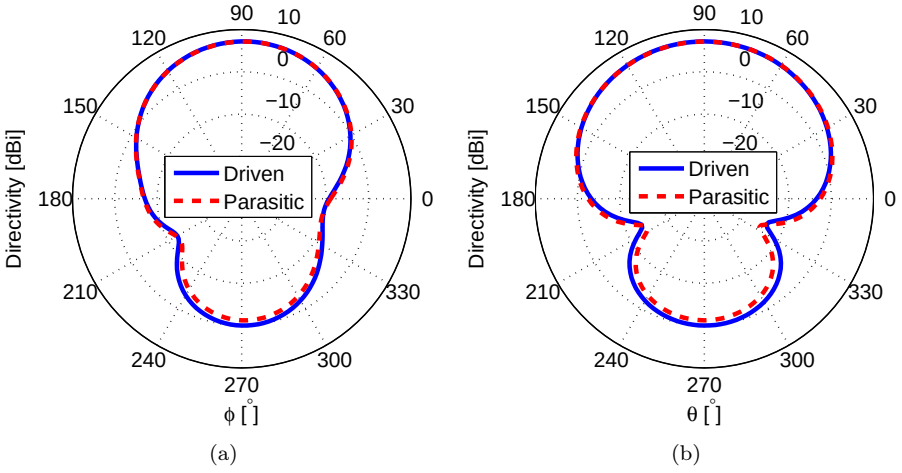

Figure 4.37: Two-element array mounted on a PCB's simulated 2D total directivity radiation patterns. (a) Horizontal plane and (b) vertical plane.

As in the previous scenario, Figure 4.38 shows that the parasitic array end-fire total directivity ($D_{(\theta=90^o,\phi=90^o)}$) is maximal around the antenna resonance of $866MHz$. The array has an impedance bandwidth of $2MHz$ a directivity bandwidth of $5.7MHz$. In this case, we can monitor the effect of ground plane in ESAs that contributes to the antenna radiation where the antenna radiation efficiency is increased to 62%. Finally, Figure 4.39 shows shows the same surface current distribution in the fully-driven and the parasitic array.

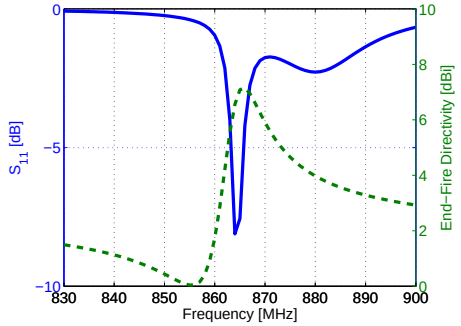

Figure 4.38: Parasitic two-element array mounted on a PCB's simulated input reflection coefficient magnitude and end-fire total directivity.

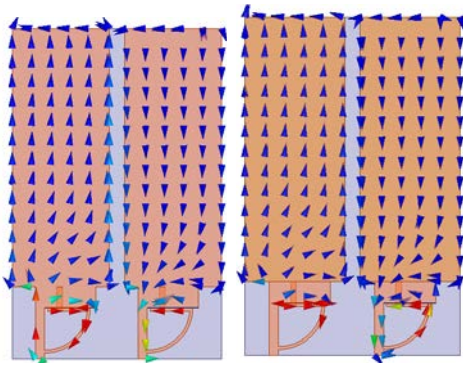

(a) (b)

Figure 4.39: Two-element array mounted on a PCB's simulated surface current distribution.(a) Fully-driven array and (b) parasitic one.

A prototype of this array was fabricated and measured for results validation (Figure 4.40(a)). Figure 4.40(b) shows the antenna measured input reflection coefficient magnitude. The measured resonance frequency is $901MHz$ (a frequency shift of 4.2%). This shift is probably due to the cable and the connector effects as well as the dispersion of the commercial SMD loads. The antenna bandwidth is $3.6MHz$. The antenna 3D far-field radiation pattern was measured in SATIMO stargate (SG 32) near-field measurement system. The measured 3D total directivity radiation pattern at the resonance frequency is given in Figure 4.40(c). The figure shows a superdirective radiation pattern with a maximum total directivity of $6.8dBi$.

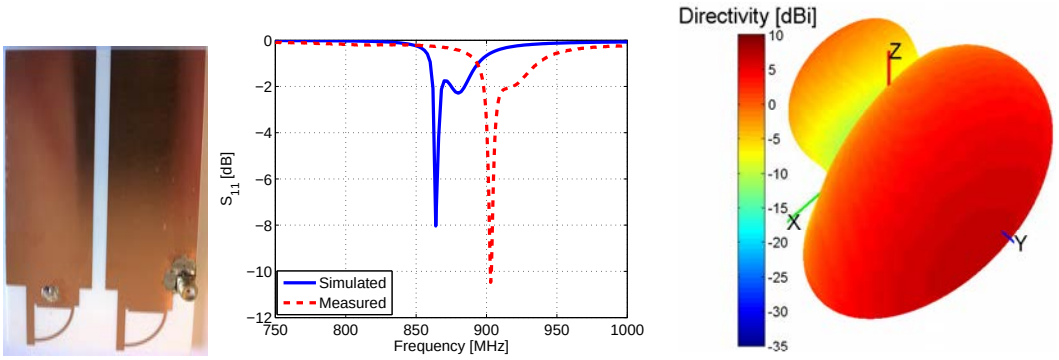

(a) (b) (c)

Figure 4.40: Two-element array mounted on a PCB. (a) A photograph of the prototype, (b) measured input reflection coefficient magnitude and (c) measured 3D total directivity radiation pattern.

The array measured 2D total directivity radiation patterns are given in Figure 4.41. The measured HPBW in horizontal and vertical planes are respectively 72° and 112° and the FBR is equal to $7.2dB$. This is in a very good agreement with the simulated results. The very small difference can be attributed to the SMD components, the coaxial cable radiation effect, and the measuring system and environment.

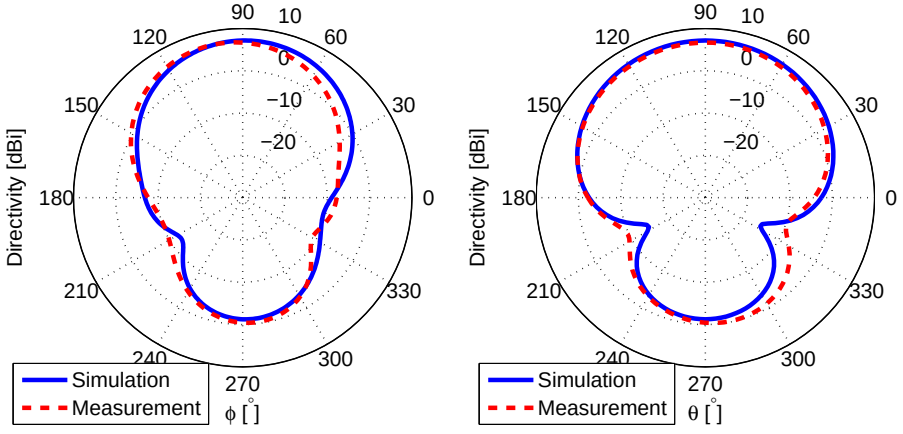

(a) (b)

Figure 4.41: Two-element array mounted on a PCB's measured 2D total directivity radiation patterns. (a) Horizontal plane and (b) vertical plane.

Figure 4.42(a) shows that the antenna measured total directivity is maximal at the measured resonance frequency. The antenna directivity bandwidth is around $8MHz$. The antenna efficiency was measured in a reverberation chamber with a tolerance of 15% (due to the incertitude in the reference antenna's efficiency) [63]. The antenna presents a measured radiation efficiency of about 70% (Figure 4.42(b)).

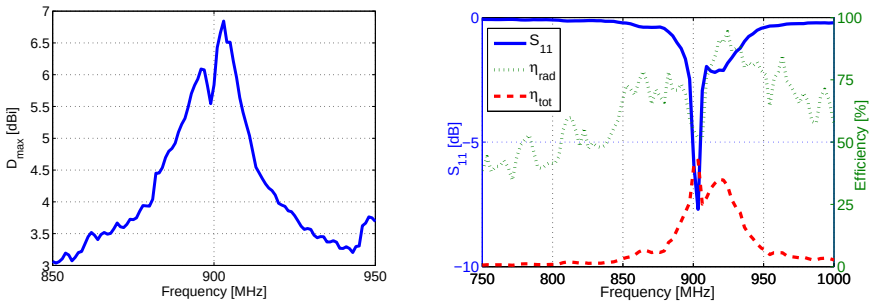

(a) (b)

Figure 4.42: Two-element array mounted on a PCB's measured parameters. (a) Maximum total directivity and (b) efficiency.

4.3.2.2.3 Three-Element Array on a PCB

In this array, three unit-elements similar to the previous array are used. Figure 4.43(a) shows the antenna geometry and dimensions. Figure 4.43(b) shows the input reflection coefficient magnitude of the three elements. Since the antenna geometry is similar to the previous scenario, the antenna resonance frequency is the same ($866MHz$). Hence, the array is designed for this frequency with a size factor ($ka = 1.4$).

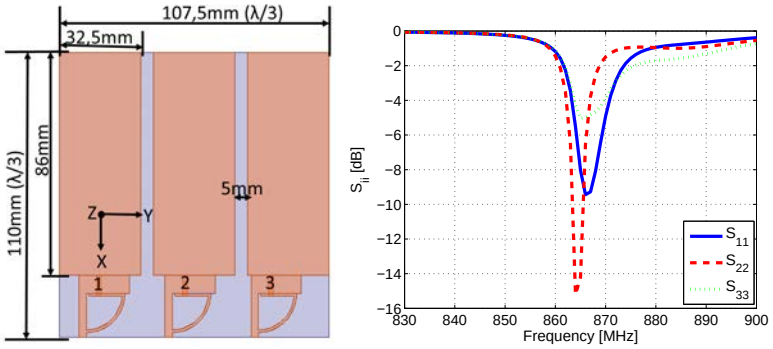

(a) (b)

Figure 4.43: Three-element array mounted on a PCB. (a) Geometry and dimensions and (b) simulated input reflection coefficient magnitude.

Exciting the second- and third-element with a current of $1.4e^{-j146^o}$ and $0.2e^{j69^o}$ relative the first one, a maximum total directivity of $9.5dBi$ is achieved. In the parasitic array, the first and third elements are respectively loaded with $68\Omega//4.5pF$ and $0.56pF$ and it achieves a maximum total directivity of $9.2dBi$. Figure 4.44 shows the 3D total directivity radiation patterns and Figure 4.45 shows 2D radiation patterns in horizontal and vertical planes. The figures show a good agreement between the two cases. For both case, the HPBWs in horizontal and vertical planes are respectively 60° and 72°. The fully-driven array's FBR is about $18.6dB$ while the parasitic array's one is about $16.9dB$.

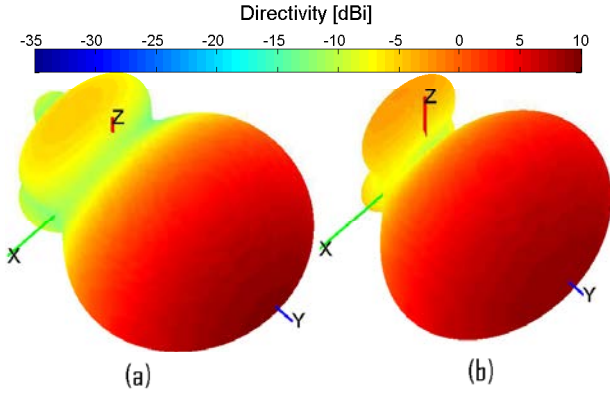

Figure 4.44: Three-element array mounted on a PCB's simulated 3D total directivity radiation pattern. (a) Fully-driven array and (b) parasitic one.

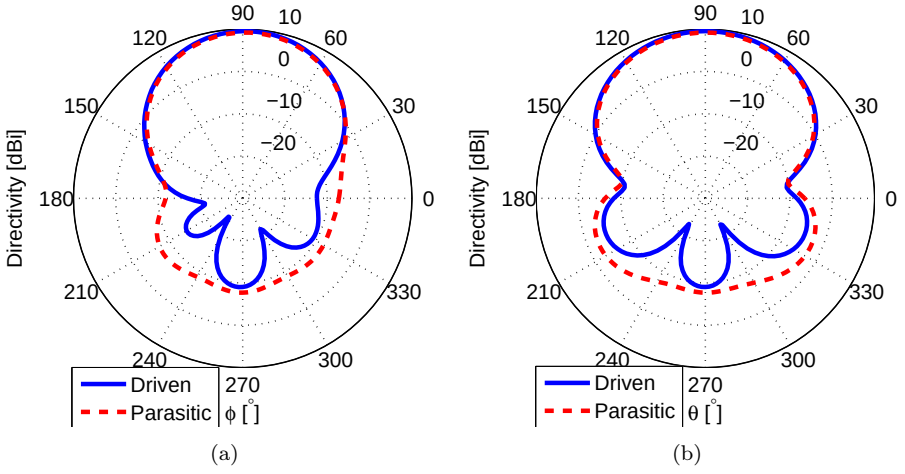

Figure 4.45: Three-element array mounted on a PCB's simulated 2D total directivity radiation patterns. (a) Horizontal plane and (b) vertical plane.

Figure 4.46 shows the same trend as in the two previous scenarios. The antenna has an impedance bandwidth of $2.8MHz$ and a directivity bandwidth of $2.6MHz$. Due to the increment in the mutual coupling, the antenna presents a radiation efficiency of 11.2%. This is the same trend that was shown with the dipole-based array, where increasing the number of elements from two to three reduces the radiation efficiency from around 100% to 22.6%.

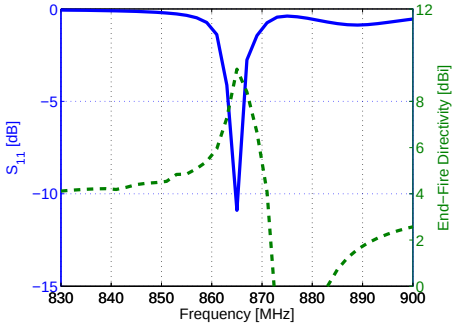

Figure 4.46: Parasitic three-element array mounted on a PCB's simulated input reflection coefficient magnitude and end-fire total directivity.

Figure 4.47 shows again a good agreement between the surface current distribution of the fully-driven and the parasitic array. Finally, this antenna is significantly smaller than a Yagi-Uda antenna covering the same frequency band and with the same directivity which dimensions are about $500 \times 152mm^2$ [110]. Moreover, this antenna is easier to integrate in the communications systems.

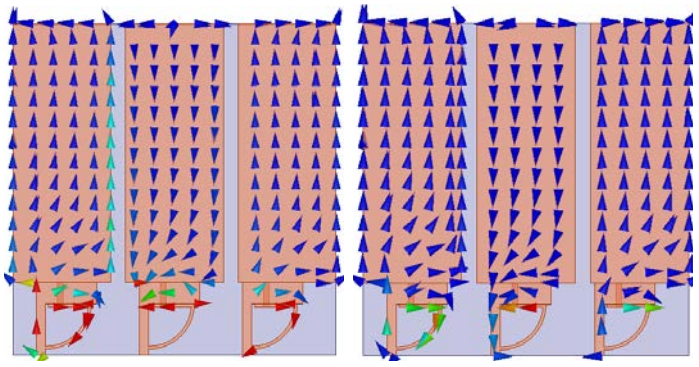

(a) (b)

Figure 4.47: Three-element array mounted on a PCB's simulated surface current distribution.(a) Fully-driven array and (b) parasitic one.

A prototype of this antenna was fabricated and measured for results validation. Figure 4.48(a) shows a photograph of the prototype. Figure 4.48(b) shows the antenna measured input reflection coefficient magnitude in dB. The measured resonance is $903MHz$ (4.7% shifted compared to the simulated one). This shift is mainly due to the coaxial cable effect and the dispersion of SMD components. Due to the antenna low efficiency, it is not easy to measure its far-field radiation pattern in the presence of a coaxial cable. Hence an optical probe from enprobe [111] was used and the measurements were performed in SATIMO stargate (SG 32) near-field measurement system. Figure 4.48(c) shows the measured 3D total directivity radiation pattern at the resonance frequency ($903MHz$). This pattern is in a good agreement with the simulated one. The measured directivity is $8.1dBi$.

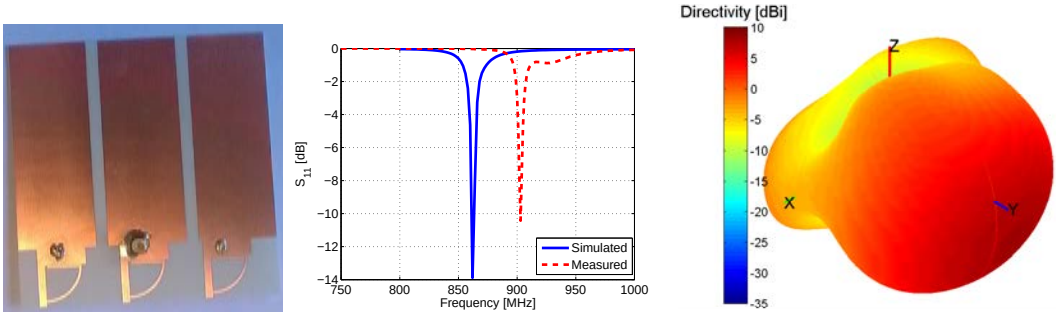

(a) (b) (c)

Figure 4.48: Three-element array mounted on a PCB's experimental results. (a) Fabricated prototype, (b) input reflection coefficient magnitude in dB and (c) 3D total directivity radiation pattern at the resonance frequency (903MHz).

Figure 4.49 shows measured 2D total directivity radiation patterns in horizontal and vertical planes. The HPBW in horizontal and vertical planes are respectively 67.5^o and 73^o and the FBR is $8.5dB$. The small difference may be attributed to the measuring system and environment as well as the dispersion of SMD components.

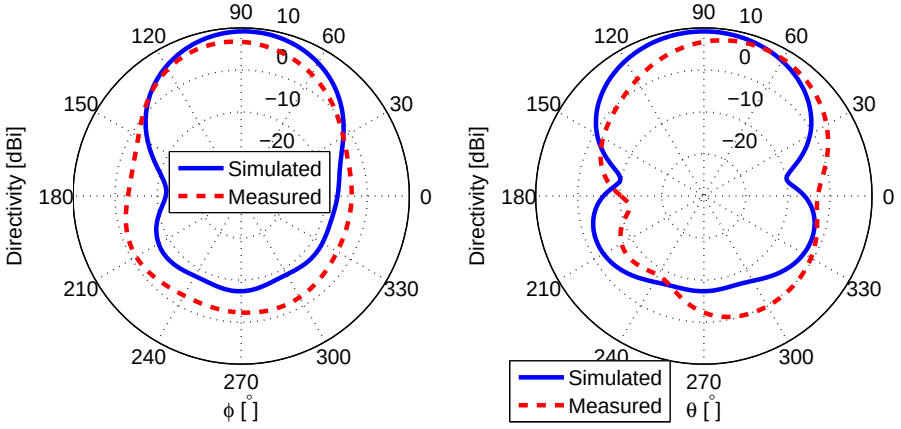

(a) (b)

Figure 4.49: Three-element array mounted on a PCB's measured 2D total directivity radiation patterns at the resonance frequency (903MHz). (a) Horizontal plane and (b) vertical plane.

4.3.2.3 Folded Monopole-Based Array

The unit element used here is a folded meandered monopole printed on a Rogers duroid/ RT5880 substrate ($\epsilon_r = 2.2, tan(\delta) = 0.0009$) with a thickness of $0.8mm$ (Figure 4.50(a)). Its size is $122 \times 31mm^2$. It has a simulated resonance frequency around $900MHz$ with a quasi-omnidirectional radiation pattern (a total directivity of $2.4dBi$ (Figure 4.50(b))) and a radiation efficiency of around 100%.

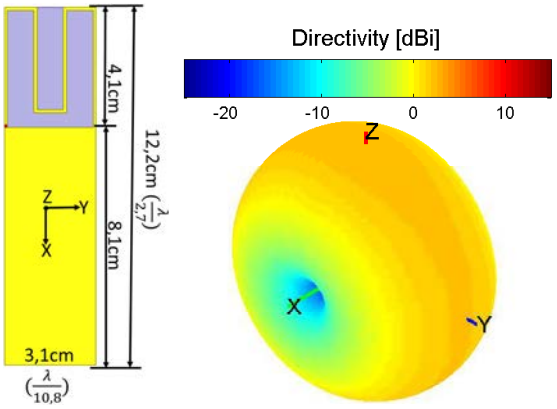

(a) (b)

Figure 4.50: The unit-element. (a) Geometry and dimensions and (b) simulated 3D total directivity radiation pattern.

We designed a four-element array for operating at $900MHz$ frequency band with an inter-element spacing is 0.2λ due to the trade off between the antenna-dimensions, -directivity and -radiation efficiency. The total size of the array is $231 \times 122mm^2(\frac{\lambda}{1.4} \times \frac{\lambda}{2.7})$. The fully-driven array current excitation coefficients and the equivalent optimal loads for transforming the array to a parasitic one are given in Table 1 (refer to Figure 4.51 for elements order). As it can be noticed some negative resistances are required, neglecting these resistances and loading the parasitic elements with the lumped elements given in Table 1, total directivities of 8.4, 11.6, 10.4 and 8.2dBi can be achieved in case of exciting the first, second, third or fourth element respectively. For example, when exciting the first element, the second, third and fourth are respectively loaded with $34.74pF$, $7.6pF$ and $61.2\Omega//77.5nH$. The significant decrement in the parasitic array directivity when exciting the first or fourth element is due to neglecting important negative resistances and the high sensitivity of the antenna directivity to the excitation coefficients as the number of elements increases. In analogy, the achieved directivity when exciting the second element is the highest due to the small values of the neglected resistances and since the coupling with the other elements is the highest. Figure 4.51 shows that the parasitic (when exciting the second element) array's simulated surface current distribution is in a very good agreement with the fully-driven array's one.

Table 4.3: The calculated excitation coefficients, the equivalent- and the applied- loads for four-element array.

Element	1	2	3	4
Excitation [A]	1	$2.26e^{j-154.8^o}$	$2.24e^{j45^o}$	$1.07e^{j-114.4^o}$
Optimal load [Ω]	$-4.79 + j40.37$	$-19.02 - j5.09$	$-j23.91$	$39.48 + j0.3$
Applied load	$12nH$	$34.74pF$	$7.6pF$	$61.2\Omega//77.5nH$

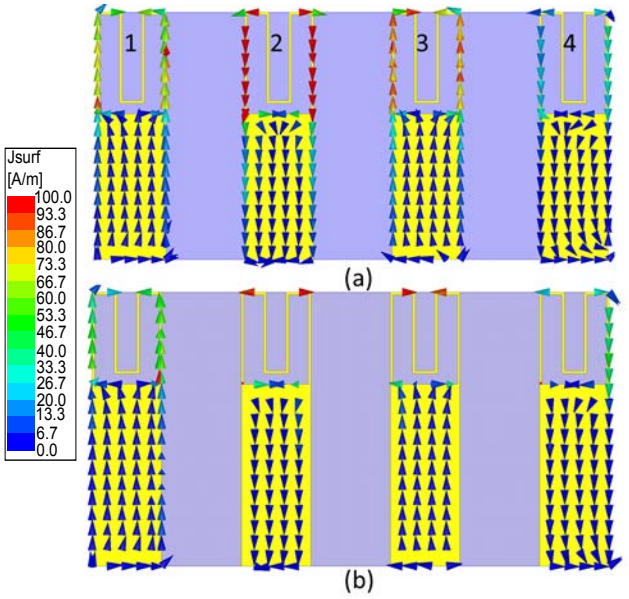

Figure 4.51: The surface current distribution in (a) fully-driven array and (b) parasitic array.

A prototype of this antenna was fabricated and measured to validate the results (Figure 4.52(a)). Figure 4.52(b) shows that the array measured input reflection coefficient is in a very good agreement with the simulated one. The simulated ($S_{11} < -10dB$) impedance bandwidth is around $7MHz$ while the measured one is $6MHz$. The antenna far-field radiation pattern was measured using SATIMO Stargate SG 32 measuring system. Figure 4.52(c) shows the array maximum total directivity as a function of the frequency. The figure shows that this directivity is highest at the the design frequency with a ($D_{max} - 1dB$) directivity bandwidth of $28.6MHz$ in simulation and $34MHz$ in measurement. Figure 4.52(d) shows the antenna radiation efficiency. It can be noticed that this efficiency rapidly decreases when approaching the design frequency. This is mainly due to the superdirectivity phenomena; where the current opposition on the different elements cancels the antenna radiation in certain directions, and hence, reduces its radiation efficiency.

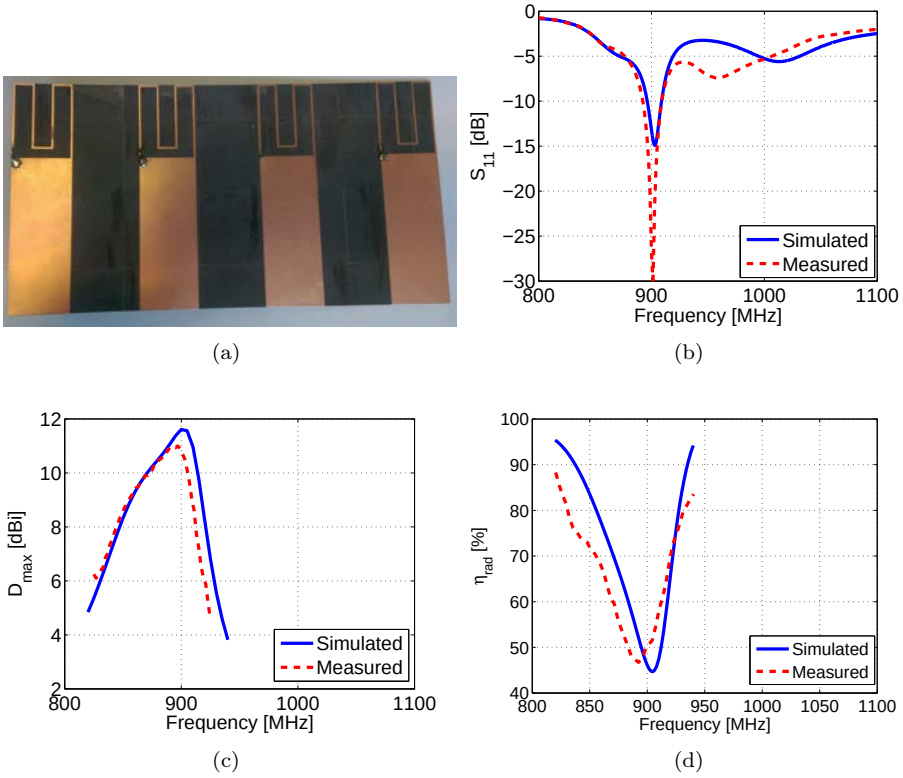

Figure 4.52: Parasitic array simulated and measured parameters. (a) A photograph of the realized prototype, (b) input reflection coefficient magnitude in dB, (c) maximum total directivity and (d) radiation efficiency.

It can be noted from Figure 4.53 that the parasitic array 3D total directivity radiation pattern is in a very good agreement with the fully-driven array's one. Concerning the parasitic array, the figure shows that the antenna is directive with a simulated directivity of $11.6dBi$ and a measured one of $11dBi$.

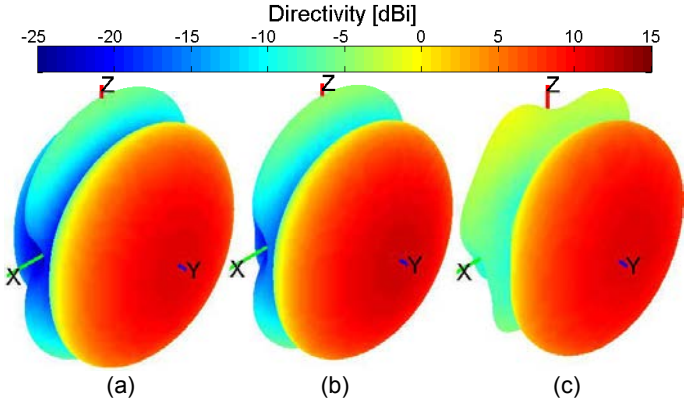

Figure 4.53: Proposed array 3D total directivity radiation pattern. (a) Simulated driven, (b) simulated parasitic and (c) measured parasitic.

The HPBW in horizontal (XoY) and vertical (YoZ) planes are respectively 48^o and 58^o in simulation and 45^o and 56^o in measurement. The simulated FBR is $18.3dB$ while the measured one is $13dB$ (Figure 4.54). The antenna has a simulated

radiation efficiency of 46% (a gain of $8.3dBi$) and an experimental one (measured in a reverberation chamber) of 47.3% (a gain of $8dBi$).

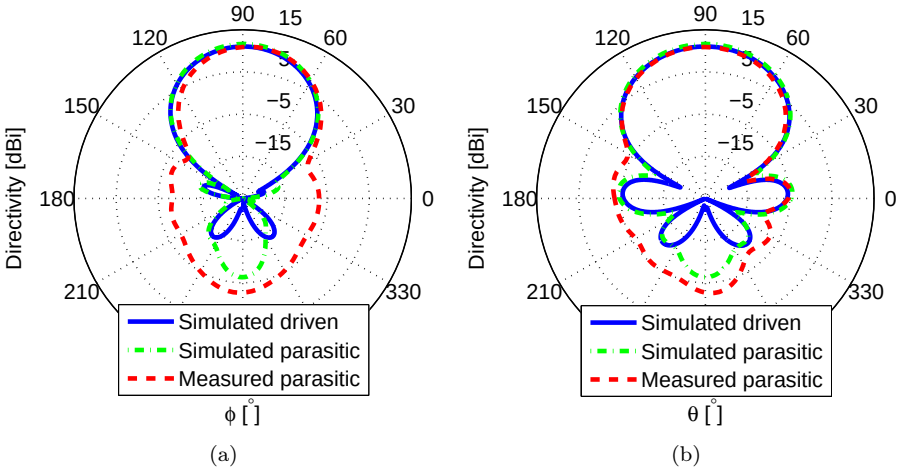

Figure 4.54: Proposed array simulated and measured 2D total directivity radiation pattern. (a) Horizontal plane and (b) vertical plane.

The antenna 3D co-polar directivity radiation pattern given in Figure 4.55 shows a very good agreement between the simulated and measured patterns. The maximum co-polar directivity is also in the end-fire (oY) direction with a simulated value of $11.6dBi$ and a measured one of $11dBi$.

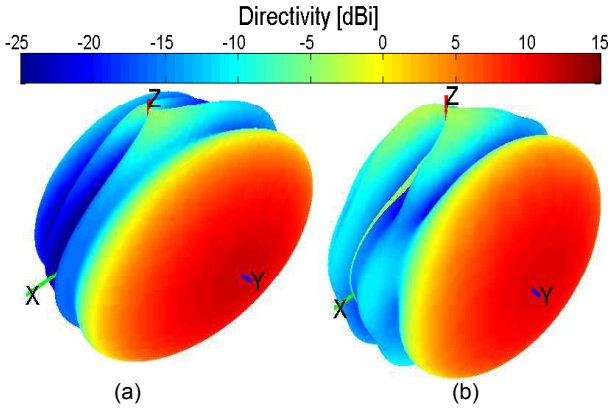

Figure 4.55: Parasitic array 3D co-polar directivity radiation pattern. (a) Simulated and (b) measured.

The antenna cross-polar 3D directivity radiation pattern is given in Figure 4.56. The maximum cross-polar directivity is in the broadside (oZ) direction and it has a simulated value of $-4.7dBi$ and a measured one of $-1.2dBi$. The small difference between simulated and measured results can be attributed to the cable effect, the uncertainties in the SMD components values and measuring system and environment. This antenna is very compact compared to others presenting the same directivity. A Yagi-Uda antenna with the same directivity is around $535 \times 175 \times 40mm^3$ [112].

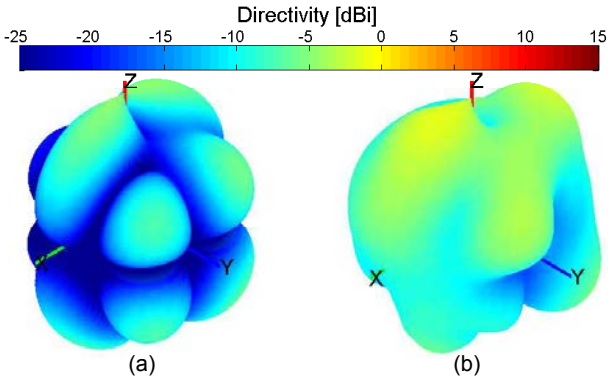

Figure 4.56: Parasitic array 3D cross-polar directivity radiation pattern. (a) Simulated and (b) measured.

It can be noticed that in all the designed antennas, the parasitic array's simulated total directivity radiation pattern was very close to the fully-driven array's one. the very small difference between the fully driven-array's radiation pattern and the parasitic one is due to neglecting a required small negative resistance. In the next section, we will study using parasitic arrays as unit-elements in compact 3D arrays.

4.4 Compact Antenna Array Based on Superdirective Elements

In this section, we investigate using parasitic (loaded) superdirective antennas as unit-elements to realize compact 3D broadside arrays. A parametric analysis on the inter-element distance demonstrates the necessary tradeoff between the antenna-dimensions, -directivity and -radiation efficiency. Although this work is based on two-element array, it can be generalized to N-element arrays.

4.4.1 3D Array Design

Four of the "two-element array on a PCB" using a loop end-fire antenna presented previously are arranged as shown in Figure 4.57(a) where the two antennas in the same plane are inverted to increase the distance between the radiating elements. Then, to achieve the maximum directivity in oY direction, this inversion is compensated by a 180^o phase shift in their excitation (elements 1 and 3 are excited out of phase comparing to elements 2 and 4). The separating distance (measured between the feeding points) is $152mm$ on x-axis and $200mm$ on z-axis. Hence, the array total dimensions are $200 \times 200 \times 70mm^3$. As it can be seen from the antenna simulated 3D total directivity radiation pattern given in Figure 4.57(b), the antenna has a directive pattern with a maximum total directivity of $11.4dBi$. The HPBW in horizontal and vertical planes are respectively $56°$ and $48°$, and the FBR is $13.2dB$. The radiation pattern has four side lobes with a Side Lobe Level (SLL) of $-8.3dBi$.

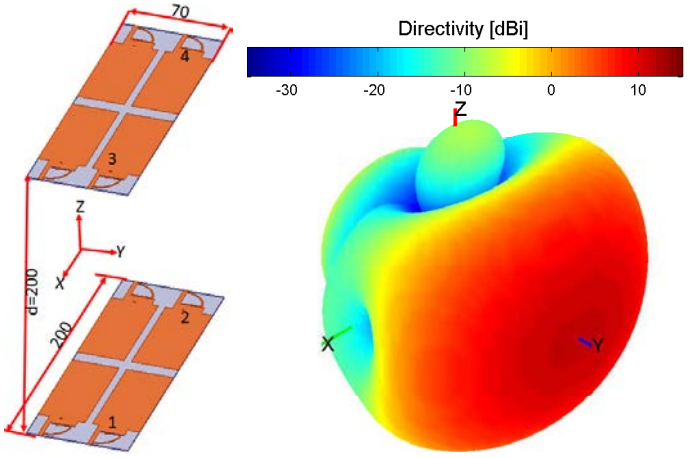

(a) (b)

Figure 4.57: Broadside array geometry and simulated parameters. (a) Geometry and dimensions, and (b) 3D total directivity radiation pattern.

Figure 4.58(a) shows that antenna's broadside total directivity ($D_{(\theta=90^o,\phi=90^o)}$) is maximal around the resonance frequency of $869MHz$ (the input reflection coefficient of the four elements are identical so only one is shown). The antenna has an impedance bandwidth of $1MHz$ and a directivity one of $8.7MHz$. Comparing with the end-fire array, it can be noticed that the array maximum total directivity is increased by $4.4dBi$, the horizontal HPBW is divided by 1.4, and vertical HPBW is divided by 2.3. The limited improvement in horizontal HPBW is due to the smaller separation in this plane, and hence, a higher mutual coupling as it can be seen in Figure 4.58(b).

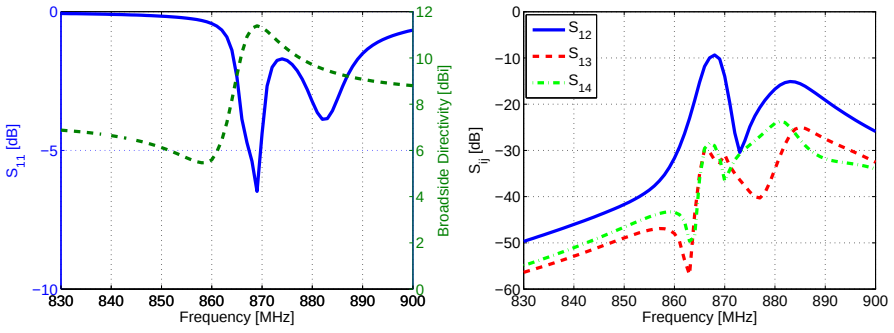

(a) (b)

Figure 4.58: Broadside array simulated parameters. (a) input reflection coefficient magnitude in dB and broadside directivity and (b) mutual coupling magnitude in dB.

4.4.1.1 Distance Effect

We vary the array distance (d) from 0.01λ to λ while monitoring the antenna input reflection coefficient, total directivity and radiation efficiency. Figure 4.59(a) shows the array simulated input reflection coefficient magnitude in dB as a function of the distance. The figure shows that for $d = 0.01\lambda$ the array is completely unmatched in the observed frequency band. This is due to the high mutual coupling. As the

distance increases the mutual coupling decreases and the array resonance frequency converges to the one of the unit-elements. Figure 4.59(b) shows the array simulated maximum total directivity and radiation efficiency as a function of the distance. For very small distances, due to the high mutual coupling, the applied loads are not suitable anymore and superdirectivity effect is lost, and hence, the radiation efficiency is maximal. As the distance increases, the superdirectivity effect appears and the radiation efficiency decreases. As expected, we can note that as the distance increases, the achieved directivity increases till 0.7λ when it starts decreasing again [66].

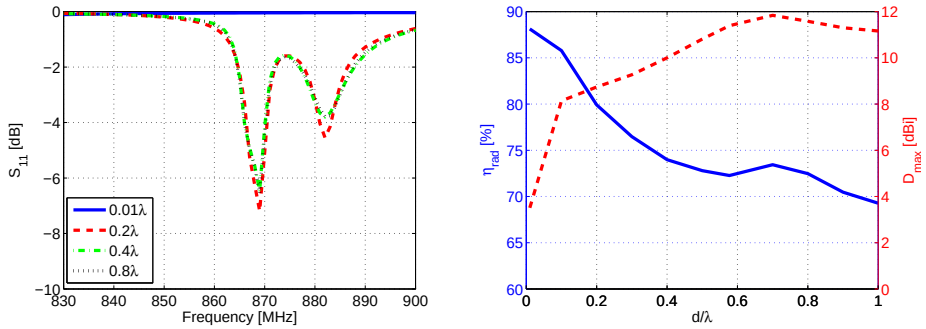

(a) (b)

Figure 4.59: Broadside array simulated parameters as a function of the distance. (a) Input reflection coefficient magnitude in dB and (b) total directivity and radiation efficiency.

Figure 4.60 shows array 2D total directivity radiation patterns in horizontal and vertical planes at the design frequency ($869MHz$) for several distances. For distances greater than 0.5λ side lobes appear in the vertical plane and as the distance increases the SLL also increases, where increasing the distance from 0.5λ to λ increases the SLL from $-12.8dBi$ to $6.7dBi$. We chose to realize the antenna with $d = 0.6\lambda$ due to a constraint on the antenna dimensions.

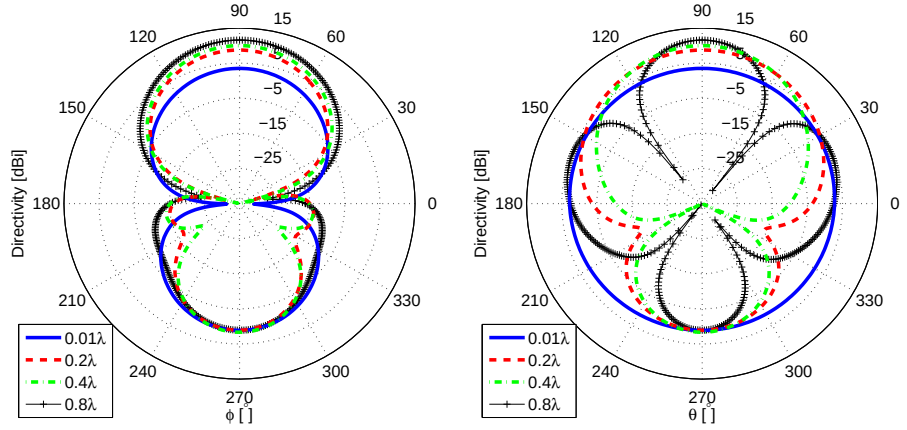

(a) (b)

Figure 4.60: Broadside array simulated 2D total directivity radiation patterns as a function of the distance. (a) Horizontal plane and (b) vertical plane.

4.4.2 Measurement Results

Figure 4.61(a) shows a photograph of the realized prototype of the broadside array. The feeding system is composed of one ZFSCJ-2-4+ power splitter [113], two ZX10-2-20+ power splitter-shifter [114] and four $30cm$-long UFL cables [115]. The antenna far-field radiation pattern was measured in SATIMO stargate (SG 32) near-field measurement system. The measured 3D total directivity radiation pattern at the resonance frequency is given in Figure 4.61(b). The figure shows a maximum total directivity of $11.3dBi$ in the broadside direction (towards oY). Figure 4.61(c) shows measured input reflection coefficient magnitude for the unit-elements and the antenna with the feeding system as well as the maximum total directivity versus frequency. The measured resonance frequency of the unit-elements is around $883MHz$ (a frequency shift of 1.8%). This shift is probably due to the antenna environment (UFL cable effect, SMA connector and the dispersion of the commercial SMD loads). We can note that the feeding system presents an approximate insertion loss of $3.5dB$ at the resonance frequency. This loss is distributed as follows: $1.5dB$ in the splitter, $0.6dB$ in the splitter-shifter, $1dB$ in the UFL cable and $0.4dB$ in the connectors. The antenna (without the feeding system) has an impedance bandwidth of $1.9MHz$. The figure also shows that the antenna directivity is maximal around the resonance frequency with a directivity bandwidth of $13.5MHz$.

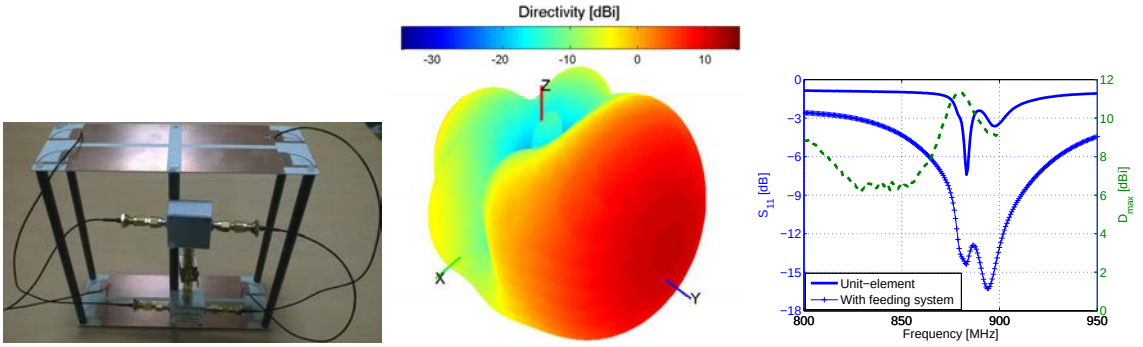

(a) (b) (c)

Figure 4.61: Broadside array prototype and measured results. (a) Fabricated prototype, (b) 3D total directivity radiation pattern and (c) input reflection coefficient magnitude in dB and maximum total directivity.

Figure 4.62(a) and Figure 4.62(b) show measured 2D total directivity radiation patterns. The HPBW in both horizontal and vertical planes are 56°, the FBR is $12.4dB$ and SLL is $-2.6dBi$. The measured pattern is in a very good agreement with the simulated one in the main-beam direction. The small difference in the backward direction may be attributed to the measuring system and environment. The antenna radiation efficiency measured in a reverberation chamber, after compensating the losses in the feeding system, is about 58%, and hence. the antenna measured gain is $8.9dBi$.

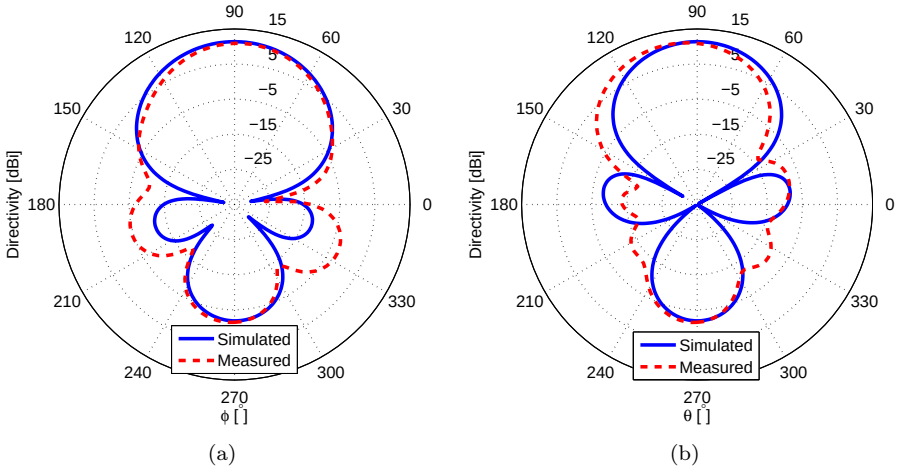

Figure 4.62: Broadside array measured 2D total directivity radiation pattern.(a) Horizontal plane and (b) vertical plane.

In this section, a compact 3D antenna array based on superdirective elements was designed. In order to increase the array efficiency, the inter-element distance should be increased. Consequently, the design of this kind of arrays is also a trade-off between its dimensions, directivity and efficiency. In the next section we will study the problem of designing compact planar antenna arrays for UHF band by using small superdirective unit-elements.

4.5 Planar Arrays Design

In this section, we propose a new strategy for designing compact planar arrays by using small superdirective arrays as unit-elements. The constraints including the maximum directivity, the efficiency, the predefined number of elements and the distance between the elements are studied. Results are validated through the realization and measurement of a 2×2 array.

4.5.1 Unit-Element Description

The initial antenna used in the designed array is a miniaturized half-loop antenna printed on a 0.8mm-thick Rogers RO4003 substrate and integrated in a PCB of $8 \times 8cm^2$ as shown in Figure 4.63(a). It has a simulated resonance around $864MHz$ as shown in Figure 4.63(c). Figure 4.63(d) shows the antenna surface current distribution (the same color range will be used from now on). As it can be noticed, the current on the ground plane is mainly following oY direction, hence, it acts as a monopole in the XoY plane and following the Y-axis. This explains the omnidirectional radiation in the XoZ direction and the null in the oY direction in the antenna far-field radiation pattern given in Figure 4.63(e). The null is slightly rotated toward X-axis due to the edges radiation. The antenna has a directivity of $2.4dBi$ and radiation efficiency of 89.4%. A prototype of the antenna was fabricated and measured for results validation (Figure 4.63(b)). Figure 4.63(c) shows the measured input reflection coefficient magnitude in dB. The measured resonance is at $881MHz$ (a shift of 2% compared to the simulation). The antenna far field radiation pattern was measured in SATIMO Stargate SG 32 near field measurement system. The

measured 3D total directivity radiation pattern at the resonance is given in Figure 4.63(e). The measured directivity is $3.1dBi$.

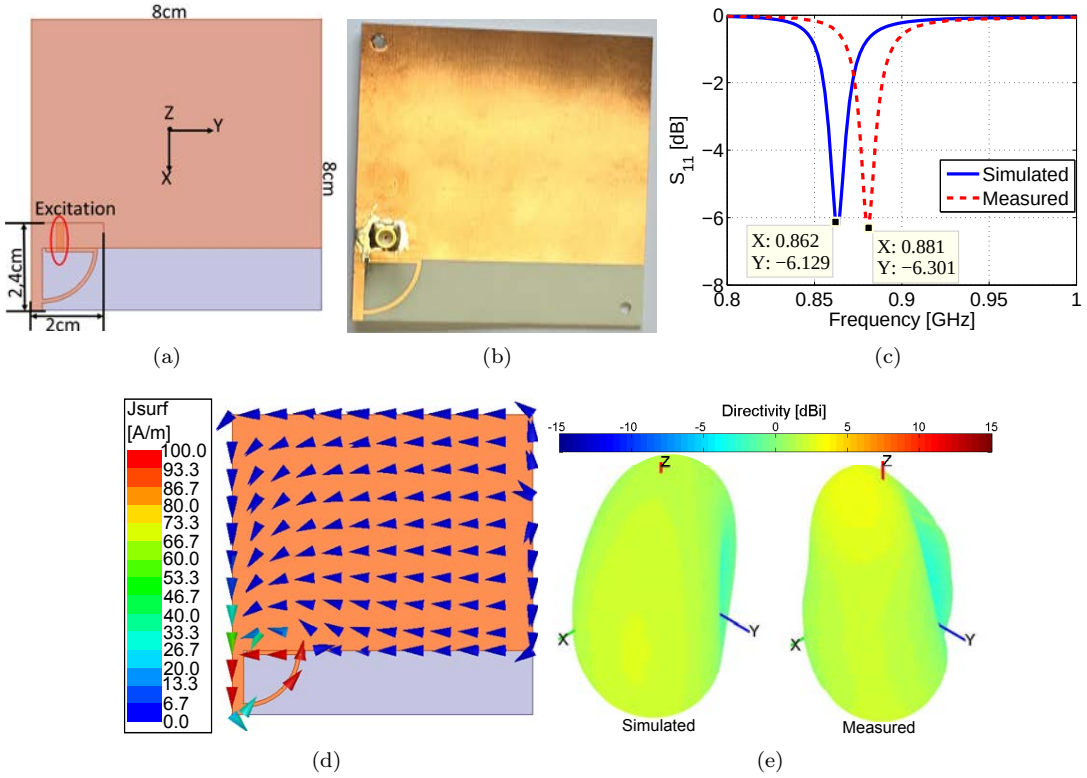

Figure 4.63: The unit-element simulated and measured parameters. (a) Geometry and dimensions, (b) fabricated prototype, (c) input reflection coefficient magnitude in dB, (d) surface current distribution and (e) 3D total directivity radiation pattern.

For more insight the antenna 2D total directivity radiation patterns in E (XoZ) and H (YoZ) planes are given in Figure 4.64. The antenna radiation efficiency measured in a reverberation chamber is about 75%.

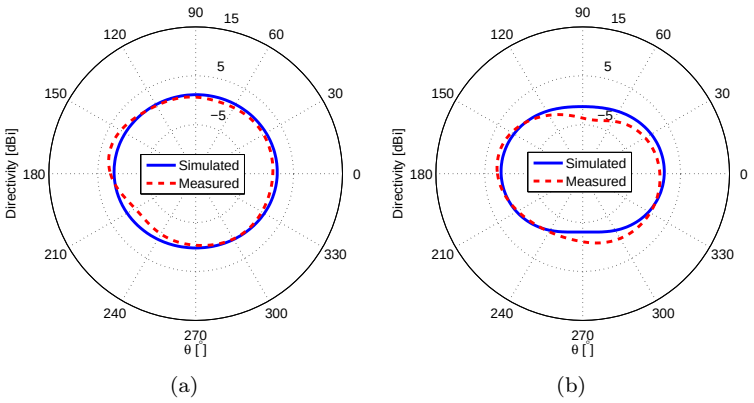

Figure 4.64: The unit-element simulated and measured 2D total directivity radiation pattern. (a) E plane and (b) H plane.

4.5.2 Parasitic Superdirective Unit-Element Design

Two elements of the above-mentioned antenna are stacked along Z-axis with an inter-element distance d_1 is varying from $0.69cm$ to $6cm$. Figure 4.65(a) shows the effect of the inter-element distance on the resonance frequency. We note that for very small distances, the resonance is shifted to $910MHz$ and as the distance increases this resonance converges to the one of the unit-element. Figures 4.65(b) and 4.65(c) show the value of the required loads for transforming the array to a parasitic one. It can be noticed that till $d_1 = 2.8cm$ only one negative resistance is required. Figure 4.65(d) shows the array directivity as a function of the distance. We observe that the driven array directivity is maximal for small distances and as the distance increases this directivity decreases. The parasitic (loaded) array directivity is close to the fully-driven one till $2.8cm$ where a negative resistance is required and neglecting this resistance significantly decreases the array directivity. Nevertheless, this directivity is still superior to Harrington's limit up to a distance of $5.5cm$. As for the array efficiency, it increases as the distance increases (Figure 4.65(e)). This is due to the decrement in the mutual coupling and the disturbance in the superdirectivity phenomena.

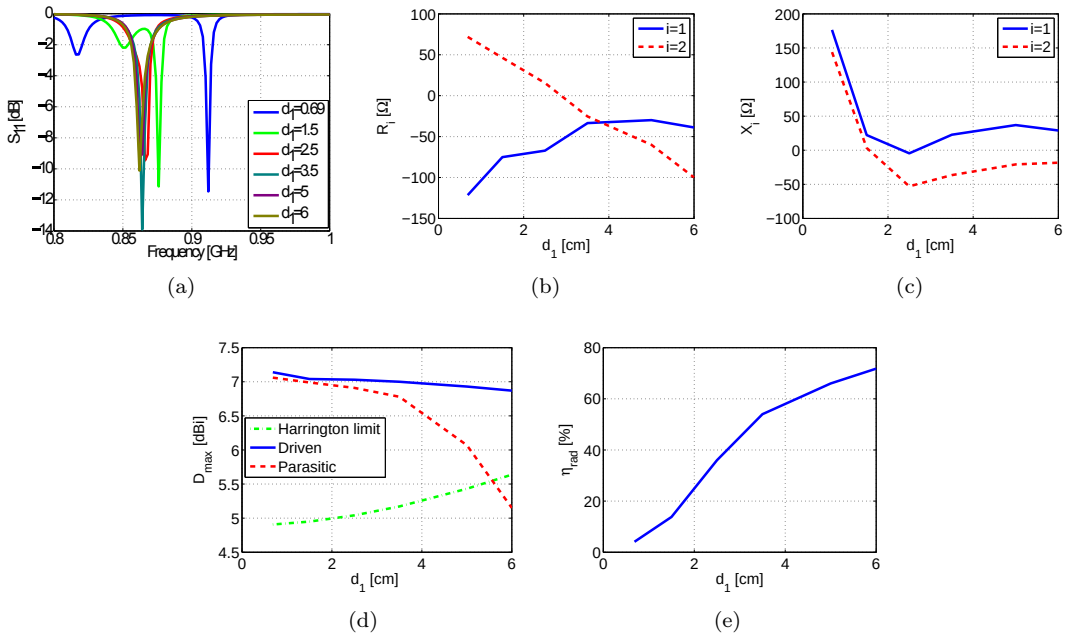

Figure 4.65: Parasitic two-element array parameters as a function of the inter-element distance. (a) Simulated input reflection coefficient magnitude in dB, (b) required resistance, (c) required reactance, (d) obtained total directivity, and (e) obtained radiation efficiency.

Based on this study and as compromise between the antenna- directivity and efficiency, we optimized a two-element array for $868MHz$ European RFID frequency band with an inter-element distance of $2.5cm(0.07\lambda)$ as shown in Figure 4.66(a). In this array, the first element is excited while the second is loaded by $3.3pF$. Figure 4.66(c) shows the antenna simulated input reflection coefficient magnitude in dB. As it can be noticed, the antenna has a resonance at $868MHz$. Figure 4.66(d) shows the antenna surface current distribution. The figure shows that the current on the two elements is out of phase which is the condition for having superdirectivity for very

small inter-element distance. Figure 4.66(e) shows the antenna 3D total directivity radiation pattern. The figure demonstrates a directive pattern with a directivity of $7dBi$ toward z-axis. This directivity is $1.9dB$ greater than Harrington's limit for an antenna with the same size factor ($ka = 1.1$). The HPBW in E (XoZ) and H (YoZ) planes are respectively 100^o and 86^o and FBR is $8.2dB$. Due to the current opposition, the antenna presents a radiation efficiency of 43.4%. A prototype of the antenna was fabricated and measured (Figure 4.66(b)). Figure 4.66(c) shows the antenna measured input reflection coefficient magnitude in dB. The measured resonance is at $880MHz$ (a shift of 1.4% compared to the simulation). The antenna measured 3D total directivity radiation pattern at the resonance is given in Figure 4.66(e). The measured directivity is $6.5dBi$. The HPBW in E and H planes are respectively 95.6^o and 84^o and FBR is $6.7dB$ (Figure 4.67). The antenna radiation efficiency measured in a reverberation chamber is about 40%.

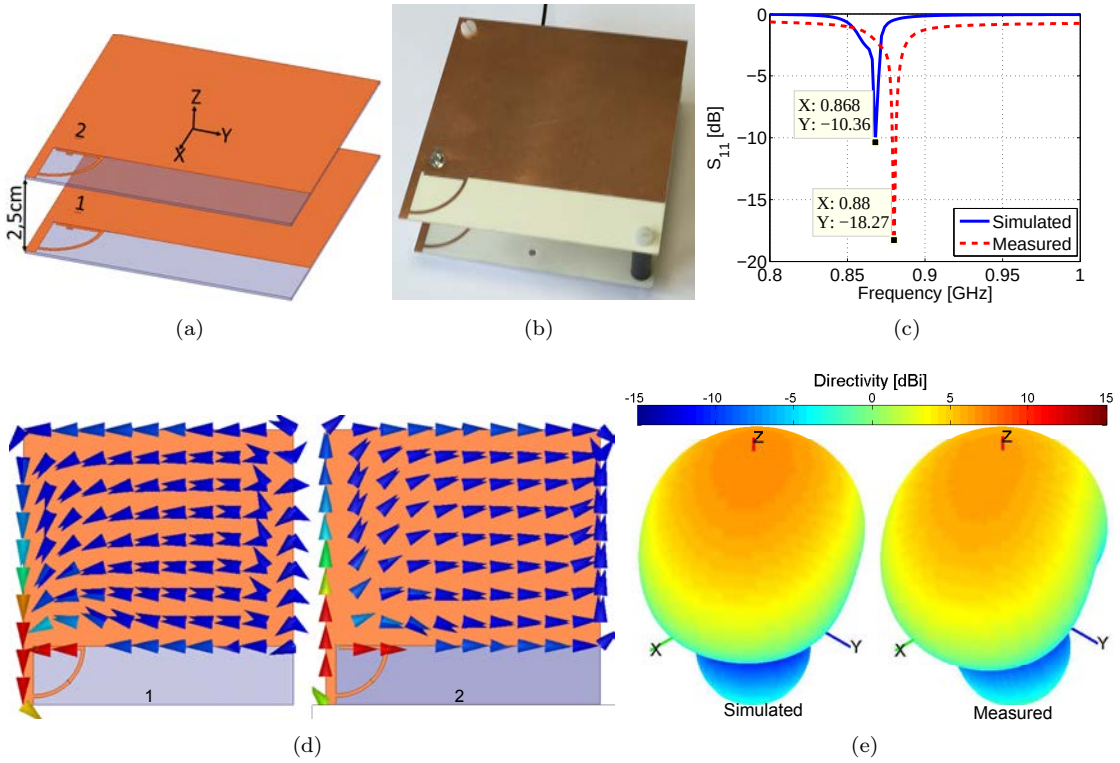

(a) (b) (c)

(d) (e)

Figure 4.66: Two-element array with 2.5cm spacing simulated and measured parameters. (a) Geometry and dimensions, (b) fabricated prototype, (c) input reflection coefficient magnitude in dB, (d) surface current distribution and (e) 3D total directivity radiation pattern.

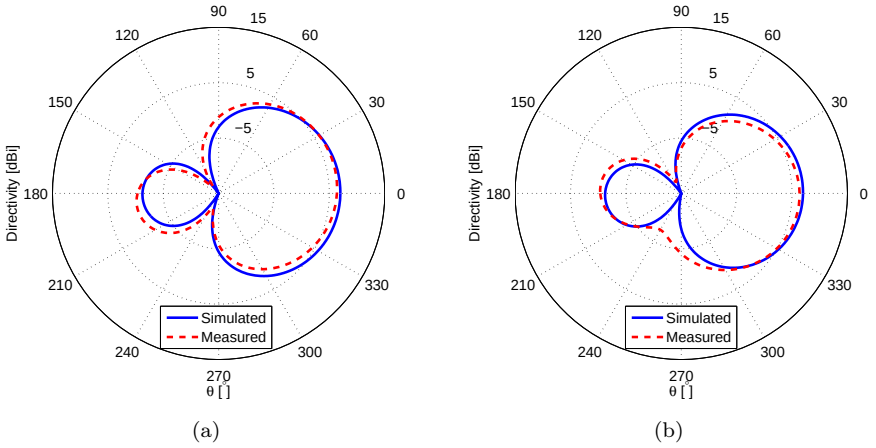

Figure 4.67: Two-element array with 2.5cm spacing simulated and measured 2D total directivity radiation pattern. (a) E plane and (b) H plane.

4.5.3 Planar Array Design

Four elements of the precedent parasitic array are integrated in 2×2 planar array as shown in Figure 4.68(a). The spacing between the elements d (calculated between the excitation ports) is changed from $12cm$ to $30cm$. Figure 4.68(c) shows the mutual coupling as a function of the distance. As expected, the figure shows a higher coupling for small separations and as the distance increases the coupling decreases. Figure 4.68(e) shows the antenna maximum directivity as a function of the distance. As the distance increases the coupling effect decreases and the achieved directivity increases till it reaches its maximum value around 0.8λ where it starts decreasing again. As for the antenna efficiency, as the distance increases it decrease (Figure 4.68(f)). This is mainly due to the lost of the superdirectivity for small distances (superdirectivity is achieved by a current opposition on the two unit-elements (Figure 4.66(d)) which cancels the antenna radiation in some directions and hence reduces its efficiency). This directivity approaches the best Harrington limit for a distance of 0.63λ. Finally, Figure 4.69 shows the 3D total directivity radiation pattern for a distance of $26cm \approx 0.75\lambda$. The achieved directivity is $12.6dBi$, and the radiation efficiency is 41%. The HPBW in E (XoZ) and H (YoZ) planes are respectively 37^o and 35^o and FBR is $8.9dB$ and the SLL is $3.2dB$. A prototype of the antenna was fabricated and measured (Figure 4.68(b)). A power divider from Mini-Circuits [116] and UFL cables are used for the feeding system. Figure 4.68(d) shows the antenna with the feeding system measured input reflection coefficient magnitude in dB. As it can be noticed, the resonance frequency is always at $879MHz$. It can also be noticed that the feeding system introduces a loss of about $1.5dB$. This loss is due to the UFL cable, the power divider and the coaxial connections. The antenna directivity given in Figure 4.68(e) shows the same trend as in the simulation.

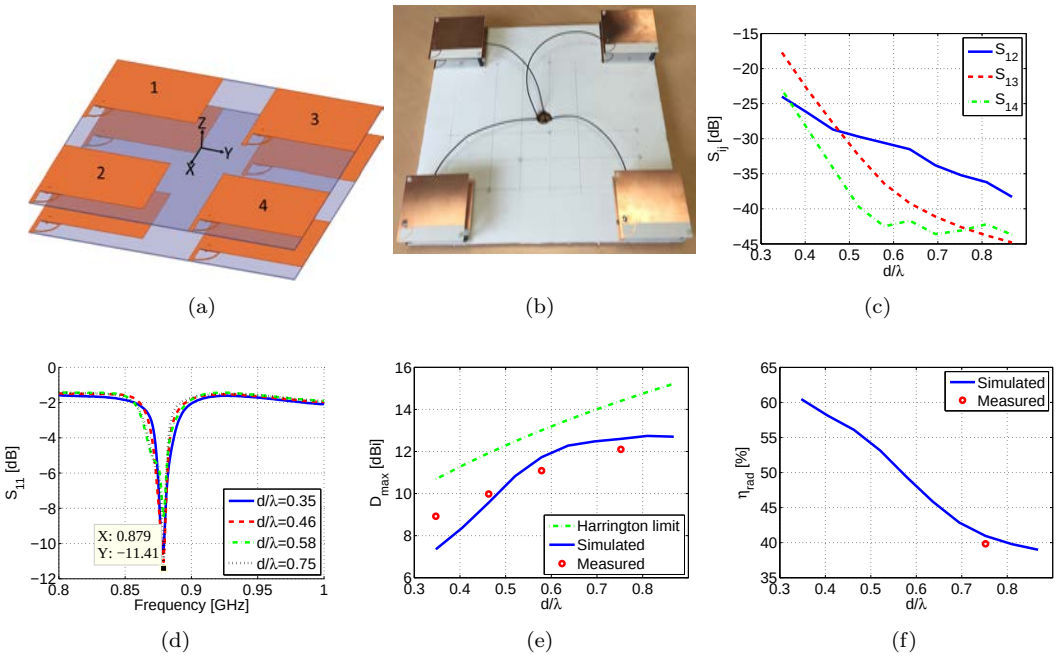

Figure 4.68: Planar array simulated and measured parameters as a function of the separation. (a) Geometry, (b) fabricated prototype, (c) mutual coupling, (d) input reflection coefficient magnitude in dB, (e) total directivity and (f) radiation efficiency.

The antenna measured 3D total directivity for a distance of $26cm$ is in a good agreement with the simulated one (Figure 4.69). The measured directivity is $12.1dBi$. The HPBW in E and H planes are respectively 39.4^o and 33.8^o and FBR is $18.8dB$ (Figure 4.70). The antenna reveals a measured radiation efficiency (also in a reverberation chamber) of about 39.8% after compensating the losses in the feeding system. In all cases, the small difference between the simulated and measured results is due to the measurement environment (the connector, the excitation cable, ..), the measurement incertitude and the tolerance on the reference antennas' parameters namely directivity for radiation pattern measurement and radiation efficiency in the efficiency measurement.

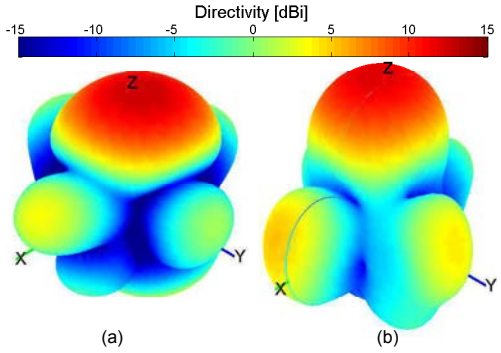

Figure 4.69: Planar array 3D total directivity radiation pattern for d=26cm. (a) Simulated and (b) measured.

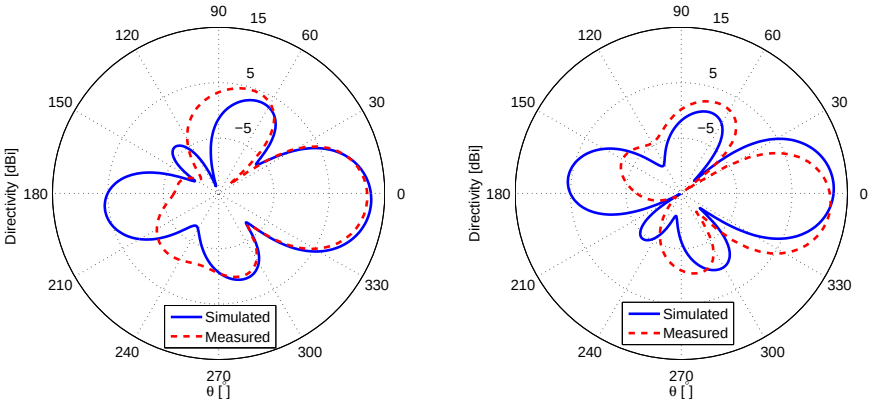

Figure 4.70: Planar array 2D total directivity radiation pattern for d=26cm. (a) E plane and (b) H plane.

In this section, a two-element superdirective array was designed and integrated in a 2×2 planar array. A parametric analysis on the inter-element distance revealed the tradeoffs between the antenna dimensions, directivity and efficiency. For an inter-element distance of $26cm$ and for total dimensions of $34 \times 34cm^2$ a total directivity of $12.6dBi$ and radiation efficiency of 41% were achieved. This antenna is significantly smaller than classic arrays with the same directivity. The generalization of this method to N-element superdirective arrays is studied in Annex 1. This array properly feeded can achieve a Circular Polarization (CP). This aspect will be investigated in the next section.

4.6 CP Array Based on Superdirective Unit-Elements

In this section, the design of a compact planar CP array based on parasitic superdirective unit-elements is investigated. Four elements of the parasitic array presented in the previous section are integrated in 2×2 planar array for $866MHz$ band as shown in Figure 4.71(a). The four elements are excited with phases of 0, 90^o, 180^o and 270^o to achieve a Left-Hand Circular Polarization (LHCP). The spacing between the elements d (calculated as a straight line between the excitation ports as shown in Figure 4.71(a)) is changed from $10.1cm$ to $27.6cm$. Figure 4.71(b) shows the antenna LHCP directivity and the efficiency as a function of the distance. It can be noticed that as the distance increases the coupling effect decreases and the achieved directivity increases till it reaches its maximum value around 0.5λ where it starts decreasing again. As for the antenna efficiency, as the distance increases it decreases and it reaches its minimum when the maximum directivity occurs. Figure 4.71(c) shows the antenna HPBW and CP aperture for an Axial Ratio (AR) $< 3dB$. As it can be noticed, CP aperture is always higher than the the HPBW. Moreover, AR is lower than $1dB$ in the entire HPBW.

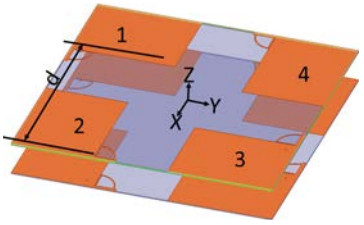

(a)

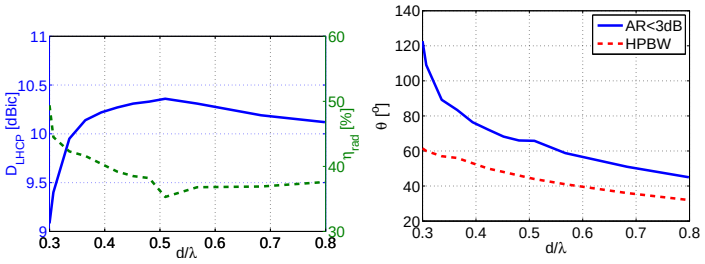

(b) (c)

Figure 4.71: Planar CP array simulated parameters as a function of the separation. (a) Geometry, (b) LHCP directivity and radiation efficiency and (c) HPBW and CP aperture.

A prototype of the antenna was fabricated and measured for a distance of $15.6cm \approx 0.45\lambda$ (Figure 4.72(a)). Two ZX10-2-20+ power dividers $(0, 180^o)$ [114], a hybrid coupler $(0, 90^o)$ from KDI/triangle [117], and four $30cm$-long UFL cables [115] are used for the feeding system. Figure 4.72(b) shows the antenna input reflection coefficient magnitude in dB. The antenna has a simulated/measured resonance frequency of $866/879.8MHz$ (a frequency shift of 1.6%). The antenna with the feeding system is well matched in all the observed frequency band. This is mainly due to the losses in the feeding system. The antenna measured LHCP directivity given in Figure 4.72(c) shows it increases till it reaches its maximum value of $10dBic$ at the resonance frequency then it starts decreasing again. The measured AR is also minimal around the resonance frequency. The antenna has a measured CP bandwidth ($AR < 3dB$) of $21MHz$.

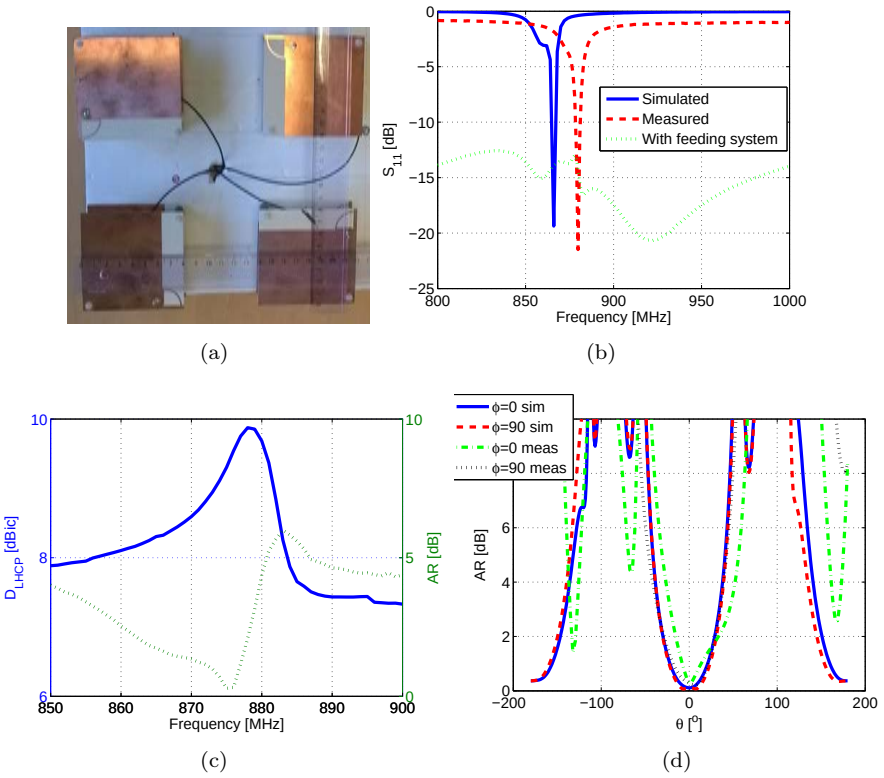

Figure 4.72: Planar CP array with $d = 15.6cm$. (a) Fabricated prototype, (b) input reflection coefficient magnitude in dB, (c) measured LHCP directivity and AR as a function of the frequency and (d) AR.

Figure 4.73(a) shows the antenna 3D LHCP directivity radiation pattern. It can be observed that the measured result is in a good agreement with the simulated one. The antenna has a simulated/ measured directivity of $10.3/10dBic$ in broadside direction (oZ). The antenna cross-polar (RHCP) 3D directivity radiation pattern is given in Figure 4.73(b). The measured result is in acceptable agreement with the simulated one.

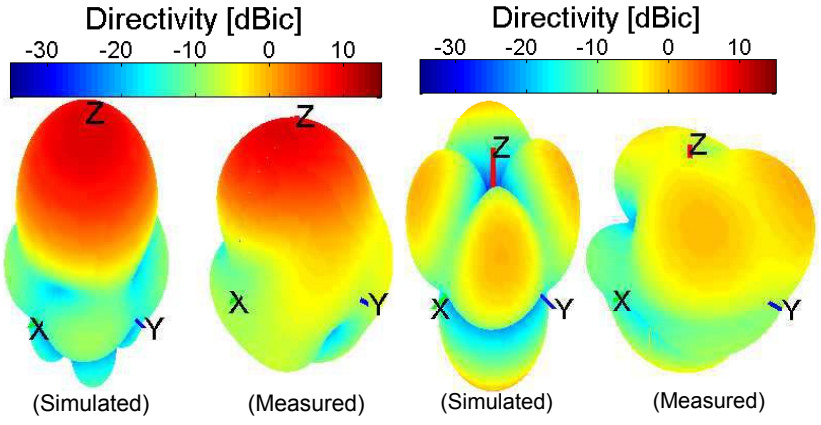

Figure 4.73: Planar CP array 3D directivity radiation pattern for d=15.6cm. (a) Co-polar and (b) cross-polar.

The antenna 2D main- and cross-polar -directivity radiation patterns are given in Figure 4.74. It can be noticed that the measured results in the main-polar are in a good agreement with the simulated ones. The simulated/ measured HPBW in E (XoZ) and H (YoZ) planes are respectively $48/45^o$ and $40.3/50.6^o$ and FBR is $40.3/19.8dB$. The small difference in the cross-polar levels is mainly due to the measurement environment (the feeding system and the support). The antenna has a simulated radiation efficiency of 38.5% and reveals a measured one of about 40% after compensating the losses in the feeding system.

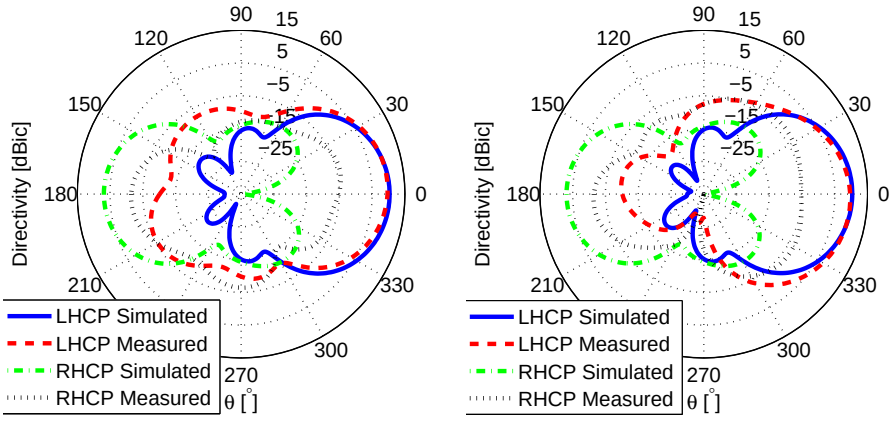

Figure 4.74: Planar CP array 2D LHCP and RHCP directivity radiation pattern for d=15.6cm. (a) E plane and (b) H plane.

4.7 Conclusion

In this chapter, a design approach for parasitic superdirective antenna arrays was presented. A parametric analysis on dipole-based arrays was performed to investigate the practical limitations. The method was later used to design multiple superdirective ESA-based arrays surpassing Harrington's limit on antenna directivity as in Figure 4.75. Then, the integration of superdirective ESAs in PCBs was investigated via different scenarios. Next, measuring superdirective ESAs integrated in PCBs was investigated via different feeding configurations. Later, a new strategy was presented to obtain a 3D small-size broadside array using compact end-fire unit-elements for UHF band. Although this work was based on a two-element array, it can be generalized on N-element arrays while keeping in mind the tradeoff between the array- dimensions, -directivity and -radiation efficiency. Afterward, a two-element parasitic superdirective antenna array was designed and integrated in a compact 2×2 planar antenna array. Finally, a compact CP planar array for $866MHz$ band based on superdirective arrays was presented. A summary of all the designed antennas is given in Table 4.4.

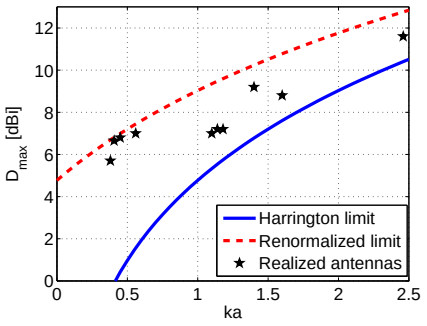

Figure 4.75: The obtained directivity of different designed antennas.

Table 4.4: A summary of all the designed antennas.

Antenna	ka	$D_{max}[dBi]$	$\eta_{rad}[\%]$	$G_{max}[dBi]$	Prototype
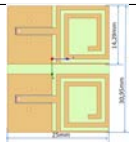	0.38	5.7	0.8	−5.27	
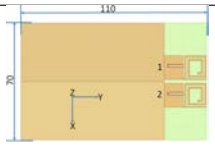	1.14	7.2	12.7	−1.76	
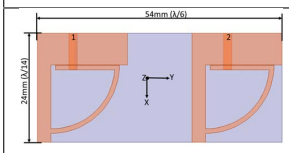	0.56	7	7.1	−4.49	
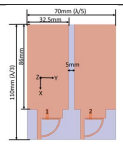	1.18	7.2	62	5.12	
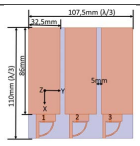	1.4	9.2	11.2	−0.31	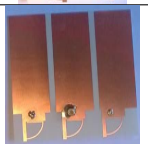
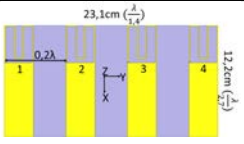	2.46	11.6	46	8.23	
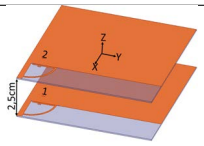	1.05	7	43.4	3.37	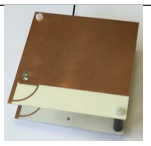
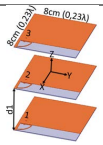	1.6	8.8	34.7	4.2	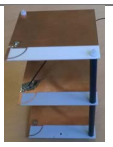
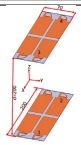	2.64	11.4	72	9.97	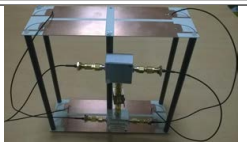
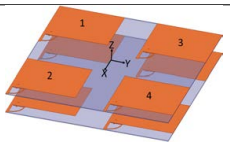	4.37	12.6	41	8.73	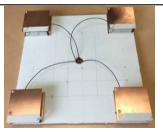
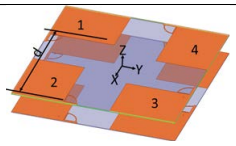	2.83	10.3	38.5	6.15	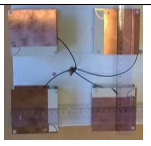

Conclusions and Future Work

Conclusions

This thesis investigates the use of parasitic superdirective arrays and non-Foster matching as solutions for enhancing the performance of Electrically Small Antennas (ESAs) beyond the theoretical limits.

NIC-Matched Antennas

The technological limitations make the design of non-Foster circuits around $900MHz$ a very complicated issue. In the first part of this thesis, and after multiple unsuccessful attempts, a very small negative capacitor based on Linvill floating-type Negative Impedance Convertor (NIC) was realized. The parasitic capacitors of the transistors were exploited to achieve this capacitance. The circuit gain, stability, noise and linearity performance were thoroughly analyzed. Then, the circuit was used to match a miniature Inverted-L Antenna (ILA) originally resonant at $2.39GHz$ in the $(0.76 - 2.17)GHz$ band. The experimental results showed that the antenna is stable, low-noise and has an acceptable total efficiency and realized gain. Around $900MHz$, the non-Foster matched antenna presents a gain improvement of $7dB$ and a total efficiency improvement by a factor of 6 compared to the passive antenna. Furthermore, the antenna Q is below the fundamental limit given bu Chu-McLean. Later, the NIC was also used to match an ILA with the same dimensions as before but on a smaller PCB so that it can be integrated in USB key. This antenna yielded a similar performance to the first one.

Superdirective Antenna Arrays

In the second part of this thesis, the theoretical limits of superdirective antenna arrays were studied and a simple and practical design approach for parasitic (loaded) superdirective antenna arrays was detailed. The practical limitations of the proposed approach were demonstrated via a parametric analysis on dipole-based arrays. This analysis showed that the loading method is not limited by the number of the elements nor by the inter-element distance. The proposed approach was later used to design two-, three- and four-element ESA-based arrays. In all cases, the parasitic array's simulated total directivity radiation pattern was very close to the fully-driven array's one. Furthermore, the end-fire directivity was maximal at the design frequency. Later, the integration of superdirective ESAs in PCBs was investigated via different scenarios showing that the PCB configuration has a significant impact on both the array directivity and radiation efficiency and adding a slot to the PCB can modify its current distribution and obtain a constructive contribution. This

leads not only to maintain the antenna's superdirectivity but also to increase its efficiency. Then, measuring superdirective ESAs integrated in PCBs was investigated via different scenarios for connecting the excitation system to the antenna. The obtained results showed that a proper connection of the excitation system can reduce its negative effects, and hence, the antenna can be measured. Afterwards, a new strategy to obtain small-size 3D or planar arrays with linear or Circular Polarization (CP) using superdirective unit-elements was presented. Although these small-size arrays were based on two-element arrays, it can be generalized on N-element ones while keeping in mind the tradeoff between the array- dimensions, -directivity and -radiation efficiency. The measured results for all the fabricated prototypes were in a good agreement with the simulated ones.

Future Work

NIC-Matched Antennas

The main drawback of the designed NIC is the internal losses. Hence, the design of high gain NIC to compensate these losses and achieve high efficiency can be a very interesting work. The design of on-chip NICs may be a possible solution for overcoming the parasitic elements issues. The design of tunable NICs is also a possible perspective. Finally, the use of non-Foster elements to achieve wide band (both in terms of directivity and impedance bandwidth) superdirective arrays seems as a very attractive application.

Superdirective Antenna Arrays

During this thesis multiple two-, three- and four-element parasitic superdirective arrays were presented. However, as the number of the elements increases, the design process becomes more complicated. In the future work, superdirective arrays of higher number of elements will be investigated. The use of other type of loading (such as modifying the element dimensions, the excitation line length (phase) and using stub-lines for replacing the localized elements) will also be studied. One another interesting approach will be investigating decoupling methods in order to design very small 3D and planar arrays based on superdirective unit-elements. In analogy with superdirtective arrays, arrays with nulls in certain directions can also be investigated. Finally, successful realizations of negative resistances will permit the design of very compact yet efficient superdirective arrays.

Annex

A Compact Planar Array Based on Three-Elements Unit-Element

Let us consider an array of three elements elements as shown in Figure 4.76(a). A parametric analysis on the inter-element distance reveals the same trends as in the previous array (Figure 4.76(b), Figure 4.76(c) and Figure 4.76(d)).

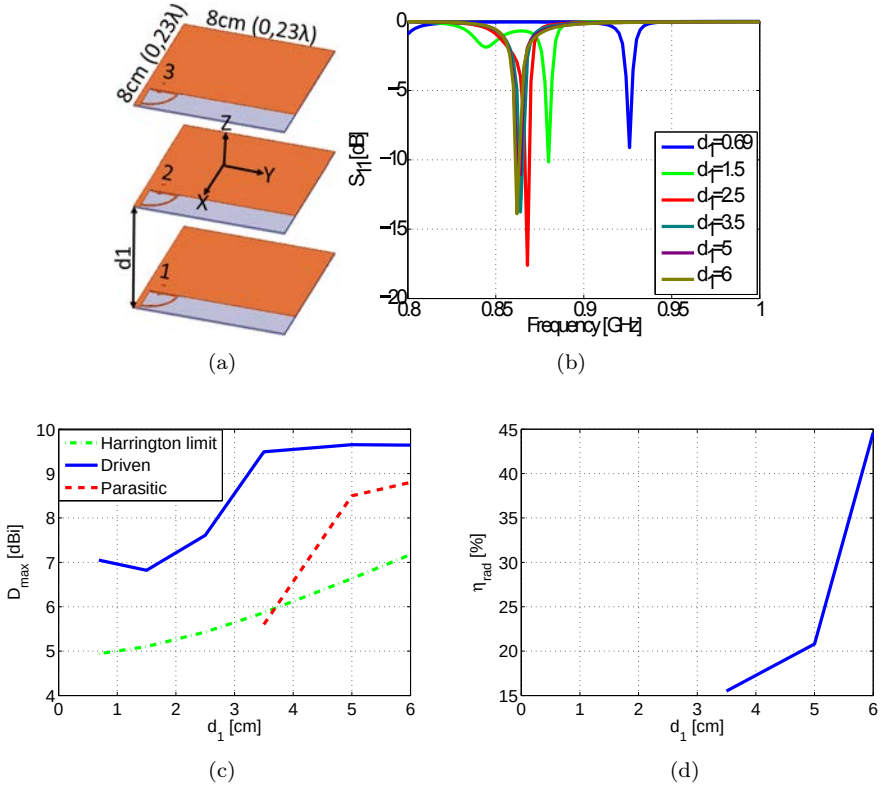

Figure 4.76: Proposed three-element array simulated parameters as a function of the inter-element distance. (a) Array geometry, (b) input reflection coefficient magnitude in dB, (c) total directivity and (d) radiation efficiency.

A prototype of the antenna array for $d_1 = 6cm(0.17\lambda)$ was fabricated and measured (Figure 4.77(a)). In this array, the second element is excited, the first is short-circuited, while the third one is loaded by $8.3nH$. Figure 4.77(b) shows the antenna input reflection coefficient magnitude in dB. As it can be noticed, the antenna has a simulated/measured resonance at $863/868MHz$ with a $S_{11} < -10dB$ bandwidth of $1.7/5MHz$. The higher losses in the measurement may be attributed

to the UFL cable used in measurement. Figure 4.77(c) shows the antenna 3D total directivity radiation pattern. The figure shows a directive pattern with a directivity of $8.8/8.5dBi$ toward z-axis. This directivity is about $1.4dB$ greater than Harrington's normal directivity limit for an antenna with the same size factor ($ka = 1.6$). The HPBW in E (XoZ) and H (YoZ) planes are respectively $72^o/73.1^o$ and $64^o/67.5^o$ and FBR is $5.8dB/4.1dB$ (Figure 4.78). The antenna presents a radiation efficiency of 34.7%/37%.

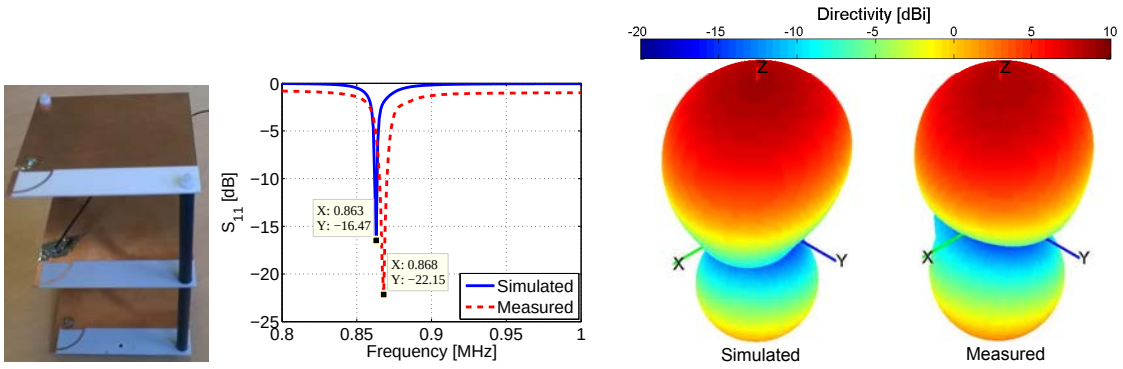

Figure 4.77: Three-element array with 6cm spacing simulated and measured parameters. (a) Fabricated prototype, (b) input reflection coefficient magnitude in dB and (c) 3D total directivity radiation pattern.

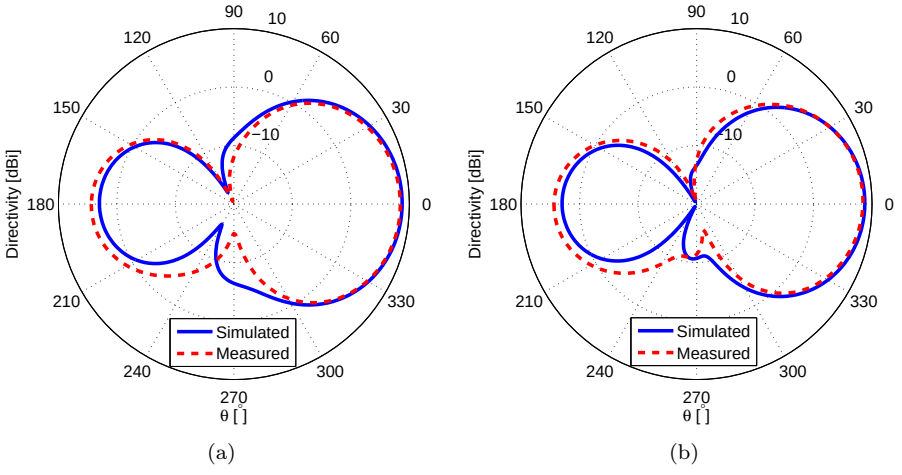

Figure 4.78: Three-element array with 6cm spacing simulated and measured parameters 2D total directivity radiation patterns. (a) E-plane, (b) H-plane.

Integrating this array in a 2×2 planar array and performing a parametric analysis on the inter-element distance the same trends as before are revealed (Figure 4.79). However, in this case we approach better Harrington limit (the average difference is about $0.5dB$).

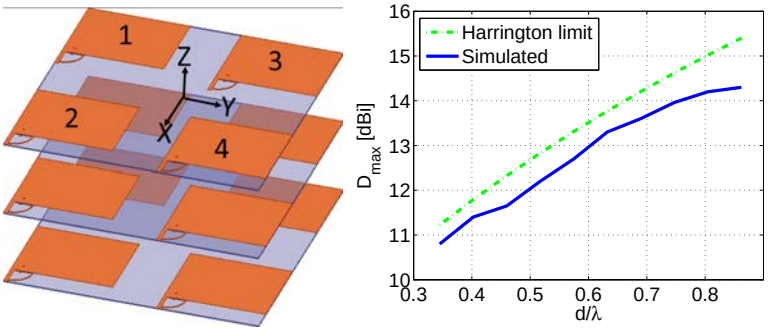

(a) (b)

Figure 4.79: Planar array based on a tree-element antenna simulated as a function of the separation. (a) Geometry, and (b) total directivity.

In this annex, a three-element parasitic superdirective antenna array was designed. These array was later integrated in 2×2 planar antenna array. This classical array based on superdirective elements approaches Harrington limit on antenna directivity.

Publications

Peer-Reviewed Journals

1. A. Haskou, D. Lemur, S. Collardey, and A. Sharaiha, Small Wide-Band ILA with Non-Foster Matching, Microwave and Optical Technology Letters. (Submitted)

2. M. Hammoud, A. Haskou, A. Sharaiha, and S. Collardey, "Small End-Fire Superdirective Folded Meandered Monopole Antenna Array", Microwave and Optical Technology Letters, vol. 58, no. 9, pp. 2122-2124, September 2016.

3. A. Haskou, A. Sharaiha, and S. Collardey, "Compact Antenna Array of Superdirective Elements", IEEE Antennas and Wireless Propagation Letters. vol. 15, pp. 1386-1389, 2016.

4. A. Haskou, A. Sharaiha, and S. Collardey, "Integrating Superdirective Electrically Small Antenna Arrays in PCBs", IEEE Antennas and Wireless Propagation Letters. vol. 15, pp. 24-27, 2016.

5. A. Haskou, A. Sharaiha, and S. Collardey, "Design of Small Parasitic Loaded Superdirective End-Fire Antenna Arrays", IEEE Transactions on Antennas and Propagation. vol. 63, no. 12, pp. 5456-5464, December 2015.

6. A. Haskou, S. Collardey, and A. Sharaiha, "Measuring Superdirective Electrically Small Antenna Arrays Mounted on PCBs", Microwave and Optical Technology Letters, vol. 57, issue 10, pp. 2269-2274, October 2015.

Peer-Reviewed International Conferences

1. A. Haskou, D. Lemur, S. Collardey, and A. Sharaiha, "A Non-Foster Circuit Design for Antenna Miniaturization", 2016 International Symposium on Antennas and Propagation (ISAP 2016), Okinawa, Japan, 24-28 October 2016.

2. A. Haskou, A. Sharaiha, and S. Collardey, "A Compact Circularly-Polarized Array Based on Superdirective Elements", 3rd IEEE Middle East Conference on Antennas and Propagation (MECAP 2016), Beirut, Lebanon, 20-22 September 2016.

3. A. Haskou, A. Sharaiha, and S. Collardey, "Designing a Stacked Three-Element Parasitic Superdirective Antenna", 17th International Symposium on Antenna Technology and Applied Electromagnetics (ANTEM 2016), Montréal, Canada, 10-13 July 2016.

4. A. Haskou, D. Lemur, S. Collardey, and A. Sharaiha, "Miniature and Wide-Band ILA Antenna with Non-Foster Matching", 10th European Conference on Antennas and Propagation (EuCAP 2016), Davos, Switzerland, 10-15 April 2016.

5. A. Haskou, A. Sharaiha, and S. Collardey, "Compact Planar Arrays Based on Parasitic Superdirective Elements", 10th European Conference on Antennas and Propagation (EuCAP 2016), Davos, Switzerland, 10-15 April 2016.

6. A. Haskou, S. Collardey, and A. Sharaiha, "Small Array Design Using Parasitic Superdirective Antennas", 10th European Conference on Antennas and Propagation (EuCAP 2016), Davos, Switzerland, 10-15 April 2016.

7. A. Haskou, S. Collardey, and A. Sharaiha, "Small 3D Array Design Using Superdirective Antennas", 2015 Loughborough Antennas and Propagation Conference (LAPC 2015), Loughborough, UK, pp. 1-3, 2-3 November 2015.

8. A. Haskou, A. Sharaiha, and S. Collardey, "A Wide-Band Miniaturized Loaded Inverted L Antenna", 2015 IEEE Symposium on Antennas and Propagation & USNC/URSI National Radio Science Meeting (APS-USNC/URSI 2015), Vancouver, Canada, pp. 1936-1937, 19-24 July 2015.

9. A. Haskou, S. Collardey, and A. Sharaiha, "A Design Methodology for Impedance-Matched Electrically Small Parasitic Superdirective Arrays", 2015 IEEE Symposium on Antennas and Propagation & USNC/URSI National Radio Science Meeting (APS-USNC/URSI 2015), Vancouver, Canada, pp. 1852-1853, 19-24 July 2015.

10. A. Haskou, A. Clemente, A. Sharaiha, C. Delaveaud, S. Collardey, and L. Rudant, "A Parasitic Three-Element Superdirective Electrically Small Antenna Array", 9th European Conference on Antennas and Propagation (EuCAP 2015), Lisbon, Portugal, pp. 1-4, 12-17 April 2015.

11. A. Haskou, A. Sharaiha, and S. Collardey, "On Measuring Superdirective Electrically Small Antenna Arrays", 2015 International Workshop on Antenna and Technology (iWAT 2015), Seoul, Republic of Korea, pp. 374-378, 4-6 March, 2015.

12. A. Sharaiha, A. Clemente, A. Haskou, M. Smierzchalski, Ch. Delaveaud, S. Collardey, L. Rudant, and K. Mahdjoubi, "Radiation Control of Electrically Small Antenna Using Superdirectivity", 3rd Advanced Electromagnetics Symposium (AES 2014), Hangzhou, China, pp. 60, 7-10 December 2014. "Keynote Lecture".

13. A. Haskou, A. Clemente, A. Sharaiha, C. Delaveaud, S. Collardey, and L. Rudant, "Ultra-Compact Superdirective Two- and Three-Element Linear Arrays", 3rd Advanced Electromagnetics Symposium (AES 2014), Hangzhou, China, pp. 105-106, 7-10 December 2014.

14. A. Haskou, A. Sharaiha, S. Collardey, M. Pigeon, and K. Mahdjoubi, "A Design Methodology for Electrically Small Superdirective Antenna Arrays", 2014 Loughborough Antennas and Propagation Conference (LAPC 2014), Loughborough, UK, pp. 405-409, 10-11 November 2014.

National Conferences

1. A. Haskou, S. Collardey, and A. Sharaiha, "Intégration dAntennes Superdirectives sur PCB", XIXèmes Journées Nationales Microondes, Bordeaux, France, pp. 216-219, 3-5 June 2015.

2. A. Haskou, S. Collardey, and A. Sharaiha, "Antenne Méandre Ultra-Miniature à Circuit Non-Foster", XIXèmes Journées Nationales Microondes, Bordeaux, France, pp. 141-142, 3-5 June 2015.

National Thematic Days

1. A. Haskou, A. Sharaiha, and S. Collardey, "Limites Théoriques et Pratiques des Antennes Superdirectives", Journées scientifiques dURSI-France 2016 "Energie et radiosciences", Cesson Sévigné, 15-16 Mars 2016.

2. A. Haskou, D. Le Mur, S. Collardey, and A. Sharaiha, "Antenne ILA Miniature et Large Bande à Circuit Non-Foster", Assemblée générale "Interférences dOndes", Lyon 19-21 Octobre 2015.

3. A. Haskou, M. Hammoud, A. Sharaiha, and S. Collardey, "Antenne Réseau Miniature et Superdirective", Assemblée générale "Interférences dOndes", Lyon 19-21 Octobre 2015.

Bibliography

[1] [Online]. Available: `http://www.agence-nationale-recherche.fr/?Projet=ANR-13-INFR-0014`

[2] [Online]. Available: `http://www.agence-nationale-recherche.fr/?Projet=ANR-11-INFR-0014`

[3] H. A. Wheeler, *"Fundamental Limits of Small Antennas"*, Proceedings of The I.R.E. (IEEE), pp. 1479-1484, December 1947.

[4] H. A. Wheeler, *"The Radiansphere Around a Small Antenna"*, Proceedings of The I.R.E. (IEEE), vol. 47, August 1959.

[5] L. .J. Chu, *"Physical Limitations of OmniDirectional Antennas"*, Journal of Applied Physics, vol. 19, no. 12, pp. 1163-1175, 1948.

[6] J. S. McLean, *"A Re-Examination of the Fundamental Limits on The Radiation Q of Electrically Small Antennas"*, IEEE Transactions on Antennas and Propagation, vol. 44, no. 5, pp. 672-675, May 1996.

[7] R. M. Fano, *"Theoretical Limitations on the Broadband Matching of Arbitrary Impedances"*, J. Franklin Institution, vol. 249, pp. 57-83 and 139-155, January and February 1950.

[8] R. F. Harrington, *"On the Gain and Beamwidth of Directional Antennas"*, IRE Transactions on Antennas and Propagation, pp. 219-225, July 1958.

[9] G. A. Thiele, P. L. Detweiler, and R. P. Penno, *"On the Lower Bound of the Radiation Q for Electrically Small Antennas"*, IEEE Transactions on Antennas and Propagation, vol. 51, pp. 1263-1269, June 2003.

[10] W. Geyi, *"Method for the Evaluation of Small Antenna Q"*, IEEE Transactions on Antennas and Propagation, vol. 51, no. 8, pp. 2124-2129, August 2003.

[11] S. R. Best and A. D. Yaghjian, *"The Lower Bounds on Q for Lossy Electric and Magnetic Dipole Antennas"*, IEEE Antennas and Wireless Propagation Letters, vol. 3, pp. 314-316, December 2004.

[12] H. L. Thal, *"New Radiation Q Limits for Spherical Wire Antennas"*, IEEE Transactions on Antennas and Propagation, vol. 54, no. 10, pp. 2757-2763, October 2006.

[13] M. Gustafsson, C. Sohl, and G. Kristensson, *"Illustrations of New Physical Bounds on Linearly Polarized Antennas"*, IEEE Transactions on Antennas and Propagation, vol. 57, pp. 1319-1327, May 2009.

[14] A. D. Yaghjian and H. R. Stuart, *"Lower Bounds on the Q of Electrically Small Dipole Antennas"*, IEEE Transactions on Antennas and Propagation, vol. 58, pp. 3114-3121, 2010.

[15] G. A. E. Vandenbosch, *"Reactive Energy, Impedance, and Q Factor of Radiating Structures"*, IEEE Transactions on Antennas and Propagation, vol. 58, pp. 1112-1127, 2010.

[16] M. Gustafsson and S. Nordebo, *"Optimal Antenna Currents for Q, Superdirectivity, and Radiation Patterns Using Convex Optimization"*, IEEE Transactions on Antennas and Propagation, vol. 61, pp. 1109-1118, March 2013.

[17] B. L. G. Jonsson and M. Gustafsson, *"Stored Energies for Electric and Magnetic Currents with Applications to Q for Small Antennas"*, International Symposium on Electromagnetic Theory, Hiroshima, Japan, pp. 1050-1053, 2013.

[18] A. D. Yaghjian, M. Gustafsson, and B.L.G. Jonsson, *"Minimum Q for Lossy and Lossless Electrically Small Dipole Antennas"*, PIER, December 2013.

[19] M. Pigeon, A. Clemente, C. Delaveaud and L. Rudant, *"Analysis of Harrington Limit for Electrically Small Antenna Directivity"*, The 8th European Conference on Antennas and Propagation (EuCAP 2014), The Hague, pp. 2921-2925, 2014.

[20] M. Hirvonen, A. Hujanen, J. Holmberg, and J.C.-E. Sten, *"Bandwidth Limitations of Dipoles Matched with Non-Foster Impedances"*, The Second European Conference on Antennas and Propagation (EuCAP 2007), pp. 1,5, 11-16 November 2007.

[21] R. M. Foster, *"A Reactance Theorem," Bell System Technical Journal"*, vol. 3, pp. 259-267, 1924.

[22] M. Latour, *"Basic Theory of Electron-Tube Amplifiers- Part II"*, 30 October 1920.

[23] J. L. Merrill, *"Theory of the Negative Impedance Converter"*, The Bell System Technical Journal, vol. 30, no. 1, pp. 88,109, January 1951.

[24] J. G. Linvill, *"Transistor Negative-Impedance Converters"*, Proceedings of the IRE, vol. 41, no. 6, pp. 725-729, June 1953.

[25] S. E. Sussman-Fort, *"Gyrator-Based Biquad Filters and Negative Impedance Converters for Microwaves"*, International Journal of RF and Microwave Computer-Aided Engineering, vol. 8, p.p. 86-101, March 1998.

[26] A. Bahr, *"On The Use of Active Coupling Networks with Electrically Small Receiving Antennas"*, IEEE Transactions on Antennas and Propagation, vol. 25, no. 6, pp. 841,845, November 1977.

[27] S. E. Sussman-Fort, *"Matching Network Design Using NonFoster Impedances"*, International Journal of RF and Microwave ComputerAided Engineering, vol. 16, no. 2, p.p. 135-142, 2006.

[28] S. E. Sussman-Fort, and R. M. Rudish, *"Non-Foster Impedance Matching for Transmit Applications"*, 2006 IEEE International Workshop on Antenna Technology Small Antennas and Novel Metamaterials, pp. 53,56, 6-8 March 2006.

[29] S. Koulouridis, and J.L. Volakis, *"Non-Foster Circuits for Small Broadband Antennas"*, IEEE Antennas and Propagation Society International Symposium (APS-URSI 2009), pp. 1,4, 1-5 June 2009.

[30] F. Yifeng, K. Z. Rajab, M. Munoz, and H. Yang, *"Electrically Small Half-Loop Antenna Design with Non-Foster Matching Networks"*, 6th European Conference on Antennas and Propagation (EuCAP 2012), pp. 126,129, 26-30 March 2012.

[31] W. Li, R. Chen, N. Zhai, S. Li, and R. Mittra, *"Wideband Matching of an Electrically Small Antenna Using a Negative Impedance Converter Technique"*, 2012 IEEE Antennas and Propagation Society International Symposium (APS-URSI 2012), pp. 1,2, 8-14 July 2012.

[32] C. R. White, J. S. Colburn, and R.G. Nagele, *"A Non-Foster VHF Monopole Antenna"*, IEEE Antennas and Wireless Propagation Letters, vol. 11, pp. 584,587, 2012.

[33] H. Mirzaei, and G. V. Eleftheriades, *"A Wideband Metamaterial-Inspired Compact Antenna Using Embedded Non-Foster Matching"*, 2011 IEEE International Symposium on Antennas and Propagation (APS-URSI 2011), pp. 1950,1953, 3-8 July 2011.

[34] G. Mishra, S. K. Sharma, and G. Rebeiz, *"Non-Foster Matching of Electrically Small Bowtie Antenna Covering 600MHz to 1100MHz"*, 2015 IEEE Symposium on Antennas and Propagation & USNC/URSI National Radio Science Meeting (APS-USNC/URSI 2015), 19-25 July, 2015.

[35] M. M. Jacob, J. long, and D. F. Sievenpiper, *"Nonlinear Effects of Non-Foster Matching Networks"*, 2015 IEEE Symposium on Antennas and Propagation & USNC/URSI National Radio Science Meeting (APS-USNC/URSI 2015), 19-25 July, 2015.

[36] D. S. Nagarkoti, Y. Hao and K. Z. Rajab, *"Q-Bandwidth Enhancement of an Antenna Using Non-Foster Circuit Based on Negative Differential Resistance Devices"*, 10th European Conference on Antennas and Propagation (EuCAP 2016), 10-15 April 2016.

[37] O. O. Tade, P. Gardner, and P.S. Hall, *"1.5 GHz Negative Impedance Converters"*, IET Journal.

[38] S. Koulouridis, and S. Stefanopoulos, *"Stability and Implementation of Non-Foster Circuits for Antennas"*, 2012 IEEE Antennas and Propagation Society International Symposium (APS-URSI 2012), pp. 1,2, 8-14 July 2012.

[39] E. Ugarte-Munoz, F. Albarracin, F.J. Herraiz-Martinez, and D. Segovia-Vargas, *"Sensitivity and Stability Analysis of Non-Foster Matched Two-Port Antennas"*, 7th European Conference on Antennas and Propagation (EuCAP 2013), pp. 3006,3009, 8-12 April 2013.

[40] H. Mirzaei, and G.V. Eleftheriades, *"A Resonant Printed Monopole Antenna With an Embedded Non-Foster Matching Network"*, IEEE Transactions on Antennas and Propagation, vol. 61, no. 11, pp. 5363,5371, November 2013.

[41] K. A. Obeidat, B.D. Raines, and R.G. Rojas, *"Application of Characteristic Modes and Non-Foster Multiport Loading to the Design of Broadband Antennas"*, IEEE Transactions on Antennas and Propagation, vol. 58, no. 1, pp. 203,207, January 2010.

[42] D.J. Gregoire, C.R. White, and J.S. Colburn, *"Wideband Artificial Magnetic Conductors Loaded With Non-Foster Negative Inductors"*, IEEE Antennas and Wireless Propagation Letters, pp. 1586,1589, 2011.

[43] J. Long, and D. Sievenpiper, *"DispersionReduced High Impedance Surface Loaded with Non-Foster Impedances"*, 2015 IEEE Symposium on Antennas and Propagation & USNC/URSI National Radio Science Meeting (APS-USNC/URSI 2015), 19-25 July, 2015.

[44] M. Barbuto, A. Monti, F. Bilotti and A. Toscano, *"Design of a Non-Foster Actively Loaded SRR and Application in Metamaterial-Inspired Components"*, IEEE Transactions on Antennas and Propagation, vol. 61, no. 3, pp. 1219-1227, March 2013.

[45] T. Debogovic, S. Hrabar and J. Perruisseau-Carrier, *"Broadband Fabry-Pérot Radiation Based on Non-Foster Cavity Boundary"*, Electronics Letters, vol. 49, no. 4, pp. 239-240, 14 February 2013.

[46] S. R. Rengarajan and C. R. White, *"Stability Analysis of Superluminal Waveguides Periodically Loaded With Non-Foster Circuits"*, IEEE Antennas and Wireless Propagation Letters, vol. 12, pp. 1303-1306, 2013.

[47] F. Gao, F. Zhang, J. Long, M. Jacob and D. Sievenpiper, *"Non-Dispersive Tunable Reflection Phase Shifter Based on Non-Foster Circuits"*, Electronics Letters, vol. 50, no. 22, pp. 1616-1618, 23 October 2014.

[48] M. M. Jacob, J. Long and D. F. Sievenpiper, *"Non-Foster Loaded Parasitic Array for Broadband Steerable Patterns"*, IEEE Transactions on Antennas and Propagation, vol. 62, no. 12, pp. 6081-6090, December 2014.

[49] S.D. Stearns, *"Non-Foster Circuits and Stability Theory"*, 2011 IEEE International Symposium on Antennas and Propagation (APS-URSI 2011), pp.1942,1945, 3-8 July 2011.

[50] S.D. Stearns, *"Incorrect Stability Criteria for Non-Foster Circuits"*, 2012 IEEE Antennas and Propagation Society International Symposium (APS-URSI 2012), pp. 1,2, 8-14 July 2012.

[51] J. Loncar, D. Muha, and S. Hrabar, *"Influence of Transmission Line on Stability of Networks Containing Ideal Negative Capacitors"*, 2015 IEEE Symposium on Antennas and Propagation & USNC/URSI National Radio Science Meeting (APS-USNC/URSI 2015), 19-25 July, 2015.

[52] [Online]. Available: `https://etd.ohiolink.edu/rws_etd/document/get/osu1308313555/inline`

[53] D. S. Nagarkoti, Y. Hao, D. P. Steenson, L. Li, E. H. Linfield and K. Z. Rajab, *"Design of Broadband Non-Foster Circuits Based on Resonant Tunneling*

Diodes", IEEE Antennas and Wireless Propagation Letters, vol. 15, pp. 1398-1401, 2016.

[54] H. Yang, I. Kim and K. Kim, *"Non-Foster Matching of a Resistively Loaded Vee Dipole Antenna Using Operational Amplifiers"*, IEEE Transactions on Antennas and Propagation, vol. 64, no. 4, pp. 1477-1482, April 2016.

[55] J. S. Roberts and R. W. Ziolkowski, *"Non-Foster Circuit Matching of a Near-Field Resonant Parasitic, Electrically Small Antenna"*, 2015 International Workshop on Antenna Technology (iWAT), pp. 89-91, Seoul, 2015.

[56] A. M. Elfrgani and R. G. Rojas, *"Stability of Non-Foster Circuits for Broadband Impedance Matching of Electrically Small Antennas"*, 2015 IEEE Radio and Wireless Symposium (RWS), pp. 50-52, San Diego, CA, 2015.

[57] A. M. Elfrgani and R. G. Rojas, *"Successful Realization of Non-Foster Circuits for Wide-Band Antenna Applications"*, 2015 IEEE MTT-S International Microwave Symposium, pp. 1-4, Phoenix, AZ, 2015.

[58] [Online]. Available: `http://www.alldatasheet.com/datasheet-pdf/pdf/48370/AD/AD8009.html`

[59] [Online]. Available: `http://etheses.bham.ac.uk/4920/1/Tade14PhD.pdf`

[60] [Online]. Available: `http://pdf1.alldatasheet.com/datasheet-pdf/view/16347/PHILIPS/BFR93A.html`

[61] [Online]. Available: `https://www.minicircuits.com/pdfs/ZX60-P33ULN+.pdf`

[62] [Online]. Available: `http://beyondmeasure.rigoltech.com/acton/attachment/1579/f-0025/0/-/-/-/-/file.pdf`

[63] G. Le Fur, C. Lemoine, P. Besnier, A. Sharaiha, *"Performances of UWB Wheeler Cap and Reverberation Chamber to Carry Out Efficiency Measurements of Narrowband Antennas"*, IEEE Antennas and Wireless Propagation Letters, Vol. 8, pp.332,335, 2009.

[64] C. J. Bowkamp and N. G. de Bruijn, *"The Problem of Optimum Antenna Current Distribution"*, Philips Research Reports, vol. 1, pp. 135-158, January 1946.

[65] H. J. Riblet, *"Discussion on A Current Distribution for Broadside Arrays Which Optimizes the Relationship Between Beamwidth and Side-Lobe Level"*, Proceedings of the IRE, pp. 489-492, May 1947.

[66] R. C. Hansen, *"Fundamental Limitations in Antennas"*, Proceedings of IEEE, vol. 69, pp. 170-181, February 1981.

[67] I. Uzkov, *"An Approach to the Problem of Optimum Directive Antennae Design"*, Comptes rendues (Doklady) de l'académie des sciences de l'URSS, Vol. 53, No. 1, 1946.

[68] N. Yaru, *"A Note on Super-Gain Antenna Arrays*, in Proceedings of the IRE, vol. 39, no. 9, pp. 1081-1085, September 1951.

[69] E. N. Gilbert, and S. P. Morgan, *"Optimum Design of Directive Antenna Arrays Subject to Random Variations"*, Bell System Technical Journal, vol. 34, pp. 637-663, May 1955.

[70] C. O. Stearns, *"Computer Performance of Moderate Size, Super-Gain Antennas"*, NBS Report 6797, 5 September, 1961.

[71] C. T. Tai, *"The Optimum Directivity of Uniformly Spaced Broadside Arrays of Dipoles"*, IEEE Transactions on Antennas and Propagation, vol. 12, pp. 447-454, July 1964.

[72] E. H. Newman, J. H. Richmond, and C. H. Walter, *"Superdirective Receiving Arrays"*, IEEE Transactions on Antennas and Propagation, vol. AP-26, no. 5, pp. 629635, September 1978.

[73] M. M. Dahoud and A. P. Anderson, *"Design of Superdirective Arrays with High Radiation Efficiency"*, IEEE Transactions on Antennas and Propagation, vol. AP-26, no. 6, pp. 819823, November 1978.

[74] E. H. Newman and M. R. Schrote, *"A Wide-Band Electrically Small Superdirective Array"*, IEEE Transactions on Antennas and Propagation, vol. AP-30, no. 6, pp. 1172-1176, November 1982.

[75] R. P. Haviland, *"Supergain Antennas: Possibilities and Problems"*, IEEE Antennas Propagation Magazine, vol. 37, pp. 13-26, August 1995.

[76] A. Bloch, R. G. Medhurst, and S. D. Pool, *"A New Approach to the Design of Super-Directive Aerial Arrays"*, in Proceedings of the IEE- Part III: Radio and Communication Engineering , vol. 100, no. 67, pp. 303-314, September 1953.

[77] C. A. Balanis, *"Antennas Theory: Analysis and Design"*, John Wiley and Sons Incorporation, Third edition, New York, 2005.

[78] R. C. Hansen, and R. E. Collin, *"Small Antenna Handbook"*, John Wiley & Sons Incorporation, Hoboken, New Jersey, 2011.

[79] W. W. Hansen, J.R. Woodyard, *"A New Principle in Directional Antenna Design"*, Proceedings of the IRE, vol. 26, pp. 3333-345, 1938.

[80] S. A. Schelkunoff, *"A Mathematical Theory of Linear Arrays"*, Bell System Technical Journal, vol. 22, pp. 80-107, 1943.

[81] C.L. Dolph, *"A Current Distribution for Broadside Arrays Which Optimizes the Relationship between Beam Width and Side-Lobe Level"*, Proceedings of the IRE, vol. 34, no. 6, pp. 335-348, June 1946.

[82] E. E. Altshuler, T. H. O'Donnell, A.D. Yaghjian, and S. R. Best, *"A Monopole Superdirective Array"*, IEEE Transactions on Antennas and Propagation, vol. 53, no. 8, pp. 2653-2661, August 2005.

[83] A. Clemente, M. Pigeon, L. Rudant and C. Delaveaud, *"Super Directive Compact Antenna Design Using Spherical Wave Expansion"*, IEEE International Symposium on Antennas and Propagation Society (APSURSI 2014), pp. 571-572, Memphis, TN, 2014.

[84] J. E. Hansen, *"Spherical Near-Field Antenna Measurements"*, IET Electromagnetic Waves Series, 1988.

[85] A. Clemente, M. Pigeon, L. Rudant, and C. Delaveaud, *"Design of a Super Directive Four-Element Compact Antenna Array Using Spherical Wave Expansion*, IEEE Transactions on Antennas and Propagation, vol. 63, no. 11, pp. 4715-4722, November 2015.

[86] J. Capon, *"High-Resolution Frequency Wavenumber Spectrum Analysis"*, Proceedings of IEEE.

[87] Z. Xi, X.F. Wu, S. Wu, Z. Tang, and S. Hu, *"Low-Complexity Robust Capon Beamforming Based on Reduced-Rank Technique"*, Journal of Electrical and Computer Engineering, 2015.

[88] T. H. O'Donnell, and A. D. Yaghjian, *"Electrically Small Superdirective Arrays Using Parasitic Elements"*, IEEE Antennas and Propagation Society International Symposium 2006, pp. 3111,3114, 9-14 July 2006.

[89] T. H. O'Donnell, A. D. Yaghjian, and E. E Altshuler, *"Frequency Optimization of Parasitic Superdirective Two Element Arrays"*, IEEE Antennas and Propagation Society International Symposium 2007, pp. 3932,3935, 9-15 June 2007.

[90] S. Lim, and H. Ling, *"Design of Electrically Small Yagi Antenna"*, Electronics Letters, vol. 43, no. 5, pp.3-4, 1 March 2007.

[91] S. R. Best, E. E. Altshuler, A. D. Yaghjian, J. M. McGinthy, and T. H. O'Donnell, *"An Impedance-Matched 2-Element Superdirective Array"*, IEEE Antennas and Wireless Propagation Letters, Vol. 7, pp. 302-305, 2008.

[92] A. D. Yaghjian, T. H. O'Donnell, E. E. Altshuler, and S. R. Best *"Electrically Small Supergain End-Fire Arrays"*, Radio Science, vol. 43, 2008.

[93] S. M. Mazinani, and H.R. Hassani, *"Superdirective Wideband Array of Planar Monopole Antenna With Loading Plates"*, IEEE Antennas and Wireless Propagation Letters, vol. 9, pp. 978-981, 2010.

[94] O. S. Kim, S. Pivnenko, and O. Breinbjerg, *"Superdirective Magnetic Dipole Array as a First-Order Probe for Spherical Near-Field Antenna Measurements"*, IEEE Transactions on Antennas and Propagation, vol. 60, No. 10, pp.4670-4676, October 2012.

[95] O. S. Kim, S. Pivnenko, and O. Breinbjerg, *"Superdirective Dual-Polarized First-Order Probe for SNF Measurements at Low Frequencies"*, 10th European Conference on Antennas and Propagation (EuCAP 2016), 10-15 April 2013.

[96] J. M. Lugo, J. de Almeida Goes, A. Louzir, P. Minard, D. Lo Hine Tong, and C. Person, *"Design, Optimization and Characterization of a Superdirective Antenna Array"*, 7th European Conference on Antennas and Propagation (EuCAP), pp. 3736,3739, 8-12 April 2013.

[97] L. Batel, L. Rudant, J. F. Pintos, A. Clemente, C. Delaveaud, and K. Mahdjoubi, *"High Directive Compact Antenna with Non-Foster Elements*, in 2015 International Workshop on Antenna Technology (iWAT), pp. 381-384, 4-6 March 2015.

[98] I. Liberal, I. Ederra, R. Gonzalo, and R. W. Ziolkowski, *"Superbackscattering Antenna Arrays"*, IEEE Transactions on Antennas and Propagation, Vol. 63, No. 5, pp.2011-2021, May 2015.

[99] J. Narrainen, *"Conception de Réseau Miniature Superdirectif et Traitements Haute-Résolution"*, internship report, 6 September 2013.

[100] B. Sentucq, A. Sharaiha, and S. Collardey, *"Superdirective Compact Parasitic Array of Metamaterial-Inspired Electrically Small Antenna"*, International Workshop on Antenna Technology (iWAT), pp. 269,272, 4-6 March 2013.

[101] B. Sentucq, A. Sharaiha, and S. Collardey, *"Superdirective Metamaterial-Inspired Electrically Small Antenna Arrays"*, 7th European Conference on Antennas and Propagation (EuCAP2013), pp.151,155, 8-12 April 2013.

[102] M. Pigeon, A. Sharaiha, and S. Collardey, *"Miniature and Superdirective Two Elements Endfire Antenna Array"*, 8th European Conference on Antennas and Propagation (EuCAP 2014), 6-11 April 2014.

[103] ANSYS HFSS, Pittsburg, PA 15219, USA.

[104] B. Riemann, *"Ueber die Darstellbarkeit einer Function durch eine trigonometrische Reihe"*, Göttingen: Dieterich, 1867. Online version available at: (http://eudml.org/doc/203787)

[105] J. C.-E. Sten, and M. Hirvonen, *"Impedance and Quality Factor of Mutually Coupled Multiport Antennas"*, Microwave and Optical Technology Letters, vol. 50, no. 8, pp. 20342039, August 2008.

[106] M. Uzsoky, and L. Solymar, *"Theory of Super-Directive Linear Arrays"*, Acta Physica Academiae Scientiarum Hungaricae, Vol. 6, pp.185205, 1956.

[107] B. Jannier, M. A. C. Niamien, A. Sharaiha, and S. Collardey, *"DVB-T Reception Test with Ultra Miniature CPW Antenna"*, 5th European Conference on Antennas and Propagation (EuCAP 2011), pp.1842,1845, 11-15 April 2011.

[108] J. T. Bernhard, J. J. Adams, M. D. Anderson, and J. M. Martin, *"Measuring Electrically Small Antennas: Details and Implications"*, IEEE International Workshop on Antenna Technology (iWAT 2009), pp.1,4, 2-4 March 2009.

[109] P. J. Massey, and K. R. Boyle, *"Controlling the Effects of Feed Cable in Small Antenna Measurements"*, 12th International Conference on Antennas and Propagation (ICAP 2003), Vol. 2, pp.561,564, 31 March-3 April 2003.

[110] [Online]. Available: `http://www.titanwirelessonline.com/v/vspfiles/assets/images/at-ya-9%20data%20sheet.pdf`

[111] [Online]. Available: `http://www.enprobe.de/products_FO-Links.htm`

[112] [Online]. Available: `http://avalanwireless.com/marketing_resources/\product_briefs/AW11-900.pdf`

[113] [Online]. Available: `www.minicircuits.com/pdfs/ZFSCJ-2-4.pdf`

[114] [Online]. Available: `www.minicircuits.com/pdfs/ZX10-2-20.pdf`

[115] [Online]. Available: http://docs-europe.electrocomponents.com/webdocs/12a7/0900766b812a766a.pdf

[116] [Online]. Available: http://194.75.38.69/pdfs/ZN4PD-920W.pdf

[117] [Online]. Available: http://www.datasheetarchive.com/dl/Scans-060/DSA2IH0075492.pdf

Résumé

Pour faire cohabiter les nombreuses technologies radios, les terminaux mobiles nécessitent une miniaturisation de plus en plus poussée des antennes. Toutefois, les performances d'antennes ont des limites fondamentales liées à leurs dimensions physiques. La littérature met en évidence que les réseaux superdirectifs permettent de dépasser la limite de Harrington sur la directivité et que des antennes adaptées par des circuits non-Foster peuvent dépasser la limite de Bode-Fano sur la bande passante. Les contributions essentielles de ce travail de thèse consistent en la conception de réseaux d'antennes superdirectifs et d'antennes adaptées par des circuits non-Foster comme solutions possibles pour l'amélioration des performances des Antennes Electriquement Petites (AEP). Dans une première partie, un convertisseur d'impédance négative est réalisé pour obtenir des condensateurs de valeurs négatives de façon à adapter des antennes miniatures sur une large bande de fréquence. Dans la deuxième partie de ces travaux, les limites théoriques des réseaux d'antennes superdirectifs sont évaluées et une approche simple et pratique permettant la conception de ces réseaux à partir d'éléments parasites est proposée. L'intégration des AEP superdirectives sur des cartes de circuit imprimé est étudiée et les difficultés de mesure de ce type d'antenne sont évaluées. A partir de ces résultats, une nouvelle stratégie pour réaliser des réseaux compactes 3D ou planaires à polarisation linéaire ou circulaire en utilisant des éléments superdirectifs est présentée.

Mots clés : antenne électriquement petite, circuit non-Foster, convertisseur d'impédance négative, superdirectivité, réseau d'antenne parasite

Abstract

For supporting different wireless technologies, mobile terminals require significant miniaturization of antennas. However, antennas performance has some fundamental limits related to their physical dimensions. The available theory shows that superdirective arrays can exceed Harrington's limit on antenna directivity and non-Foter matched antennas can surpass Bode-Fano limit on antenna bandwidth. Therefore, this work focuses on the design of superdirective antenna arrays and non-Foster matched antennas as possible solutions for improving the performance of Electrically Small Antennas (ESAs). In the first part: a Negative Impedance Converter (NIC) is designed to have a very small negative capacitor. The circuit is evaluated in terms of gain, stability and linearity. Then, the circuit is used to match several small antennas in the UHF band. In the second part: the theoretical limits of superdirective antenna arrays are studied. A simple and practical approach to design parasitic antenna arrays is proposed. The integration of superdirective ESAs in Printed Circuit Boards (PCBs) is studied and the difficulties of measuring this type of antennas are evaluated. A new strategy for the design of 3D or planar compact arrays, with linear or circular-polarization, using superdirective elements is presented.

Key words: Electrically Small Antenna (ESA), non-Foster circuit, Negative Impedance Convertor (NIC), superdirectivity, parasitic antenna array